Quantum Control of Cold Rydberg Ensembles and Non-Hermitian Systems

Chengxing He

Beijing, China

B.S., University of Science and Technology of China, 2015

A Dissertation Presented to

the Graduate Faculty of the University of Virginia

in Candidacy for the Degree of

Doctor of Philosophy

Department of Physics

University of Virginia

September, 2021

Abstract

In this dissertation, mechanisms of dephasing in a cold dipole-dipole coupled Rydberg gas are discussed, and control sequences for suppressing dephasing are introduced and experimentally demonstrated. Additionally, population control in a two level non-Hermitian system facilitated by control loops in 2-dimensional parameter space is simulated and modeled analytically.

Detuning jump sequences inspired by quasi-phase matching in nonlinear optics are introduced and utilized to suppress dephasing in a cold Rydberg gas. Rabi flopping in random dipole-dipole coupled systems with more than a few atoms is demonstrated for the first time by actively suppressing dephasing with detuning jump sequences. The dephasing suppression mechanism is introduced and experimental results at different detunings and different Rydberg atom densities are compared.

Dephasing in cold dipole-dipole coupled Rydberg gases due to (1) inhomogeneities in dipole-dipole interaction strengths between atoms and (2) Rydberg excitation hopping between different atoms, is considered. By comparing experimental Rabi oscillation spectra with the results of simulations with hopping effects turned on/off, it was found that excitation hopping plays a more important role when the system is far detuned from energy transfer resonance. Increased density results in proportional increases in the dephasing associated with the two mechanisms.

The second part of the dissertation focuses on a numerical study of population transfer in a two level non-Hermitian system subject to control loops along which the coupling and energy separation betwen the two levels are adiabatically varied. Contrary to previous studies, we found that population transfer can be achieved even when the control loop does not encircle an exceptional point (EP) of degeneracy in the chiral complex eigenvalue landscape.

Acknowledgements

Getting a PhD is an arduous process for most, me included. Fortunately, I was surrounded by many talented and experienced people who were able to guide me through this process. While it is not possible to acknowledge all of those who have helped me, there are a few who I am especially grateful to.

To work as a research assistant for most of my PhD years and focus solely on research is a luxury. I would first like to thank the physics department and Prof. Robert Jones for writing grant proposals that funded this research, especially so in an era when science is under constant attack.

Of course as my PhD advisor, Prof. Jones offered much more help beyond financial support. He is always available for answering my questions, no matter late night or while he is out of town. I am especially grateful for his patience of guiding me hand in hand to dig deep into every corner of scientific problems, and to examine every parameter of experimental conditions and their implications. I am still learning new things while writing up this dissertation thanks to Prof. Jones' dedication of editing this dissertation in great details and raising new questions while doing so. This rigor paid dividends, as all the topics discussed in this dissertation are sparked by new phenomena that arose when attempting to repeat other researcher's efforts, which others had simply neglected.

I would like to thank Prof. Cass Sackett and Prof. Eugene Kolomeisky for serving in my research committee, they asked some truly important questions during committee reviews that helped me think deeper with my research. Prof. Cass Sackett also helped me figure out MOT designs with his expertise and

our lab was lucky to borrow or inherent equipment from Prof. Cass Sackett and Prof. Tom Gallagher. The physics building underwent renovation during my PhD and I would like to thank Rick Marshall for keeping the experimental environment relatively stable despite all the hammerings.

I am very fortunate to have my cousin Hui Tang and her husband Shu Hu, who started his tenure track as I started my PhD, to guide me through a lot of issues during PhD, from small things like preparing presentations to broad topics like impacts of my research. After discussing many-body quantum physics with me for years, Shu, a native material scientist, was able to find a niche in quantum materials, and I was able to appreciate how my research could work on platforms beyond cold Rydberg gas, talking about a fruitful relation!

Despite not directly working in natural science, my parents, Dingchao He and Yongping Liao are always trying their best to understand my research field, and sharing whatever information they can find regarding the outlook of my research field, keep reminding me that the future is bright. Additionally, as family members, their caring and support was very important for me during my micro-depressions and micro-anxieties.

I was fortunate to have a lot of talented colleagues in the Jones group. Although far from the easiest MOT setup to work with, I am grateful to Mary Kutteruf, Tao Zhou and Brian Richards for setting the MOT up, especially to Brian Richards who shared two years in the lab with me, and taught me how to operate the experimental apparatus, use Labview based softwares, as well as programming in R, and offered help even after he has graduated. Prof.

Charles Conover and Dr. Sachin Sharma, both experienced MOT operators, helped adjusting the MOT and offered ideas for improving MOT designs. A lot of equipments were borrowed from the PLSB lab over the years, and a lot of discussion with Sanjay Khatri, Lingyun Chai, Dr. Peter Sandor, Dr. Ali Azarm and Mark Gordon helped me decide what optical elements to buy and how to setup my apparatus. Towards the last few years of PhD, journal club was organized within the group and the exchange of ideas between Dr. Sachin Sharma, Dr. Ali Azarm, Sanjay Khatri, Lingyun Chai and me were very valuable for me to better understand my research and gain knowledge in other research fields.

Outside the research group, I was also fortunate to have a lot of friends with a lot of expertise that helped me during my PhD. Xiao Hu taught me how to use Matlab. Jie Qi helped me with machining and designing apparatus in general. Liyu Liu showed me the latest optical setup in their newly-built apparatus and borrowed me a few optical elements to play with, switching to those elements eventually helped me to drastically increase the stability of apparatus in our lab. Zhijie Fan taught me how to use Rivanna computing clusters and setup the LaTeX format for this dissertation. Meng Hua and Rajveer Nehra are activists who shared a lot of information on finding jobs and postdocs towards the end of my PhD. Of course, in addition to all their academic expertise, all those people mentioned above and many others in and out of the department are great friends who made my PhD years enjoyable.

Contents

List of Figures

List of Tables

Chapter 1

Introduction

Quantum many-body physics can be extremely complex. As a matter of fact, no analytical solution exists for a system as simple as a helium atom, which consist of a nucleus and two electrons. Therefore, research in many body quantum physics typically involves grasping the essence, or the dominant interaction within the system with a simplified physics picture, with corrections added as needed. In quantum physics, this philosophy dates back to the characterization of spin-orbit coupling [7], the Born-Oppenheimer approximation [8], the Hartree-Fock method [9] etc., and is still followed by modern physicists today.

Embracing the philosophy of "grasping the essence," the goal of this dissertation is to accurately describe, with the simplest physics model, the characteristics and behavior of many body quantum systems created in the lab, and to identify the main contributors to, and simple remedies to combat dephasing/decoherence within those systems. Our efforts focus on a particular

many body quantum system: an ensemble of cold Rydberg atoms in a diffuse gas. Whilst the study of dephasing/decoherence has long been an important topic in quantum physics, as interference has been long regarded as one criteria that distinguishes quantum from classical systems, in recent years, the study of many body quantum systems, including the study of dephasing/decoherence mechanisms and control, has come under the spotlight. In large part this is due to the realization of engineered many body quantum systems, namely quantum computers/simulators that have the potential to serve as powerful technologies that will help advance science (beyond physics) and reshape many industries [10, 11, 12].

Originally proposed theoretically by R. Feynman [13] and popularized by Shor's algorithm [14], the laboratory realizations of quantum computation/simulation are fairly recent. A successful experimental realization of quantum computer should meet DiVincenzo's criteria [15], the first of which is "a scalable physical system with well characterized qubits". Unfortunately, regardless of operating platforms, quantum computers/simulators suffer from problems such as cross-talk and inhomogeneities involving unwanted or ill-defined interactions between qubits, or between qubits and their environment. The presence of such effects means that the qubits are no longer "well characterized", and results in dephasing and decoherence. Understanding interactions between qubits, and between qubits and their environment, and further designing protocols to eliminate or homogenize those interactions, is important for the future development of quantum computation/simulation.

Albeit not explored directly in a quantum computer/simulator, those is-

sues are exactly what the experiments in this dissertation set out to explore. Rydberg atoms are a popular choice for facilitating quantum gates because of their sensitivity to nearby atoms due to strong dipole-dipole interaction [16, 17, 18, 19, 20, 21, 22]. These interactions will be defined and will be discussed in more detail in forthcoming chapters. However, this same sensitivity to other Rydberg atoms and/or their environment hampers their ability to function correctly as quantum gates. This dissertation focuses on how Rydberg atoms are affected by each other and their environment, and how active control methods can be used to reduce or eliminate unwanted interactions. The results that reveal sources of, and cures for, dephasing/decoherence might be very valuable to the realization of quantum computers/simulators using Rydberg atoms. Moreover, the principles of dephasing/decoherence, and their foils, are to some degree universal, thus the results described here may be applicable in other quantum systems as well, like ion traps [23] and superconducting circuits [24], and more generally to quantum control problems beyond quantum computation and simulation.

1.1 Atomic Units

Atomic units are a system of natural units of measurement which are especially convenient for atomic physics and computational chemistry [25]. Atomic units are defined by setting the values of the reduced Planck constant, elementary charge, Bohr radius, and electron mass to unity

$$\hbar = e = a_0 = m_e = 1. \tag{1.1}$$

From there, other units like energy, time, and electric field can be defined on a scale relevant to typical parameters and processes. Some physical units used in this dissertation can be converted between SI and atomic units using Table 1.1 [26].

1 atomic unit	Value in SI units
Length	$5.29177210903(80) \times 10^{-11}$m
Velocity	$2.18769126364(33) \times 10^{6}$ m·s^{-1}
Energy	$4.3597447222071(85) \times 10^{-18}$ J
Electric field	$5.14220674763(78) \times 10^{11}$ V·m^{1}
Time	$2.4188843265857(47) \times 10^{-17}$ s

Table 1.1: Atomic units.

1.2 Rydberg Atoms

Rydberg atoms are atoms in which one electron is excited to a state with a large principal quantum number (n>10) [27]. In the experiments discussed in this dissertation, the outermost electron of individual ^{85}Rb atoms ($5s$ ground state) is excited to an n~30 state. In general, because of their large electron orbits (with mean radii $R \propto n^2$), and small binding energies ($W \propto n^{-2}$), Rydberg atoms have unique and exaggerated properties.

Because the outermost electron is far from the nucleus or any other electrons, in many aspects Rydberg atoms essentially behave like Hydrogen atoms, with the addition of core polarization and penetration effects due to the non-hydrogenic ion core. Those effects can be viewed as perturbations to the Hydrogen atom, resulting in modified eigenenergies and wavefunctions, characterized by a quantum defect. The quantum defect can either be calculated

or experimentally measured [28]. Once obtained, most properties of Rydberg atoms like their bare energy level structure and electronic wavefunctions can be readily computed.

The experiments described in this dissertation utilize external electric fields to manipulate Rydberg electrons. In the presence of external electric fields, the zero field angular momentum eigenstates $|nlm\rangle$ are coupled via matrix elements of the form, $\langle nlm| Ez |n'l'm\rangle$. Here E is the external electric field which defines the axis z for atom. In general, the electric field alters the Rydberg eigenstates and their associated eigenenergies, through the Stark effect. In the experiments described in this dissertation, the applied electric field are relatively weak, such that the electric field induced couplings between Rydberg states are small compared to the zero field splitting between those states. As a result, the resulting Stark shifts are second order in the field, and the eigenstates are approximately equal to those in zero field. Accordingly, we refer to the Stark shifted states using their field free, angular momentum eigenstate labels, and compute the matrix elements relevant to interactions between Stark tuned atoms using the zero field states.

Given the large size and dipole moment of Rydberg atoms, strong interactions between Rydberg atoms can be expected. In the physical regime of the experiments in this dissertation, where the interatomic distances are ~5μm and the diameter of the low angular momentum n~30 Rydberg atoms we study is ~100nm, the dominant interaction between Rydberg atoms is electric dipole-dipole ($\propto R^{-3}$).

1.3 Dipole-Dipole Interaction and Resonant Energy Transfer

It is well known that two molecules (or two excitation centers within a single larger molecule) can exchange electronic energy through nonradiative dipole-dipole coupling. If the process is resonant, with one excitation center acquiring precisely the same electronic energy that was lost from the other, the process is commonly referred to as Förster resonance energy transfer (FRET) [29]. Similar couplings and resonant energy transfer processes can happen between atoms. A transition dipole moment $\overrightarrow{\boldsymbol{\mu}} = e\langle\overrightarrow{\boldsymbol{r}}\rangle = e\,\langle nl|\,\overrightarrow{\boldsymbol{r}}\,|n'l \pm 1\rangle$ exists between any two electronic states of an atom for which the angular momentum quantum number l differs by one. Thus, a pair of atoms can also excite/deexcite through a nonradiative dipole-dipole coupling

$$V_{DD} = \frac{\overrightarrow{\boldsymbol{\mu_1}} \cdot \overrightarrow{\boldsymbol{\mu_2}} - 3\left(\overrightarrow{\boldsymbol{\mu_1}} \cdot \hat{\boldsymbol{R}}\right)\left(\overrightarrow{\boldsymbol{\mu_2}} \cdot \hat{\boldsymbol{R}}\right)}{R^3}, \tag{1.2}$$

where $\overrightarrow{\boldsymbol{\mu_1}}$ and $\overrightarrow{\boldsymbol{\mu_2}}$ are the transition dipole moments within atoms 1 and 2, respectively, and $\overrightarrow{\boldsymbol{R}}$ is the position of the nucleus of one atom relative to the other. As alluded to above, it should be noted that dipole-dipole coupling approximation works only for cases where the interatomic distance is much greater than the size of an atom (~5μm vs. ~100nm as is the case for the experiments in this dissertation). Otherwise, higher order couplings play a role, and it may not be sufficient to describe the state of the outermost electron in each atom using simple Rydberg atom orbitals. If one or both Rydberg

electrons are subject to the potential of both nuclei (with similar strengths), hybrid (molecular) orbitals need to be considered to describe the system accurately.

When the excitation/deexcitation energy of the pair of atoms are closely matched, resonant energy transfer can occur. Dipole-dipole interaction mediated resonant energy transfer process are affected by a variety of factors, such as distance between atoms, the transition dipole moment strength, and the energy difference between "donor" and acceptor transitions [27]. Details of the process can be found in later chapters.

Rydberg atoms are good candidates for studying dipole-dipole interactions in general [16, 17, 18, 19, 20, 22, 30, 31, 32, 33, 34, 35, 36], including dipole-dipole interaction mediated resonant energy transfer. The transition dipole moments between Rydberg states can be very large, the distance scale between Rydberg atoms can be varied by changing the density of an atom cloud, or precisely tuned with optical tweezers [21], and the energy difference between donor and acceptor transitions can be broadly tuned with applied electric fields via the Stark shift.

1.4 Evolution of Quantum State in a Rydberg Atom Gas Ensemble

In a two-state quantum system ($|0\rangle$ and $|1\rangle$), a particle, such as an electron in an atom, can occupy both states at the same time. When the energies of the two states are different, the evolution of the quantum phase occurs at different

rates for the two levels. Arbitrarily assigning the energy (and phase) of state $|0\rangle$ as 0, one can write the state of the electron in an atom as

$$\Psi = a_0 |0\rangle + \sqrt{1 - a_0^2} e^{-i\phi(t)} |1\rangle , \tag{1.3}$$

where a_0 is the amplitude of state $|0\rangle$, and the phase difference between the two states is $\phi(t) = \phi_0 + \int E(t)dt$. The rate of phase evolution is governed by the energy difference E between the two states.

For a pair of Rydberg atoms subject to dipole-dipole interactions, the degeneracy of single Rydberg atom excitation is broken, creating two new eigenstates of the atom pair, shifted from twice the single atom excitation energy by $\pm V_{DD}$. As previously discussed, V_{DD} is dependent on the interatomic distance as well as the transition dipole moments (both strength and relative orientation) of the two atoms. In some situations, a large Rydberg gas ensemble can be approximated as many isolated pairs of atoms, or many smaller ensembles of atoms (more detailed discussions in Chapter 3). In the presence of strong dipole-dipole interactions between neighboring atoms, the energies of the eigenstates within isolated pairs or ensembles is shifted, depending on interatomic distance, relative atom orientations, etc. Because neither interatomic distances nor relative atom orientations is uniform throughout a random ensemble of Rydberg atoms, the dipole-dipole energy shifts within each atom pair or micro-ensemble, relative to twice the single atom excitation energy, is also not uniform, creating a different phase evolution in different local ensembles, ultimately leading to a (nearly) random phase distribution across

the ensemble as a whole. In addition to this "dephasing", due to atom motion and/or fluctuating external fields, interatomic distances, relative atom orientations, and pair energies are time dependent, meaning the phase evolution is time-dependent and depends on the coupling of the electrons to other (unmeasured) degrees of freedom. These environmental couplings lead to decoherence within the local atom ensembles, in addition to the time-independent energy inhomogeneities which cause dephasing. In later chapters, more detailed models of dephasing and decoherence, as well as methods to alleviate them, will be presented.

1.5 Dissertation Structure

The remainder of this dissertation consists of six chapters. Chapter two describes the apparatus used for the experiments discussed in subsequent chapters, and in part serves as a lab manual for maintenance of the apparatus. Chapter three describes how Rydberg gases can be mathematically modelled, from a simple two-atom two-state picture, to fully interacting four atom systems including electronic fine structure. Chapter four shows how pulsed electric fields, in a sequence that was first introduced by Kutteruf and Jones for measuring the coherence time of dipole-dipole coupled Rydberg atoms in a random ensemble [37], can be employed to actively suppress macroscopic dephasing in the same system. Moreover, it includes a theoretical discussion of how such a sequence could be used to suppress dephasing in more ordered systems as well as actively reduce microscopic decoherence rates associated

with time-dependent electronic energy variations. Chapter five explores two main sources of dephasing, inhomogeneity and hopping of Rydberg excitation and, by comparing experimental and simulation results, considers the conditions under which hopping can be reasonably ignored. Chapter six utilizes simulations to explore population transfer dynamics in non-Hermitian systems subject to control loops which adiabatically change the coupling and energy separation that define a two level system. Chapter seven summarizes the results reported in the dissertation and prospects for future work.

Chapter 2

Experimental Setup

The experiments described in this dissertation involve exciting and detecting Rydberg atoms within a cold ^{85}Rb ensemble. In this chapter, the three main components of the experimental apparatus are described: Laser systems, Electronics systems and Vacuum systems. The Magneto-Optical Trap (MOT) which is responsible for producing the cold ^{85}Rb ensemble, and combines the capabilities of all three systems, is then described in detail, from its operation principles to characterization. Lastly, the data collection process is briefly introduced.

2.1 Experimental Environment

All experiments described in this dissertation were performed in Room 166 of the Physics Building at University of Virginia. The HVAC system is designed to maintain lab temperature around ~72°F, with the controlling thermostat

sitting directly above the MOT. In practice, because the temperature control system only reads the temperature at two locations within lab, temperature gradients cannot be prevented and the gradient will differ depend on outside temperature. The humidity of air coming out of HVAC system is not controlled beyond maintaining a dew point several degrees below the lab temperature. Even though dehumidifiers in the lab can help control local humidity level, a gradient of humidity cannot be prevented. With these factors combined, the day to day consistency of the lab environment is not guaranteed and experiments are always recommended to be performed on non-rainy days without large day and night temperature fluctuation. Bluetooth and USB based temperature and humidity sensors are purchased on Amazon to monitor environmental conditions throughout the room.

2.2 Laser Systems

Lasers in our experiments are responsible for reliably transferring atom population from one state to another, and ideally without excitation of atoms into any other states, while remaining at a relatively constant intensity thus constant population transfer rate. Moreover, the flexibility of turning on and off laser excitations (within ~100ns) is required. To meet those criteria, the laser systems utilize the following components.

2.2.1 External-Cavity Diode Lasers

External-Cavity Diode Lasers (ECDL) are widely used in modern laboratories for their ease of maintenance and good stability. In an ECDL, a laser diode is used as the gain element, and is incorporated within a tunable resonant cavity to complete a laser system. The two laser systems utilized in this dissertation both use angular dispersion from a diffraction grating to provide wavelength selectivity [38, 39, 40, 41, 42, 43, 44]. For the ECDLs used in this dissertation, one end of the laser diode chip has a high reflective (HR) coating, forming one end of the resonant cavity while the other end of the laser diode chip has antireflective (AR) coating to prevent the diode chip itself from acting like a resonant cavity. The light from diode chip is then collimated using a lens and directed onto the diffraction grating. In the Littman-Metcalf design (used by our New Focus lasers), the other end of the resonant cavity is a rooftop prism which reflects the first order diffraction off the grating to provide feedback. In the Littrow-Hänsch design (used by the Toptica laser), the diffraction grating itself serves as one end of the resonant cavity, sending the first order diffraction back into the diode to provide feedback. In both cases, the angle of the retroreflecting element (prism or grating) can be coarse tuned by hand and fine-tuned with a piezoelectric actuator for frequency selection. For any selected angle within the large first order dispersion angular range, only a narrow spectrum is retro-reflected and amplified. With this narrow band feedback, the zero-order diffraction of the grating serves as the output beam of laser. In the Littman-Metcalf design, the zero-order diffraction is

angle independent, in the Littrow-Hänsch design, an output coupling mirror rotates as the grating rotates to ensure that the output beam is grating angle independent.

Additionally, to guarantee good feedback and mode-hop free operation, the cavity length needs to vary with the wavelength of the laser. Specifically, the cavity length needs to relate to the feedback angle of diffracted beam as

$$L(\theta_d) = \frac{N\lambda(\theta_d)}{2} = \frac{N\Lambda(\sin\theta_i + \sin\theta_d)}{2}, \tag{2.1}$$

where L is the cavity length, N defines the cavity mode (which should not change in a mode-hop free laser), Λ is the groove spacing of diffraction grating, and θ_i and θ_d are the angle of incidence and diffraction relative to the grating normal. This condition can be achieved by carefully selecting the pivot point of retroreflector. In the Toptica laser, the current to the laser diode also changes in a synchronized way as the grating and output coupler rotates to change the index of refraction of the semiconducting lasing material, thus matching the internal resonator length with external cavity length, giving a large mode-hop free range.

Three ECDLs are used in the experiments described in this dissertation. Two of them are New Focus TLB 7000 lasers tuned near ~780nm, which act as (and will be referred in this dissertation as) the trap and repump lasers for the Magneto-Optical Trap (MOT). They are responsible for driving the $5s_{1/2}, F = 3$ to $5p_{3/2}, F = 4$ (with ~30MHz redshift), and $5s_{1/2}, F = 2$ to $5p_{3/2}, F = 3$ transitions in ^{85}Rb, respectively. Typically, the trap laser operates

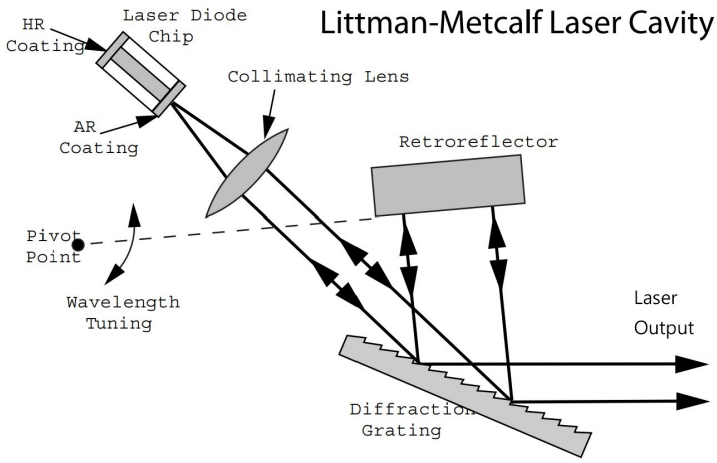

Figure 2.1: Principle of operation for the Littman-Metcalf ECDL design [2].

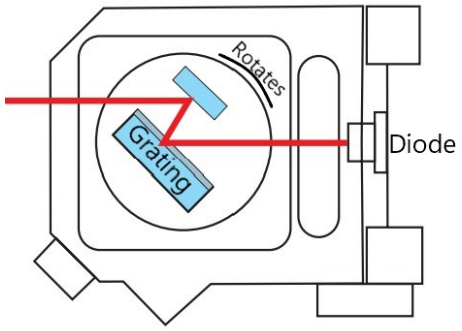

Figure 2.2: Principle of operation for the Littrow-Hänsch ECDL design [3].

at 89.5mA and has 39mW of laser output, the repump laser operates at 81.5mA and has 23mW of laser output. The voltages on the piezoelectric actuators that adjust the retroreflecing prism angles in both lasers are tuned on a daily basis to account for frequency drifts.

The other ECDL used in this dissertation is a Toptica DL pro laser within the Toptica SHG pro laser system. The 964nm beam from Toptica DL pro is sent through a tapered amplifier, where the size of the beam is gradually increased so that the beam interacts with a larger gain region as it propagates to efficiently amplify beam power. After the tapered amplifier, the energy of the 964nm beam can reach up to 635mW. To facilitate Rydberg excitation from $5p$ to n~30, the output of the tapered amplifier is frequency doubled, as discussed in next section.

2.2.2 Second Harmonic Generation

The emission frequency range of a diode laser is determined by the band gap of the p-n junction in the diode [45, 46], which usually lies in the infrared regime. To extend the frequency range of diode lasers, non-linear frequency-mixing techniques can be used to convert the coherent infrared radiation produced by diode lasers to desired frequencies. For excitation from $5p$ to n~30 in Rb, the required wavelength is ~480nm. Narrow band CW laser light at this wavelength can be obtained by frequency doubling a ~960nm CW beam in a non-linear crystal. Here two infrared (e.g., 964nm) photons are annihilated, to create a single blue (482nm) photon. To achieve maximum conversion frequency, the Toptica SHG Pro employs a bow-tie-ring second harmonic genera-

tion (SHG) cavity with frequency doubling crystal [47]. The SHG cavity length is stabilized using the Pound-Drever-Hall(PDH) technique [48, 49], where the cavity length is modulated, creating sidebands symmetrically centered around the central frequency of fundamental laser (964nm). A fraction of the 964nm laser within the SHG cavity is sent to a fast photodiode, where the intensity of the two sidebands are compared. The power in the two sidebands should be equal if the cavity length provides minimum loss at the central fundamental frequency, otherwise the signal difference between the two frequencies provides feedback into the piezoelectric actuator which controls the length of SHG cavity.

After a decade of operation, the angle and position of the frequency doubling crystal may need tuning on a day to day basis due to damage in the anti-reflection coating on the face of crystal, and loosening of mounts. The mirrors on the edge of SHG cavity may also need tuning, although a lot less frequently. The internal oscillator amplitude for PDH locking can also be fine-tuned to maximize laser output power. A pair of prisms after the SHG cavity can be utilized to optimize the spatial beam profile but is currently not in use due to power loss. Currently, with a properly tuned SHG cavity, the system is capable of outputting 130-140mW of blue (482nm) light. This completes the operation principle and maintenance of Toptica SHG pro laser (referred to as the blue laser in this dissertation).

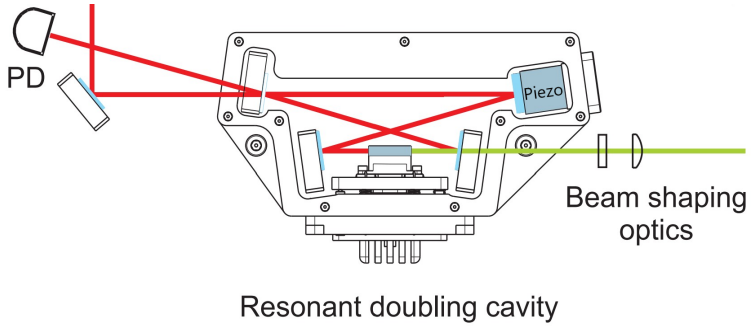

Figure 2.3: Principle of operation for second harmonic generation (SHG) within SHG cavity of blue laser [3].

2.2.3 Frequency Locking with Feedback Circuit

Limited by the design of the tunable external cavity, the stability of a standalone ECDL may not be sufficient to maintain the output frequency within atom linewidth precision over long periods of time (hours in the case of experiments in this dissertation). Thus, to further increase the stability, the ECDLs are frequency-locked to external sources. To achieve frequency locking via a feedback circuit, a signal that varies monotonically as a function of frequency is required. Such a signal can be one side of a transmission peak in a Fabry-Pérot cavity as its length is scanned, or one side of the absorption peak of an atomic transition as the laser frequency is scanned. The feedback circuit compares the signal size with a desired value, usually midway through the slope, via an op-amp. Any difference in the amplitude of the signal relative to the reference is then amplified, and fedback into the control piezo of the ECDL, adjusting the output frequency of the laser correspondingly. Taking things a step further, the time integral, and derivative of the difference signal can be used in addition to the proportional feedback, for better locking. This

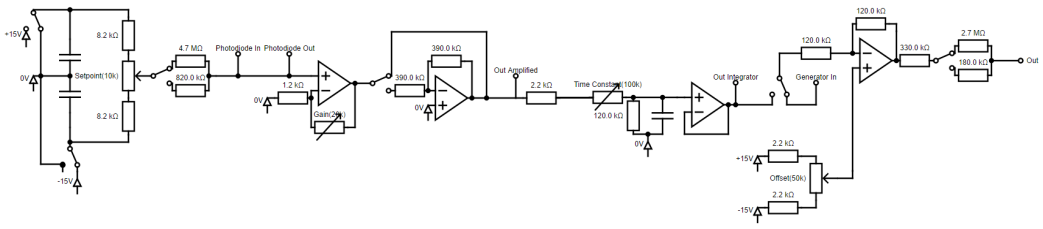

Figure 2.4: Circuit diagram of the homemade feedback circuit for frequency locking of the infrared trap and repump lasers.

is known as PID (proportional–integral–derivative) control [50].

For the trap and repump lasers, the laser frequency is locked to the falling edge (as frequency increases) of the ^{8}5Rb $5s_{1/2}, F = 3$ to $5p_{3/2}, F = 4$ and $5s_{1/2}, F = 2$ to $5p_{3/2}, F = 3$ transitions, respectively, using saturated absorption spectroscopy (discussed below) and a proportional feedback circuit. The blue laser frequency is locked to the error signal of a Fabry-Pérot Interferometer (FPI) (ThorLabs SA200-3B), the length of which is tunable by a piezoelectric actuator. The ThorLabs TPZ001 piezo driver applies a static voltage to the piezoelectric actuator to define a cavity length, and the ThorLabs SA201 Spectrum Analyzer Controller sends a triangular wave on top of the static voltage to modulate the length of Fabry-Pérot cavity. A photodiode measures the transmitted light through the cavity. The change in the amplified photodiode output voltage provides an error signal that is sent to the Toptica PID110 module locking the frequency of the master diode laser onto the falling edge (as frequency increases) of the amplified error signal.

2.2.4 Saturated Absorption Spectroscopy

In saturated absorption spectroscopy, a small fraction (4%) of the laser output (both trap and repump lasers) is sent to a Rb vapor cell, serving as the "pump beam". After passing through the Rb cell, roughly 4% of the pump beam is retro reflected through the cell, serving as a probe, and is incident on a photodiode. When the lab frame frequency of the laser is tuned so that some atoms are excited from a $5s$ to $5p$ state, fewer atoms are available to absorb light from the probe, resulting in increased probe transmission through the cell. By exposing atoms to light travelling in opposite directions, the Doppler shift can be eliminated since only two kinds of atoms will absorb both beams (depending on the common frequency of the two beams in the lab frame): (1) Those that are not moving will see the pump and probe beams at the same frequency and will absorb light only if it is resonant with a $5s$ to $5p$ transition (producing a direct absorption peak in the probe beam transmission vs. laser frequency); and (2) Those moving at a particular velocity such that the pump beam is on resonance with one transition and the probe beam is on resonance with another transition (producing a cross-over peak in the probe transmission spectrum). Because of this, saturated absorption provides a straightforward Doppler-free spectroscopic tool for laser frequency locking.

To reduce the effect of laser power variations that would result in error signal fluctuations not related to changes in the probe absorption, the feedback signal is based on a differential input. Dual photodiodes in a push-pull configuration provide a voltage signal proportional to the difference in the power

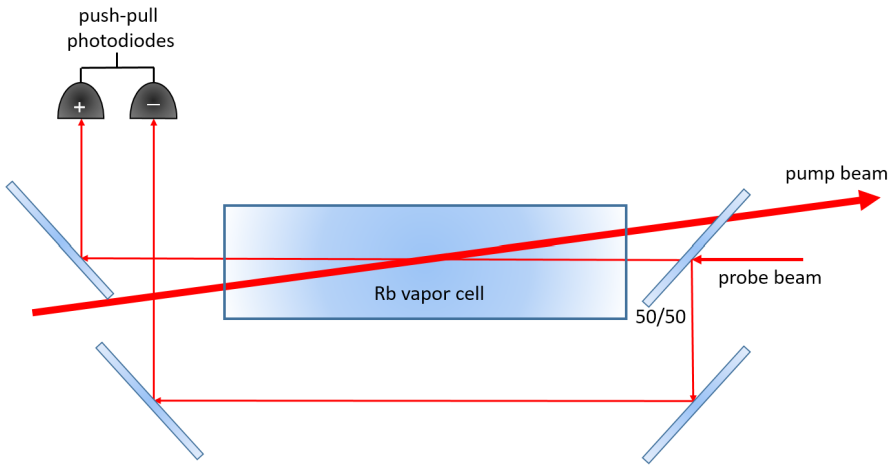

Figure 2.5: Saturated Absorption Spectroscopy.

of the probe beam and that of a second reference beam that does not pass through the pumped volume of the vapor cell. In practice, this is achieved by passing the retro-reflected pump beam through a 50/50 beam splitter, one beam through the vapor cell into one photodiode, and the other beam directly into the other photodiode.

The trap and repump beams for the Magneto-Optical Trap (MOT) are locked ~30MHz redshifted from $5s_{1/2}, F = 3$ to $5p_{3/2}, F = 4$, and locked to the $5s_{1/2}, F = 2$ to $5p_{3/2}, F = 3$ transitions, respectively. In practice a portion of the trap laser is first redshifted by ~30MHz, then locked to the crossover peak of $5s_{1/2}, F = 3$ to $5p_{3/2}, F = 4$ and $5s_{1/2}, F = 3$ to $5p_{3/2}, F = 4$, which is ~60MHz redshifted from $5s_{1/2}, F = 3$ to $5p_{3/2}, F = 4$. Since the MOT holds cold atoms which move slowly and do not suffer from significant Doppler shifts, Doppler-free saturated absorption spectroscopy is ideal for providing the required laser frequency references for the MOT setup. The falling edge of either transition

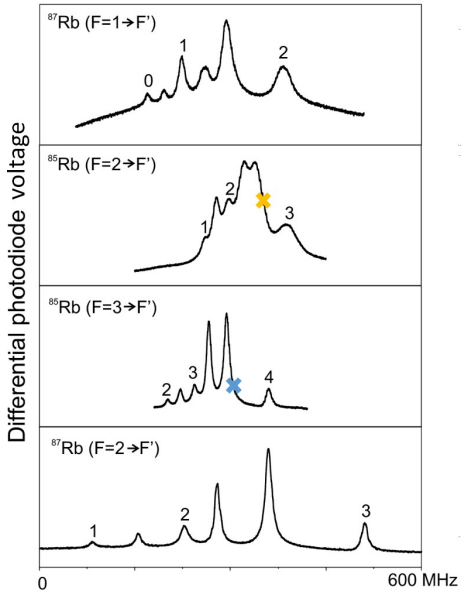

Figure 2.6: Saturated Absorption Spectroscopy signal of ^{85}Rb and ^{87}Rb. The blue cross marks the locking point for the trap laser (edge of the crossover peak of $5s_{1/2}, F = 3$ to $5p_{3/2}, F = 4$ and $5s_{1/2}, F = 3$ to $5p_{3/2}, F = 4$) while the yellow cross shows the locking point for the repump laser (edge of the $5s_{1/2}, F = 2$ to $5p_{3/2}, F = 3$ transition) [51].

is sent to the frequency locking feedback circuit described earlier. Proper detuning of trap beam, essential for MOT operation (as discussed later), is achieved with an Acousto-Optic Modulator (AOM).

2.2.5 Acousto-Optic Modulator

Acousto-Optic Modulators (AOM) serve two purposes in the experiments, the trap laser AOM is in continuous operation and provides a constant frequency shift from the locking frequency as discussed earlier. For the blue laser, the AOM serves as a fast optical switch. As the title of the dissertation suggests, interactions between atoms, rather than between atom and laser, is our pri-

mary concern in this dissertation. Thus, the excitation of atoms from the upper trap state $5p$) to a Rydberg state (n~30) is required only for a brief amount of time. In addition, the use of rapid Rydberg excitation and relatively short Rydberg-Rydberg interaction times reduces the impact of unwanted Rydberg population transfer via collisions and van der Waals interactions.

In our AOMs, a piezoelectric transducer is attached to a quartz crystal. An oscillating electric signal drives the transducer to vibrate, which in turn creates sound waves in the quartz. The standing wave in the quartz compresses and expands it at different locations, resulting in a periodic change in the index of refraction so that the quartz crystal behaves like a diffraction grating. As such, the AOM can deflect an incident laser beam into the first (or higher) diffraction orders, and the frequency of the diffracted beam is the sum (or difference) of the input laser frequency and the transducer frequency. Using our AOMs, a maximum conversion efficiency of ~70% of the input power into first order beam can be obtained. Another way of understanding the working principle of AOM is a three-wave mixing process, where sum-frequency generation or difference-frequency generation between phonons and photons creates new photons. At a specific deflection angle where a phase-matching criteria is met($\overrightarrow{\boldsymbol{k_{input}}} \pm \overrightarrow{\boldsymbol{k_{phonon}}} = \overrightarrow{\boldsymbol{k_{output}}}$), the conversion efficiency is high, resulting in a macroscopically deflected beam.

In continuous operation, the 1st order beam is utilized to provide a constant ~30MHz redshift to the portion of the trap laser beam used for saturated absorption locking (the portion used for trapping is not subject to the frequency shift), the red shifted portion is locked onto a crossover peak ~60MHz red-

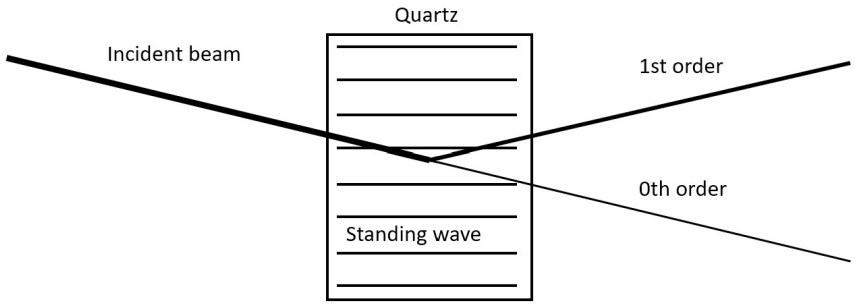

Figure 2.7: Acousto-Optic Modulator (AOM).

shifted from $5s_{1/2}, F = 3$ to $5p_{3/2}, F = 4$ transition, meaning the trap laser is ~30MHz redshifted from the transition (the reason for redshift will be discussed later). When operating as an optical switch, by switching on and off the RF input to the transducer, the 1st order beam can be turned on and off. In practice on/off switching times as short as 100ns for 1st order beam can be achieved, enabling the creation of 300ns pulses to excite atoms into Rydberg states. Notably, despite the loss in peak power, use of the 1st order diffracted beam rather than the modulated 0th order beam, is essential for the Rydberg excitation. This ensures that there is no Rydberg excitation when the excitation pulse is nominally off, preventing continuous Rydberg excitation, redistribution, and ionization.

2.3 Electronics Systems

The eigenstate energies of Rydberg atoms are modified in external electric fields due to Stark effect. In our experiments, a high fidelity (small inhomo-

geneity, quick turn on/off time) electric field generation device is incorporated to shift Rydberg atom energies as we desire. Moreover, we use field ionization for state-selective detection of Rydberg atoms, requiring a strong and consistent ionizing field ramp as well as a sensitive ion detector. The timing of distinct steps within each individual measurement, including laser excitation, electric field pulses and ramps, etc., are precisely synchronized by a digital delay generator.

2.3.1 Voltage Generation

To produce high fidelity electric fields, electronics capable of producing high fidelity time-dependent voltages are needed. Two voltage generation subsystems are connected to two stainless steel plates which straddle the laser-atom interaction region and define the time-dependent electric fields in the experiments. The first subsystem is an Arbitrary Waveform Generator (AWG, Tektronix AWG 510), which is capable of generating arbitrary time-dependent voltages, between $\pm$2V with a fidelity of 1mV, in 1ns time-bins. Due to nonzero capacitance and resistance of the stainless steel plates, the actual response time for voltage change on plates is ~2ns. The AWG defines the time-dependent Stark shift and state composition of the Rydberg atoms excited in the MOT. The second subsystem is based on a trigger transformer circuit and enables the application of a DC voltage bias (via BK Precision BK1762 Power Supply) and a HV ionizing field ramp (discussed later) to the Rydberg atoms.

2.3.2 Electric Field Generation Plates

While electronics are capable of producing voltage signals, those voltages need to be applied to a pair of parallel field plates to produce spatially uniform electric fields throughout the laser-atom interaction region. For our experiments, a simple set of two solid parallel plates is not suitable because the operation of the MOT and Rydberg excitation requires lasers to enter the interaction region from at least six different directions along three (nearly) orthogonal axes. Accordingly, the conductors that define the field must accommodate the passage of the laser beams as well as ions moving from the interaction region to detector.

Previous cold Rydberg atoms experiments in the lab have utilized 4 parallel stainless steel rods to define the electric field within the MOT. However, the rods did not completely shield the atoms from stray fields due to high voltage contacts on the MCP detector, and the experiments were affected by the intrinsic field inhomogeneities produced by the rods. An alternative setup we have tried with limited success is two parallel mesh held in place by solid stainless steel frames. Although the mesh provided up to 97% light transmission, the ordered wire array resulted in significant degradation of two of the three retro-reflected MOT beams and substantially reduced MOT performance. Eventually, we carefully calculated the paths of MOT beams as well as the ion extraction path, and developed a new field plate design with clear holes at the appropriate locations so that the lasers and ions were not hindered. The plate voltages are fed into the vacuum chamber via Kapton insulated wires and

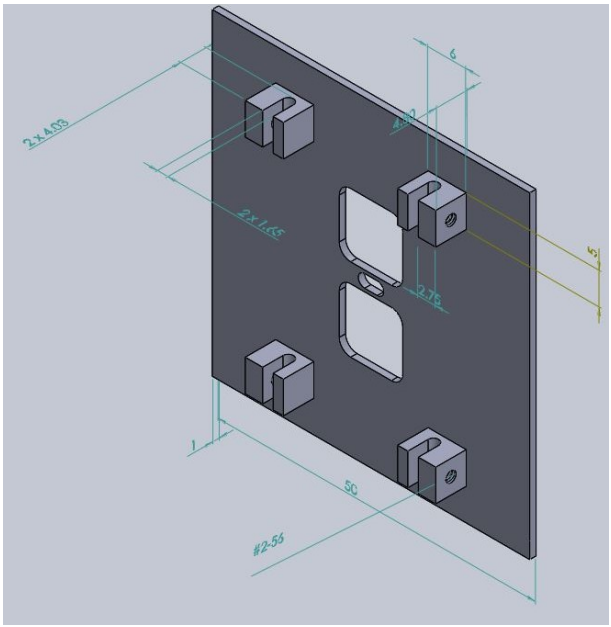

Figure 2.8: CAD design of one of the electric field generation plates.

stainless steel rods. The two stainless steel parallel plates are clamped onto the original parallel field rods using stainless steel screws, ensuring electrical contact. The performance of the plates was analyzed with COMSOL Multiphysics finite element analysis (FEA) software. The software suggests that the field inhomogeneity within the 1mm×1mm×1mm volume at the center of the vacuum chamber (where the MOT is located) is <0.5%, and that the electric field within trapped atom region should be, $F = V_{diff} * 0.92/\text{cm}$, where V_{diff} is the voltage across the two electric field generation plates.

2.3.3 State-selective Field Ionization

Field ionization is an efficient and widely used tool to detect and distinguish population in different Rydberg states [52]. When the ionization field is ap-

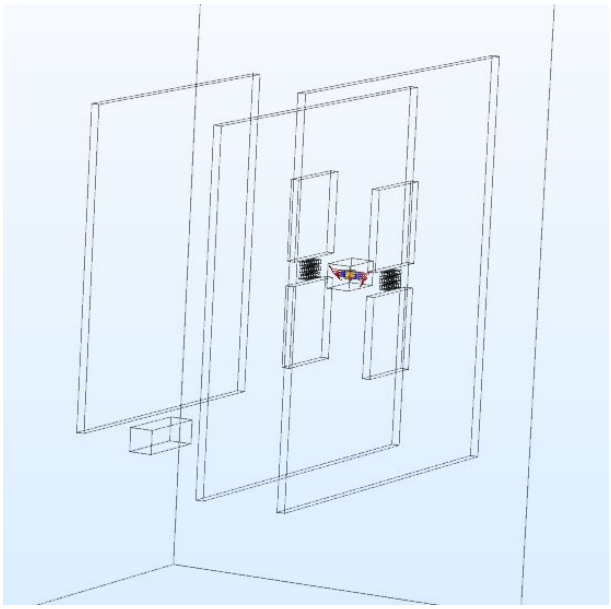

Figure 2.9: Finite Element Analysis (FEA) of field inhomogeneity near the MOT area.

plied as a pulse, with rise times of nanoseconds to microseconds [53, 54, 55], detection selectivity can be achieved as different Rydberg states ionize at different times during the rise of the field. While the physical process of field ionization of Rydberg atoms can be very complicated and has given birth to a field of research in itself, for the purpose of our experiments, we only rely on qualitative aspects of pulsed field ionization. Namely, Rydberg states that are higher in energy in zero or small electric fields will be ionized earlier in a slowly rising (adiabatic) field pulse, such that the probability of finding atoms in Rydberg states of different energies is mapped to the time of ionization in the field. This is known as state-selective field ionization (SSFI). It should be noted that due to mixing of Stark manifolds at strong electric fields, ions originating from different states may overlap in the time-dependent ion signal

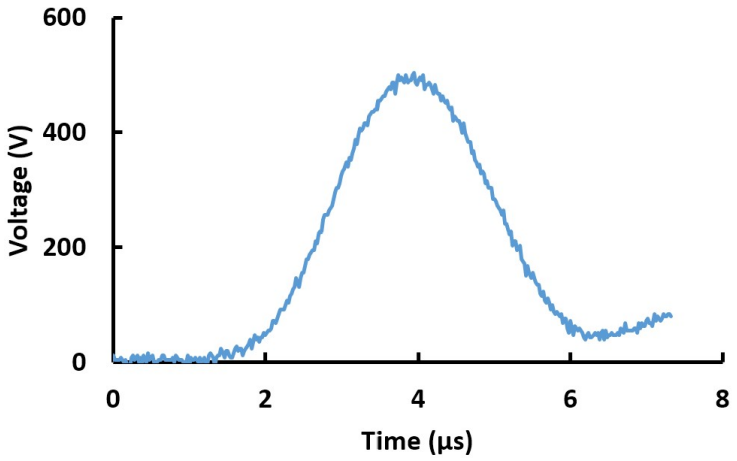

Figure 2.10: Time-dependent voltage pulse from the trigger transformer measured using a Tektronix P6015A high-voltage probe. When applied to the field plates, similar pulses enable state-selective field ionization (SSFI) detection.

from the detector, thus in practice it is almost impossible to precisely resolve and accurately assess the population in all states without careful engineering of the ionization field ramp [56, 57, 58]. However, by focusing on the portions of the time-dependent ionization traces where population is dominated by ions originating from one state, it is still possible to determine the relative change of the population in different states.

In this dissertation, SSFI is achieved with a trigger transformer, which produces a ~2μs rise-time high-voltage (HV) pulse, the amplitude of which is tunable using an external voltage source (BK Precision BK1762 Power Supply), when it receives a TTL trigger from the delay generator. The HV pulse enables us to ionize n~30 Rydberg atoms and provide partial energy resolution for different Rydberg states ($32p_{3/2}, |m_j| = 3/2$ and $33s_{1/2}$, in particular) initially in a small or zero electric field.

2.3.4 Micro Channel Plate Detector

After field ionization, the resulting Rb^+ ions are pushed by the ionizing field toward a dual microchannel plate (MCP) detector. The MCP functions as a particle amplifier, converting each incoming Rb^+ ion into a pulse of electrons, which can then be collected on the detector anode as a negative voltage pulse.

Each MCP is an array of tiny glass tubes or slots (microchannels) leading from one face to the opposite. When ions strike the glass wall of a MCP microchannel, electrons are released from the electron-donating material on the wall surface of the microchannel. The electrons are accelerated in a strong electric bias field placed across the MCP, and hit the microchannel wall multiple times, releasing more electrons upon each impact until reaching the other end of the microchannel [4]. The resulting electron bunch exiting the channel has sufficient charge to be detected through the transient change in voltage on the collection plate or anode. The anode is held at a bias voltage of 100V relative to the back plate of the chevron stacked MCP pair, pulling electrons toward the anode. The electrons deposited on the anode temporarily reduce its voltage. The time-dependent voltage change is measured with an oscilloscope. Provided the electron gain is not saturated, the area of the voltage pulse is proportional to the number of Rb^+ ions produced by field ionization at a certain time (field strength).

The MCPs require no special maintenance, only turning off the high voltage across MCP when not running experiments and always storing MCPs in vacuum. One special note on the use of MCPs with SSFI is signal bleaching.

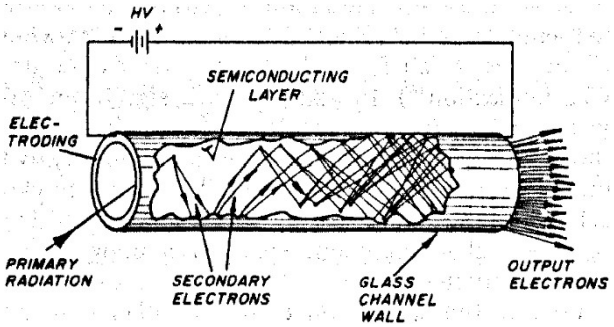

Figure 2.11: Micro Channel Plate Detector at work. [4]

After an ion creates an electron shower within a microchannel, some relaxation time is needed before the microchannel walls are fully charged again. Accordingly, the signal gain can be reduced if additional ions strike the same channel during the relaxation time. In SSFI, especially in cases where large numbers of ions are created, consecutive batches of ions (representing populations in different states) can arrive at the MCP within the relaxation time, such that the latter batch of ions does not receive the same gain as the earlier one, complicating the analysis of population distribution in different Rydberg states, pre-ionization. Whether the system suffers from bleaching can be checked by changing the bias voltage across the MCP, which in turn changes the gain of the MCP and relaxation time, enabling one to determine if the relative sizes of the signals corresponding to population in two different Rydberg states remains the same.

2.3.5 Delay Generator

So far, several time sensitive events during the experiment have been introduced: Excitation of Rydberg atoms, Stark shift tuning, ionization, and de-

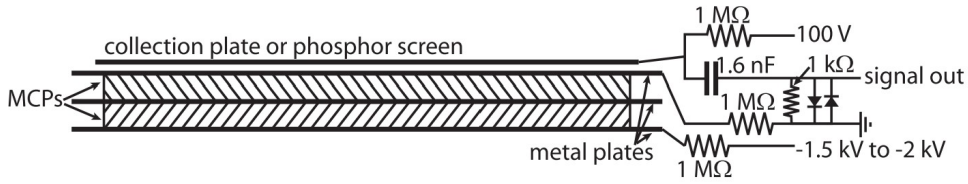

Figure 2.12: Ion detection setup in this dissertation, consisting of a pair of chevron stacked MCPs, a collection plate, and electronics to provide and detect voltages on those components [5].

tection. All these events are synchronized with a Stanford Research Systems DG645 delay generator, which is capable of producing 4 independent 0-5V trigger pulses of variable length and at arbitrary times relative to a master trigger. The DG645 has a relative temporal resolution of 5ps. In practical operation the delay generator itself is triggered at 15Hz by frequency dividing a reference pulse train from the 60Hz power line by a factor of four. This minimizes the impact of 60Hz AC line noise on experiments because the experiments are performed at the same phase of any 60Hz electrical noise. All the events listed below are triggered by a 4V TTL signal, with their corresponding detailed timing.

2.4 Vacuum Systems

The coherence inherent within quantum interactions between atoms is a fragile beauty. If exposed to background air molecules travelling at ~500m/s, the atoms in our experiments along with the coherences stored within/between them would be lost. To avoid this from happening, an ultra-high vacuum (UHV) system capable of achieving background pressures as low as 4×10^{-11}torr

Delay Generator Channel	Event	Timing	Length
AB		0(power grid)+108ns	10μs
EF	AOM on/off (excitation of Rydberg atoms)	A+10,276ns	300ns
GH	AWG pulse begin (tuning Stark shift)	F+1,108ns	10μs
CD	Ionization (of Rydberg atoms) / Oscilloscope refresh	C+280-780ns, depend on AWG pulse length	1.8μs

Table 2.1: Delay generator timing sequence, each letter represents a particular edge of a pulse, the two letters in one channel (e.g., AB) represent the timing for rising and falling edge of the pulse respectively.

is employed. The vacuum chamber (Kimball Physics MCF600-SS200408) is constructed from stainless steel. Flanges containing electrical feedthroughs and transparent windows for optical access are Conflat (CF), which use stainless steel knife edges to cut into copper gaskets to achieve tight seals. To compliment the ultra-high vacuum chamber, all materials within the vacuum chamber need to have as low outgassing rate as possible, including stainless steel, ceramic, Kapton (for insulation of cooper wires within chamber) as well as very limited use of silver paint. Electrical contacts are achieved with either metal screws or spot-welds, avoiding the use of soft solder.

To pump down to such a low pressure, a two-stage process is employed. The whole chamber can be connected to a TiTan 20S ion pump as well as a turbo pump backed by an oil free mechanical scroll pump. A UHV compatible valve is employed to allow the turbo pump to be connected/disconnected from the main chamber without compromising the high vacuum. In the first stage,

the turbo pump (backed by an oil free mechanical scroll pump) is connected to the chamber, pumping the chamber from atmosphere pressure down to $\sim 1 \times 10^{-8}$torr while the whole chamber is baked-out at ~150°C to release trapped gaseous molecules within the chamber. When the pressure of the chamber drops to $\sim 1 \times 10^{-8}$torr, the voltage across the MCP is gradually increased to its 2000V operating voltage to push out residual molecules within the channels. After outgassing the MCP, the valve connecting the chamber to the turbo pump is shut, and the chamber is allowed to return to room temperature before the ion pump is turned on. Eventually, with only the ion pump connected, the vacuum chamber reaches a steady state background pressure of 4×10^{-11}torr.

In normal operation, the turbo pump is then fully disconnected from the vacuum chamber, while the ion pump maintains the high vacuum.

2.4.1 Atom Source

Within the vacuum chamber, ^{85}Rb vapor for the experiments is generated using alkali metal dispensers (AMD) [59], more commonly referred to as "getters". Getters are made of an alkali metal chromate (Rb_2CrO_4) with a reducing agent, wrapped with a metal casing which has a trapezoidal cross-section with a slit to allow evaporation of alkali metal vapor. By controlling the current through the getter casing, the temperature of the reducing agent/chromate mixture is changed, thus controlling the evaporation rate of Rb atoms from within. In the experimental setup for this dissertation, 3 getters are spot-welded together in series, and the ends are then spot welded to two stain-

less steel clamps attached to ceramic posts. Two Kapton insulated wires are spot-welded to the stainless steel clamps, feeding current to the getters from a constant current power supply (HP 6282A) outside the vacuum chamber. Normal operation current is 1.8-2.3A yielding a typical Rb atom density in the MOT of $3 \times 10^9/\text{cm}^3$- $8 \times 10^9/\text{cm}^3$.

2.5 Magneto-Optical Trap (MOT)

To preserve coherence properties *between* atoms, in addition to keeping air molecules from hitting them, the atoms themselves also need to be cooled and trapped. Whereas Doppler free spectroscopy can be employed for experiments exploring properties of *individual* atoms, for experiments exploring many-body interactions *between* atoms, the configuration of the many body system should not change much from the beginning of the experiment to the end. That is, the atoms can move but not so fast that the relative atom separations at the end of each measurement are markedly different than at the beginning. In the experiments described in this dissertation, many body systems formed by ^{85}Rb atoms are observed for up to 15μs. At room temperature, ^{85}Rb atoms move at an average speed of ~300m/s, which means a typical room temperature ^{85}Rb atom can cover a distance of up to 4.5mm during the experiment, vastly exceeding the interatomic distance of ~5μm in the experiments. Accordingly, the strength of the interactions between individual atoms changes dramatically over time, better described in the context of collisions than controlled few or many-body physics. Fortunately, ensembles of cold atoms (moving at speeds

of ~0.1m/s) are relatively easy to produce since the introduction of MOT in 1987 [60]. We use a MOT to create cold ^{85}Rb samples for all of the experiments described in this dissertation.

2.5.1 Operation Principle

The quantitative details of MOT operation can get complicated very quickly, to the point that renowned Nobel Laureate in Physics W. Ketterle commented to his class, "I would actually say nobody fully understands the Magneto-Optical Trap." [61]. But qualitatively, the MOT is based on the simple concept of spatially dependent scattering radiation force: When an atom is off center in the trap, a scattered radiation restoring force is aimed towards the center.

The first ingredient of a MOT is a scattered radiation force [62, 63], which in itself can cool down atoms, leading to atom cooling techniques like optical molasses [64]. In laser beams, the travel direction of photons is well defined. When the energy of the photons in the beam is near resonant with an atomic transition, the atom can absorb the photon, and acquire its momentum. The same atom can then spontaneously emit a photon with the same energy in a random direction, transitioning back to the original state. After multiple absorption and emission cycles, the atom receives no net impulse from the random spontaneous emission events. However, during each absorption the atom's velocity changes by $h\nu/Mc$ in the direction of the cooling laser, where ν is the frequency of cooling laser, h is Planck's constant, c is the speed of light in vacuum, and M is the mass of the atom. If the laser is slightly red detuned (i.e., below the resonant frequency) in the lab frame, an atom travelling in

the opposite direction of the light in the cooling laser beam sees the laser frequency as closer to resonance, due to the Doppler effect. Accordingly, it will have a higher absorption rate than an atom travelling in the same direction as the laser light. By employing red detuned cooling lasers from all directions, atoms experience a significant damping force that opposes their motion in any direction.

While the radiation force provides cooling, it does not provide trapping. For trapping, a spatially dependent, rather than velocity dependent, scattering radiation force is needed. This is achieved using a spatially varying magnetic field. Through the Zeeman effect, the energy and resonant frequencies of atoms in the trap are position dependent. Therefore, the photon absorption rate, and average scattering force, is position dependent.

To understand the basic restoring force of the MOT, consider a 1D trap with a linearly varying magnetic field $B(z) = \gamma z$ where γ is a constant. For simplicity, we assume spinless atoms with a lower S state and a upper P state ($m_l = 0, \pm 1$). The resonance frequency of the S to P transition depends on z and the magnetic quantum number m_l of the P state. The energy detuning from the center of the trap at $z = 0$ can be written: $\Delta E = \mu m_l \gamma z$, where μ is the magnetic moment of P state. Again, utilizing a red-detuned laser, the transition from S to $P(m_l = 1)$ is closer to resonance at $z < 0$ while S to $P(m_l = -1)$ is closer to resonance at $z > 0$. Accordingly, if one adjusts the polarization of the incoming red-detuned laser light so that σ_+ polarized light travels along the $+z$ direction while σ_- polarized light travels along the $-z$ direction, then through the same photon scattering arguments presented

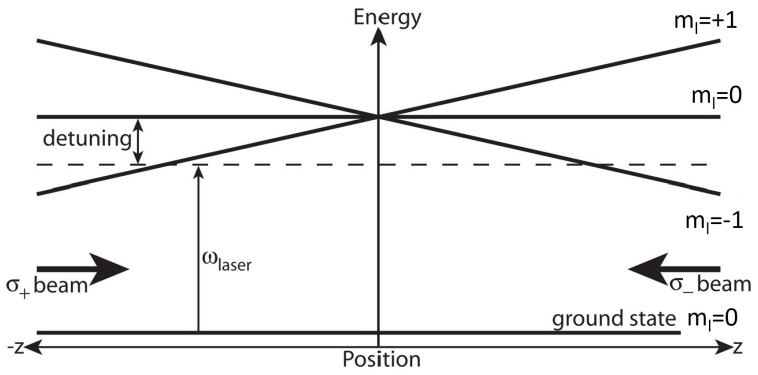

Figure 2.13: Energy diagram of one-dimensional MOT [5].

for atom cooling, any atoms with $z < 0$ will absorb more light from the σ_+ beam while those located at $z > 0$ will absorb more light from the σ_- beam. Thus, all atoms are simultaneously cooled and pushed toward the center of the trap at $z = 0$. For ^{85}Rb atoms, the lifetime of the $5p$ state is only 30ns, so atoms that are excited rapidly de-excite to $5s$ state and are again subject to the trapping forces. To extend the concept to three-dimensions, a pair of anti-Helmholtz coils is employed to provide a linear varying magnetic field in all three dimensions near the center of the coils, and counter propagating pairs of beams along three perpendicular axes with correctly tuned polarizations are needed to work in conjunction with the 3D magnetic field. It should be further noted that the MOT can actually cool atoms below the Doppler limit, thanks to the hyperfine structure of the atoms, but the details are not important to the experiments so they are not discussed here [65].

2.5.2 Implementation

As discussed previously, the MOT requires a monotonically varying magnetic field in three dimensions, an atom that acts as a two level system with σ_+ and σ_- Zeeman transitions, and narrow linewidth continuous wave lasers to drive those transitions. In our case, a set of anti-Helmholtz coils provides the requisite magnetic field gradient, with each coil consisting of 114 turns of polyurethane-nylon coated copper wire wrapped around a water cooled aluminum frame. The frames are machined to snugly fit onto the vacuum chamber, creating a pair of anti-Helmholtz coils with a diameter of 18cm and coil separation of 10cm.

The magnetic field near the center of the anti-Helmholtz coils can be described by [66]

$$B_z(z,\rho) = \sum_{n=0} b_n B_z n \approx b_1 z + b_3(z^3 - 3z\rho^2/2), \tag{2.2}$$

$$B_\rho(z,\rho) = \sum_{n=0} b_n B_\rho n \approx -(b_1\rho)/2 + b_3(-3\rho z^2/2 + 3\rho^2 z/8), \tag{2.3}$$

where $b_1 = \frac{3\mu I A R^2}{(R^2+A^2)^{5/2}}$ and $b_3 = \frac{5(4A^2-3R^2)}{6(R^2+A^2)^2} b_1$. In our case A=10cm (the distance between coils) and R=9cm (radius of coils) thus $b_3 \ll b_1$. Therefore, the magnetic field varies approximately linearly in all directions near the center of coils at $\rho = z = 0$. Typical currents of 10A provide an on-axis magnetic field gradient of ~15Gauss/cm, while the radial magnetic field gradient is half of that at 7.5Gauss/cm.

To cancel the effect of Earth's magnetic field and to properly locate the

MOT in a good position (by redefining the zero magnetic field position) for ion extraction through electric field plates, 3 pairs of shim coils (featuring windings with the same helicity in pairs of coils wrapped around dedicated aluminum frames) are employed to create constant magnetic fields on three orthogonal axes. The three individual pairs of shim coils have dedicated current supplies to achieve independent magnetic field compensation in all three dimensions.

The $5s_{1/2}, F = 3$ and $5p_{3/2}, F = 4$ states of ^{85}Rb atoms are utilized to realize the approximate 2-level MOT trapping system discussed earlier, as $5s_{1/2}, F = 3$ is the only state to which $5p_{3/2}, F = 4$ can spontaneously decay. However, because $5p_{3/2}, F = 4$ is very close to the $5p_{3/2}, F = 3$ level (only 120MHz away, compared to ~30MHz natural linewidth of $5p_{3/2}$ states), the $5p_{3/2}, F = 3$ state can be populated as well during the continuous trap laser pumping. This state, in turn, can spontaneously decay to the $5s_{1/2}, F = 2$, which will not participate in the optical cycling associated with the trap, leading to atom loss from the trap. Thus, a second "repump" laser is required to transfer any atoms in the $5s_{1/2}, F = 2$ level back to $5p_{3/2}, F = 3$, where they are again trapped. Frequency locking for the trap and repump laser is based on saturated absorption spectroscopy, and has been discussed previously. The necessary red-detuning for cooling and trapping is achieved by red detuning a portion of the laser with AOM by 31MHz, then locking that portion to crossover peak in the absorption spectrum ~60MHz red detuned from $5s_{1/2}, F = 3$ to $5p_{3/2}, F = 4$ resonance peak for a net red detuning of ~30MHz from $5s_{1/2}, F = 3$ to $5p_{3/2}, F = 4$ resonance for the trap laser (compared to ~30MHz natural linewidth of $5p_{3/2}$ states). The value of the detuning is a

compromise between too little trapping force (too much red detuned) and too little trapping region (too little red detuned) and is a function of trap beam diameter and intensity (high intensity light dresses the trap states, causing additional blue (AC Stark) shifts of the transition frequency).

The frequency-locked trap laser beam is expanded by a telescope, consisting of AR-coated −100mm and +500mm lenses separated by 400mm, producing a ~5×11mm FWHM oval beam. That beam is then split into three orthogonal retroreflecting beams that cross at the center of the MOT vacuum chamber. Considering that the output of trap laser is 39mW, the power density of the trap laser is 30mW/cm^2, well beyond the saturation intensity of 3.895mW/cm^2 [67] for trap transition. Excess laser power means strong coupling between the two trap states, modifying the eigenstate energy as a function of laser power, pushing the system towards the regime of dipole trapping [68]. In a retroreflecting beam setup, standing waves are created, and in the regime of dipole trapping, atoms will be pushed towards local intensity maxima, creating an unwanted pattern in MOT for the experiments in this dissertation. To avoid this problem, the retroreflecting mirrors are mounted to a chassis which is suspended from optical table by rubber mounts. Minifans are installed next to the retroreflecting mirrors causing slight mirror vibrations, that (on time average) eliminate the standing wave patterns in the trap. Ultimately, this approach can reduce the stability of the MOT setup, and future work on eliminating the need for rubber suspension is highly recommended.

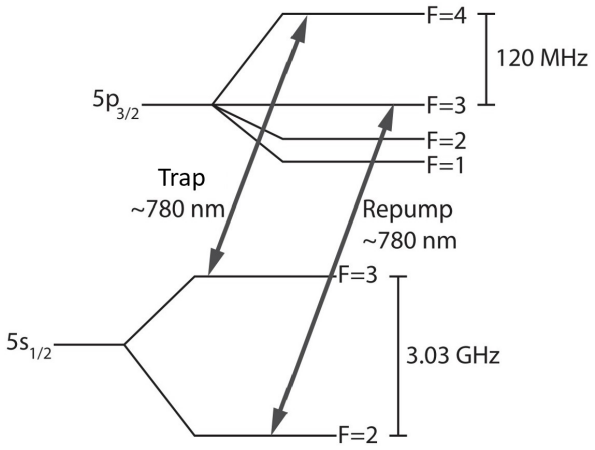

Figure 2.14: Energy diagram of the $5s_{1/2}$ and $5p_{3/2}$ states of ^{85}Rb [5].

2.5.3 MOT Maintenance

As discussed earlier, the position of the MOT is defined by the laser beams and the location of the zero in the magnetic field. Because the ion extraction hole in the electric field plate between the MOT and the detector is small, the requirement for accurate MOT positioning is high for our particular experimental setup. To achieve optimal MOT position, the following procedure is employed. First, an aperture is used to shrink the size of trap laser, better defining the propagating direction. Second, paper apertures are placed on the vacuum chamber windows through which the trap lasers propagate. The paper apertures are cut to the exact size of the vacuum chamber windows with a tiny hole cut in the center of the apertures. Third, the trap lasers are aligned to travel straight through the holes in the center of paper apertures. In this way, the beam positions, both incoming beam and reflected beam can be accurately defined to go straight through the center of vacuum chamber.

Beyond that, tiny adjustments to individual mirrors are still needed, as well as adjustments on shim coil current to position the magnetic field zero at the center of the vacuum chamber.

2.5.4 MOT Characterization

A few parameters of the MOT are very important for characterizing and controlling the interactions of the atoms it holds. As discussed in Chapter 1, the dipole-dipole interaction depends critically on interatomic distance, and setting the proper electric field is crucial for controlling resonant dipole-dipole interactions. Thus, MOT density, size and temperature, electric field inhomogeneity within the MOT, and the MOT electric field's relation to the applied voltage across electric field plates, are all crucial parameters.

A calibrated CCD camera (Ganz FC-06A) is used to measure the size and density of the MOT on a daily basis. Calibrating the size of MOT is straightforward, because the distance between the field plates is well defined at 1.00cm and both plates can be clearly imaged on the CCD. At the current camera position, the distance between the plates is 188 pixels(Lines), thus the size of the MOT can be determined by counting pixels(Lines) on CCD readout using a calibration factor of 53μm/pixel(Line).

The density of the MOT can be inferred from the fluorescence power emitted from the MOT. Given the high power density of the trapping laser, the MOT transition is well saturated. Accordingly, an atom within the MOT spends half of its time in the upper $5p$ state. Thus, on average, each atom emits a photon every two natural lifetimes, radiating a fluorescence power

per atom $P_{atom} = \frac{hc}{2\tau\lambda} = 4.7\text{pW}$. Averaged over all of the atoms and atom orientations in the MOT, the emitted radiation is isotropic, and the power captured by the CCD is determined by the solid angle it captures. In turn, that solid angle is determined by the camera aperture size (2.0cm diameter) and its distance from MOT (16cm), thus the optical power incident on the CCD can be related to the number of atoms within MOT (N) by $P_{CCD} = N \cdot P_{atom} \frac{\pi R^2_{aperture}}{4\pi d^2_{MOT-CCD}} = N \cdot 4.5 \times 10^{-15}\text{W}$.

So, the remaining factor needed to determine the number of atoms in the MOT is the relationship between the brightness of the MOT image (and the corresponding readout voltage) and the fluorescence power incident on the CCD. Unfortunately, the fluorescence from MOT is too weak to be accurately measured using our power meter. Thus, as an alternative, an attenuated 780nm laser beam is directed onto the CCD and the corresponding readout voltage is recorded. A known attenuation is then removed and the power of the brighter beam is measured directly by a calibrated power meter. With this, the relation between incident 780nm optical power and CCD brightness is determined. For the most recent calibration, the power in the less attenuated laser beam is measured to be 10.5μW, while the additional attenuation used for the CCD is found to reduce the transmission to only 0.6% of the incident power. This results in an incident power to the CCD of 62nW. Integrating the CCD readout voltage response associated with the laser beam over the beam profile then provided a calibration factor of $28.74\text{mV}\cdot\text{mm}^2/\text{nW}$. Combining the power calibration with the relationship between atom number and power received by CCD, the measured MOT image brightness on the CCD, and

the size of the MOT image, the number of atoms within the MOT can be measured. The MOT density can then be inferred by assuming a 3D Gaussian atom distribution with the measured FWHM.

The temperature of the MOT has been determined by temporarily shutting off the MOT trapping potential, switching off the trap and repump lasers using a combination of Pockels cells and polarizers, and measuring the expansion of the atoms as a function of time. A temperature measurement for our MOT, performed under conditions very similar to those used for the experiments described here, was performed by a former student, Kutteruf, as discussed in more detail in her dissertation [5]. At that time, the temperature of MOT was measured to be 70μK, and quite insensitive to the trapping and repump laser power, alignment, detuning, and Rb getter current.

The relation between the electric field in the MOT and the voltages applied to the electric field plates were calibrated by measuring Rydberg Stark shifts for different applied voltages. The energy difference between the $32p_{3/2}, m_j = 3/2$ and $32p_{3/2}, m_j = 1/2$ as a function of electric field can be accurately calculated using a program developed by Richards based on the method of Zimmerman et al. [69]. Experimentally, the same energy difference can be measured as a function of the voltage applied across the electric field generation plates. State-selective field ionization is used to measure the excitation probability in the two different levels as the frequency of the blue Rydberg excitation laser is scanned over the $5p_{3/2}$ to $32p_{3/2}$ resonance as a function of applied static voltage, and the frequency difference between the excitation maxima to the two states is determined. As mentioned previously, the blue

laser is frequency locked to a tunable F-P cavity, the resonance frequency of which is controlled by varying the voltage across a piezoelectric actuator which changes the length of the cavity, with the cavity resonance frequency varying at 361.7MHz/V.

The measured splitting vs. applied voltage to the MOT field plates is fit to the calculated field dependent splitting, to calibrate the relation between applied voltage and electric field in the MOT. The calibration is found to be $F = 0.92V_{plate}/\text{cm} - 0.09\text{V/cm}$ with V_{plate} being the voltage across electric field generation plates, and positive electric field defined as the direction from the MOT towards the MCP. Note that this calibration includes the effects of any stray fields, e.g., due to imperfect shielding of the HV connections to the MCP detector. The field offset(0.00V/cm), which indicates negligible field component parallel to the plane of the field plates, and residual (0.09V/cm) field perpendicular to the plane of the plates, demonstrates that the field plates provide a significant improvement on shielding compared to previous field rod designs, which had a 2.8V/cm offset and 1.5V/cm residual field. It should also be noted that the measured relation is perfectly consistent with finite element simulated value of $F = 0.92V_{plate}/\text{cm}$.

The field inhomogeneity within the MOT can be determined by measuring the voltage required to enable $32p_{3/2}, |m_j| = 3/2 + 32p_{3/2}, |m_j| = 3/2$ to $32s_{1/2} + 33s_{1/2}$ resonant energy transfer (discussed in more detail in chapters 3 and 4) when the blue laser is positioned to excite the Rydberg atoms at different positions within the MOT. Given that the Rydberg atom excitation region defined by blue laser beam (FWHM ~34μm) is much smaller than the

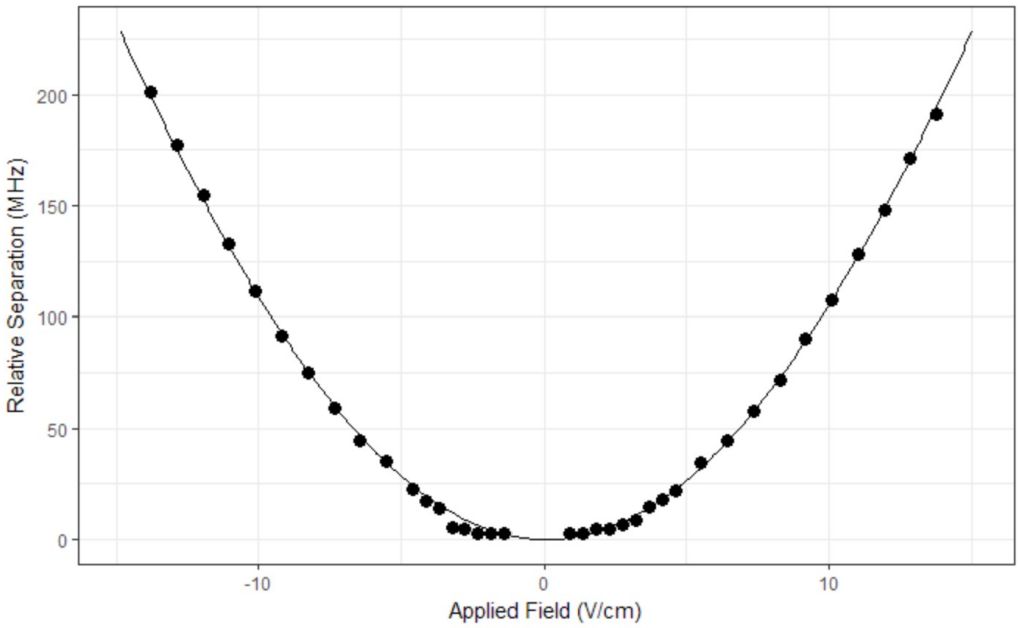

Figure 2.15: Frequency splitting between the $32p_{3/2}, m_j = 3/2$ and $32p_{3/2}, m_j = 1/2$ resonances as a function of applied electric field. The solid line is the calculated value while the dots are measured values using the best fit applied voltage to electric field calibration. Note that the excitation probability approaches zero with decreasing electric field, leading to increased uncertainties in the measured splitting.

diameter of the MOT (FWHM ~0.5mm), the local electric field at different locations within the MOT can be measured using slight adjustments of the position of the blue laser. After the resonance voltage at the center of the MOT is measured, the blue laser beam is moved from the center of the MOT (where the maximum number of Rydberg atoms are produced) towards the front, back, top, and bottom of the MOT (in sequence) until the Rydberg excitation drops to half of what was recorded at the center, suggesting the beam has been relocated to (roughly) the HWHM (0.25mm) of the atom distribution. The energy transfer resonance voltage is then measured at those four positions. The inhomogeneity of the electric field is then calibrated by comparing the resonance voltages for those five points. The resonance voltage is determined to be 12.466V/12.453V/12.480V/12.446V/12.480V at the center/front/back/top/bottom positions, respectively, indicating a field inhomogeneity of 0.05V/cm/mm horizontally and 0.06V/cm/mm vertically in a nominal resonant field of 11.40V/cm (0.44%/mm horizontally and 0.55%/mm vertically, compared to the FEA values of 0.75%/mm horizontally and 0.55%/mm vertically). While the electric field inhomogeneity along the direction of blue laser beam could not be measured, due to the symmetry of the field plates, variations in that dimension are expected to be small. Finite element analysis predicts a field inhomogeneity of 0.37%/mm in that dimension.

During experiment, the blue laser beam is first expanded to ~40mm diameter before being focused in the center of the MOT, using a 300mm lens to achieve a focusing size as small as 42.3μm vertically and 26.6μm horizontally FWHM (measured with Thorlabs BC106N-VIS beam profiler). Combining

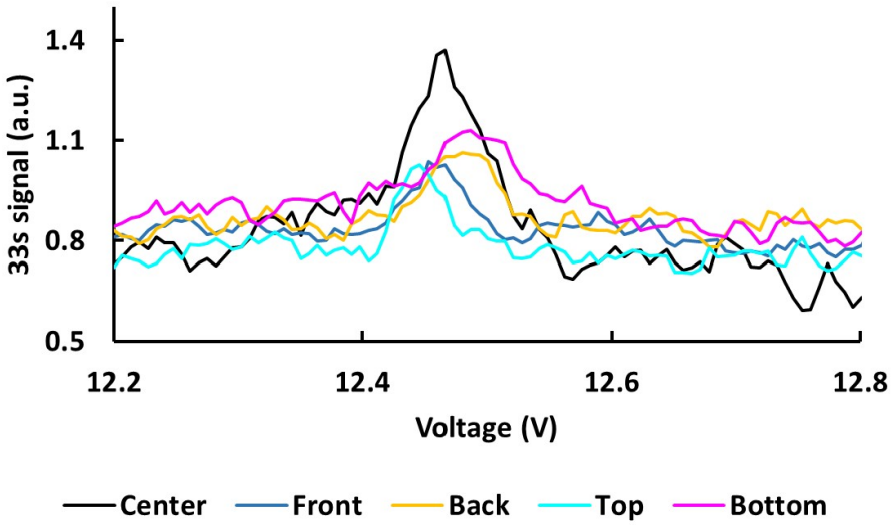

Figure 2.16: Probability of $32p_{3/2}, |m_j| = 3/2 + 32p_{3/2}, |m_j| = 3/2$ to $32s_{1/2} + 33s_{1/2}$ resonant energy transfer as a function of applied voltage at different Rydberg excitation positions within the MOT. The variation in resonance position is used to determine the field inhomogeneity in the MOT.

this with the field inhomogeneity measurement, the field inhomogeneity within the excited Rydberg atom volume is estimated to be 2.6mV/cm vertically and 1.3mV/cm horizontally. Compared to the relevant resonant dipole-dipole tuning electric field of ~11.5V/cm, the field inhomogeneity within excited Rydberg atom ensemble is ~0.03%. This is a significant improvement over past experimental geometries, and its effect on the experimental results is negligible compared to other measurement uncertainties and imperfections.

2.6 Data Collection

All of the experimental data were acquired using a LabView program originally written by White and then heavily modified by Zhou and Richards, all former

students. The program is capable of controlling the delay of a particular channel of the DG645 delay generator, sending event trigger pulses to the AWG510 Arbitrary Waveform Generator, reading the temperature and voltage on the F-P cavity, collecting waveforms from two oscilloscopes (monitoring Rydberg SSFI signal and MOT fluorescence), plus many more functions which are not used for the experiments described in this dissertation. The waveforms from the oscilloscopes can also be gated and integrated in the program for ease of data analysis afterwards. Full Rydberg TOF traces are also saved to accommodate more customized data analysis after completion of the experiments.

Chapter 3

Modeling a Dipole-dipole Coupled Rydberg Atom Gas

A Rydberg atom gas subject to dipole-dipole interactions can be extremely complex. An ensemble of N initial $32p_{3/2}, |m_j| = 3/2$ (referred simply as p in chapters 3-5 unless m_j is specified) atoms pairs subject to resonant pp to $32s33s$ ($32s$ referred simply as s, $33s$ referred as s' in chapters 3-5) dipole-dipole interactions, can evolve into a coherent superposition of $O(N!)$ quantum states (hence the tremendous capabilities of quantum computer/simulator), requiring an $O(N!) \times O(N!)$ Hamiltonian to describe. The experiments discussed in this dissertation involve ~5000 Rydberg atoms, rendering complete simulations - including all states and interactions within Rydberg atom gas ensemble - impossible with current computing technologies.

Fortunately, approximations can be made to simulate a fully interacting

Rydberg gas with reasonable accuracy. Since the dipole-dipole interaction strength for a pair of Rydberg atoms scales as R^{-3} (where R is the interatomic distance), the coupling between nearest neighboring Rydberg atoms can inhibit interactions involving beyond nearest neighbors [70, 71]. Specifically, a strong resonant dipole-dipole coupling between nearest neighbors shifts the eigenenergies of the atom pair, by $\pm V_{nearest}$, so the dipole-dipole coupling between either atom in the pair and its more distant neighbors is non-resonant, with an effective detuning of $\pm V_{nearest}$. Accordingly, the coupling to the more distant atoms takes the form of a second order van der Waals interaction with an associated energy shift on the order of $\left|\frac{V_R^2}{V_{nearest}}\right|$, where V_R is the dipole-dipole interaction strength between an atom in the initial pair and another atom at a distance R away, which scales as R^{-3}. In a ensemble of uniform density, the probability of finding an atom R away from the central atom scales as $4\pi R^2$, thus the average energy shift of the Rydberg electron on either of the central atoms, by the atoms in the ensemble at a larger distance R away, scales as $4\pi R^2\left|\frac{V_R^2}{V_{nearest}}\right| \propto R^2\left|\frac{R^{-6}}{V_{nearest}}\right| \propto R^{-4}$. Therefore, the total energy shift on a central Rydberg atom, due to distant atoms, scales as $\int_R^\infty R^{-4}dR \propto R^{-3}$. Thus, the effects of far away atoms on the central atoms can be reasonably neglected. Hence, the behavior of the Rydberg atom gas can be approximated with reasonable accuracy by only considering interactions between an atom and a few of its closest neighbors. The simplest approximation only includes interactions between nearest neighbors. To improve on this simplest model, this chapter also describes an approach that breaks up the ensemble into groups of four, rather than two, fully interacting atoms. Both simulation strategies

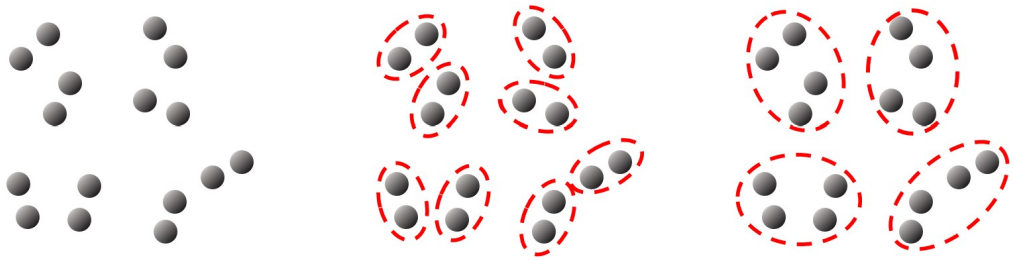

Figure 3.1: Rydberg gas ensemble, broken into groups of two atoms or four atoms.

will be discussed in this chapter and various results of the two models will be compared. This dissertation does not include models that include larger groups of atoms, due to limited computation capabilities. Previous studies of dipole-dipole *resonant* energy transfer processes have shown that the results of simulations based on ensembles of more than four atoms closely match those calculations involving only four atoms [30]. However, as discussed in chapter 5, this is not the case for off resonant energy transfer processes.

3.1 Tuning the Resonance of Dipole-dipole Interaction

To facilitate resonant energy transfer between a pair of atoms, the energy of pp and ss' or $s's$ (for simplicity we refer to both ss' and $s's$ as ss' in the following chapters when referencing only their energy rather than quantum states) must be closely matched. In experiments, the energy detuning between ss' and pp can be varied by exploiting the different Stark shifts of the p, s and s' single atom states as a function of applied electric field. A plot of the Rb

energy levels as a function of external electric field (i.e., a "Stark map") can be calculated numerically. We have used a code developed by Richards based of the method of Zimmerman et al. [69]. Comparing the total energy of a pair of isolated p atoms with the total energy of an $s + s'$ atom pair, one obtains the Stark map for pp and ss' (see Figures 3.2 and 3.3). It is important to note that the dipole field due to one atom at the location of the other is generally not parallel to the externally applied electric field, so the projection of total electronic orbital angular momentum along the external electric field axis is not conserved, and ss' pairs, with total angular momentum projection on the external field axis $|m_J| = 0, 1$, can evolve into states with $|m'_J| = 0, 1, 2$ such as $pp(m_j = +3/2, m_j = +1/2)$, $pp(m_j = -1/2, m_j = -1/2)$ etc. The impact of those additional configurations of those states on resonant energy transfer will be discussed later. As shown in Figures 3.2 and 3.3, the bare pp and ss' energy curves intersect at 11.49V/cm, identifying a resonance electric field of 11.49V/cm for the $pp + ss'$ interaction. Because the Stark shift of the pp and ss' states is linear very near resonance (over a field range of ± 0.5V/cm for the scope of this dissertation), the energy separation between ss' and pp (which gives the detuning from the resonance condition), can be approximated as $\delta(F) = 170 * (F - F_{res})\text{MHz} \cdot \text{V}^{-1} \cdot \text{cm}$, where F is the externally applied electric field strength, and F_{res} is the resonance electric field for the $pp + ss'$ interaction. Accordingly, the energy splitting between the pp and ss' states can be tuned, varying linearly with the external electric field.

In the experiments, voltages applied across the two electric field plates provide the appropriate time-dependent tuning electric fields. We find that when

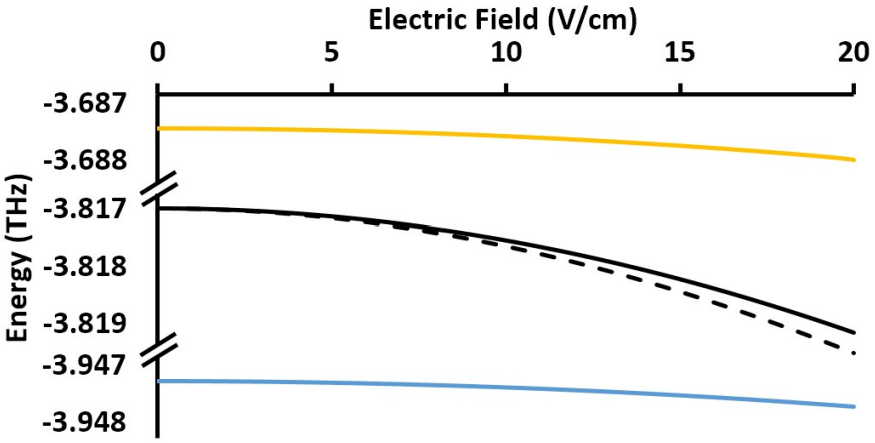

Figure 3.2: Stark map of $32p_{3/2}, |m_j| = 3/2$ (denoted p - black solid), $32p_{3/2}, |m_j| = 1/2$ (black dash), $32s$(denoted s - blue) and $33s$(denoted s' - yellow) single atom states in ^{85}Rb, relative to the ionization potential.

the back field plate (furthest from the MCP detector) is held at 12.93V, the atoms are tuned to resonance when the front plate (nearest to the MCP detector) is grounded. According to the field calibration, the measured resonance field is 11.83V/cm, slightly different from the predicted value of 11.49V/cm. The front field plate is connected to the output of an arbitrary waveform generator (AWG) enabling fast (2ns) changes in the applied electric field of $\sim\pm$0.5V/cm about the resonance, to facilitate fast detuning changes.

3.2 Interacting Pair of Rydberg Atoms Subject to Electric Field

Consider a pair of Rydberg atoms, each containing one nucleus (or ion core for non-hydrogenic Rydberg atoms) and one electron. For atom separations

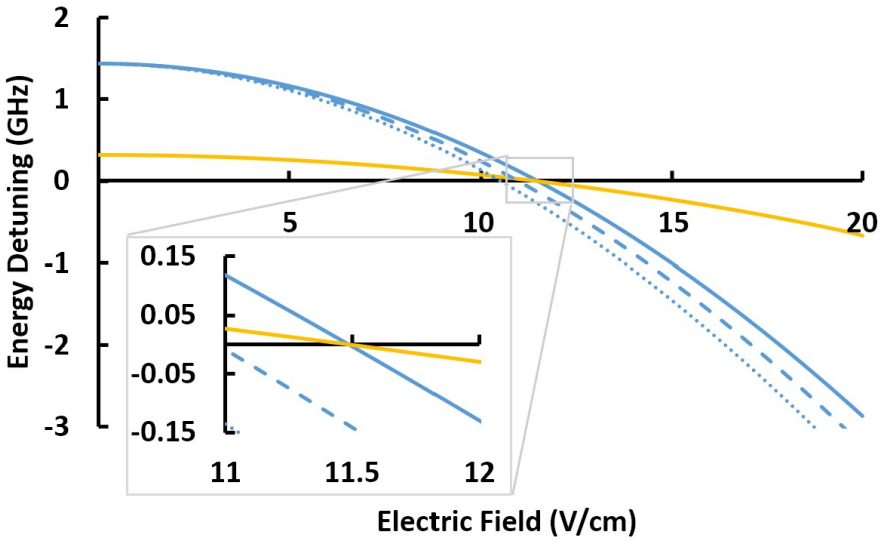

Figure 3.3: Stark map of $pp(|m_j| = 3/2, |m_j| = 3/2)$(blue solid), $pp(|m_j| = 3/2, |m_j| = 1/2)$(blue dash), $pp(|m_j| = 1/2, |m_j| = 1/2)$ (blue dot) and ss' (yellow) non-interacting pair energies, relative to the $pp(|m_j| = 3/2, |m_j| = 3/2)$ to ss' energy transfer resonance which occurs in an electric field of ~11.5 V/cm.

much greater than the spatial extent of the relevant electronic states of either atom, the lowest order term in the neutral atom-atom multipole coupling is dipole-dipole. The dipole-dipole interaction between two atoms is [27]

$$V_{DD} = \frac{\overrightarrow{\boldsymbol{r_1}} \cdot \overrightarrow{\boldsymbol{r_2}}}{R^3} - \frac{3(\overrightarrow{\boldsymbol{r_1}} \cdot \overrightarrow{\boldsymbol{R}})(\overrightarrow{\boldsymbol{r_2}} \cdot \overrightarrow{\boldsymbol{R}})}{R^5}, \tag{3.1}$$

where $\overrightarrow{\boldsymbol{r_1}}, \overrightarrow{\boldsymbol{r_2}}$ are the positions of electrons 1 and 2 relative to the ion core of atoms 1 and 2, respectively, and $\overrightarrow{\boldsymbol{R}}$ is the position of ion core 2 relative to 1. We define $\hat{\boldsymbol{z}}$ as the direction of the external field, and expand this equation with $\overrightarrow{\boldsymbol{r_1}} = (x_1, y_1, z_1), \overrightarrow{\boldsymbol{r_2}} = (x_2, y_2, z_2)$ and $\overrightarrow{\boldsymbol{R}} = (x_3, y_3, z_3)$. The interatomic distance is $\left|\overrightarrow{\boldsymbol{R}}\right| = \sqrt{x_3^2 + y_3^2 + z_3^2}$ while the direction of interatomic vector can be defined using $\theta = \arctan\frac{\sqrt{x_3^2+y_3^2}}{z_3}$ and $\phi = \arctan\frac{y_3}{x_3}$. Here, θ is the angle between the internuclear and $\hat{\boldsymbol{z}}$ axes. For two atoms, our results must be independent of the azimuthal angle ϕ (representing rotations about the internuclear axis), but this will not be the case for ensembles with more than two atoms). We now have

$$\begin{aligned} V_{DD} = \frac{1}{R^3}\big[&(x_1x_2 + y_1y_2 + z_1z_2) - 3(x_1\sin\theta\cos\phi + y_1\sin\theta\sin\phi + z_1\cos\theta) \\ &\cdot (x_2\sin\theta\cos\phi + y_2\sin\theta\sin\phi + z_2\cos\theta)\big]. \end{aligned} \tag{3.2}$$

Due to the substantial mass of the ions, and their relatively large separation, $\overrightarrow{\boldsymbol{R}}$ is treated as a classical parameter. However, the positions of the electrons, $x_1, y_1, z_1, x_2, y_2, z_2$ are described by quantum mechanical operators that need to be integrated over the distributions of the relevant atomic orbitals.

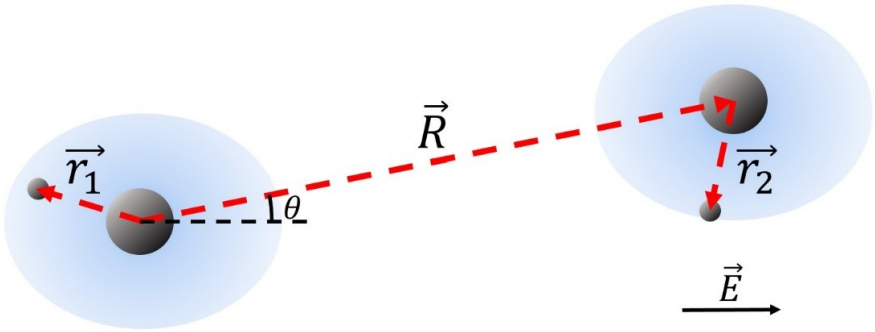

Figure 3.4: Dipole-dipole interaction between a pair of Rydberg atoms subject to an electric field, $\vec{\boldsymbol{E}} = E\hat{\boldsymbol{z}}$.

To exploit the symmetry of the atomic orbitals, and thus ease the computation, the $\hat{x}, \hat{y}, \hat{z}$ operators can be written in terms of spherical tensor operators [72, 73], where $\hat{x} = \frac{\hat{r}}{\sqrt{2}}\left(C_{-1}^{(1)} - C_1^{(1)}\right), \hat{y} = \frac{i\hat{r}}{\sqrt{2}}\left(C_{-1}^{(1)} + C_1^{(1)}\right), \hat{z} = \hat{r}C_0^{(1)}$, and $\hat{r}$ is the radial operator. Therefore

$$
\begin{aligned}
V_{DD} = \frac{\hat{r}\hat{r}}{R^3}\Bigg[& C_1^{(1)}C_1^{(1)}\left(-\frac{3}{2}\sin^2\theta(\cos 2\phi - i\sin 2\phi)\right) \\
& + \frac{3}{2\sqrt{2}}\left(C_1^{(1)}C_0^{(1)} + C_0^{(1)}C_1^{(1)}\right)\sin 2\theta(\cos\phi - i\sin\phi) \\
& + C_0^{(1)}C_0^{(1)}(1 - 3\cos^2\theta) \\
& + \left(C_1^{(1)}C_{-1}^{(1)} + C_{-1}^{(1)}C_1^{(1)}\right)\left(\frac{3}{2}\sin^2\theta - 1\right) \\
& + \frac{3}{2\sqrt{2}}\left(C_{-1}^{(1)}C_0^{(1)} + C_0^{(1)}C_{-1}^{(1)}\right)\sin 2\theta(-\cos\phi - i\sin\phi) \\
& + C_{-1}^{(1)}C_{-1}^{(1)}\left(-\frac{3}{2}\sin^2\theta(\cos 2\phi + i\sin 2\phi)\right)\Bigg],
\end{aligned}
\tag{3.3}
$$

where, in each product of two operators, the first operator always acts on the

first atom and the second operator always acts on the second atom. Notably, the projection of total electronic angular momentum along the $\hat{\boldsymbol{z}}$ axis, m_J, is not conserved in the presence of both the static field and V_{DD}. V_{DD} couples states in which m_J changes by 0, ± 1, or ± 2.

Finally, we must include all the energetically accessible quantum states that may be relevant to the dynamics over the $\sim 1\mu$s time scales of interest. In a resonant or near resonant field, a pair of $pp(|m_j| = 3/2, |m_j| = 3/2)$ atoms can evolve into $ss'(|m_j| = 1/2, |m_j| = 1/2)$. However, in principle, ss' can then evolve into $pp(|m_j| = 1/2, |m_j| = 1/2)$, or $pp(|m_j| = 3/2, |m_j| = 1/2)$, etc. From there the pair can continue to evolve into other pp, ss' states with different m_j values, resulting in a total of 24 interacting states.

Fortunately, for a given electric field, some states are only weakly coupled to the others, due to their large energy detuning and, therefore can be eliminated from consideration over $\sim 1\mu$s evolutionary timescales. The energy difference between the $p(|m_j| = 3/2)$ and $p(|m_j| = 1/2)$ states, in an electric field near the pp to ss' resonance, is ~140MHz (see Figure 3.2), while the average dipole-dipole interaction strength under the experimental conditions in this dissertation (Rydberg atom densities of $\leq 3 \times 10^9/\text{cm}^3$) is $\leq$10MHz. Therefore, coupling to atom pairs $pp(|m_j| = 3/2, |m_j| = 1/2)$ or $pp(|m_j| = 1/2, |m_j| = 1/2)$ can be neglected for pairs of atoms initially excited to $pp(|m_j| = 3/2, |m_j| = 3/2)$. Accordingly, for pairs of atoms starting from $pp(m_j = +3/2, m_j = +3/2)$, only three states, $pp(m_j = +3/2, m_j = +3/2)$, $ss'(m_j = +1/2, m_j = +1/2)$ and $s's(m_j = +1/2, m_j = +1/2)$, need to be considered to accurately simulate the system dynamics of a single atom

pair. The states that need to be considered for pairs of atoms starting from $pp(m_j = -3/2, m_j = -3/2)$ or $pp(m_j = \pm 3/2, m_j = \mp 3/2)$ are similarly limited. To simplify notation, m_j=+3/2(in case of p) or +1/2(in case of s or s') will simply be written as +, while m_j=−3/2 or −1/2 will be denoted as −.

Within the restricted basis approximation, the system separates in to four independent three level problems, for the four possible m_j combinations in the initial state: $pp(++)$ evolving into $ss'(++) + s's(++)$, $pp(--)$ evolving into $ss'(--) + s's(--)$, and $pp(+-)/(-+)$ evolving into $ss'(+-)/(-+) + s's(+-)/(-+)$.

There are three corresponding interaction matrix elements:

$$\langle pp(++)|V_{DD}|ss'(++)\rangle = \frac{\langle p|\hat{r}|s\rangle \langle p|\hat{r}|s'\rangle}{3R^3}\left(-\frac{3}{2}\sin^2\theta(\cos 2\phi - i\sin 2\phi)\right) \quad (3.4)$$

(denoted V_{RT1}),

$$\langle pp(--)|V_{DD}|ss'(--)\rangle = \frac{\langle p|\hat{r}|s\rangle \langle p|\hat{r}|s'\rangle}{3R^3}\left(-\frac{3}{2}\sin^2\theta(\cos 2\phi + i\sin 2\phi)\right) \quad (3.5)$$

(denoted V^*_{RT1}),

$$\langle pp(\pm\mp)|V_{DD}|ss'(\pm\mp)\rangle = \frac{\langle p|\hat{r}|s\rangle \langle p|\hat{r}|s'\rangle}{3R^3}\left(-1 + \frac{3}{2}\sin^2\theta\right) \quad (3.6)$$

(denoted V_{RT0}).

Using a radial matrix element calculator developed by Richards [74], we find $\langle p|\hat{r}|s\rangle$=964 and $\langle p|\hat{r}|s'\rangle$=941, respectively. With an energy detuning E be-

tween pp and ss', the four relevant Hamiltonians are:

$$H_{\text{2atom,1}} = \begin{pmatrix} 0 & V_{RT1} & V_{RT1} \\ V_{RT1}^* & E & 0 \\ V_{RT1}^* & 0 & E \end{pmatrix}, \tag{3.7}$$

where the basis states are $pp(++)$, $ss'(++)$ and $s's(++)$,

$$H_{\text{2atom,-1}} = \begin{pmatrix} 0 & V_{RT1}^* & V_{RT1}^* \\ V_{RT1} & E & 0 \\ V_{RT1} & 0 & E \end{pmatrix}, \tag{3.8}$$

where the basis states are $pp(--)$, $ss'(--)$ and $s's(--)$, and

$$H_{\text{2atom,0}} = \begin{pmatrix} 0 & V_{RT0} & V_{RT0} \\ V_{RT0} & E & 0 \\ V_{RT0} & 0 & E \end{pmatrix}, \tag{3.9}$$

where the basis states are $pp(\pm\mp)$, $ss'(\pm\mp)$ and $s's(\pm\mp)$. The subscripts $+1$, -1, and 0 label the sign of the projection of total electronic angular momentum on the $\hat{\boldsymbol{z}}$ axis. The angle-dependent on-resonance energies of the four pair eigenstates, in the reduced basis, are shown in Figure 3.5. Results of diagonalization of the full 24 state Hamiltonian are shown in Figure 3.5. The good agreement between the full and reduced basis calculations shows that the latter is a reasonable approximation to the full problem.

In simulations where only the total population in p, s, and s' is of interest,

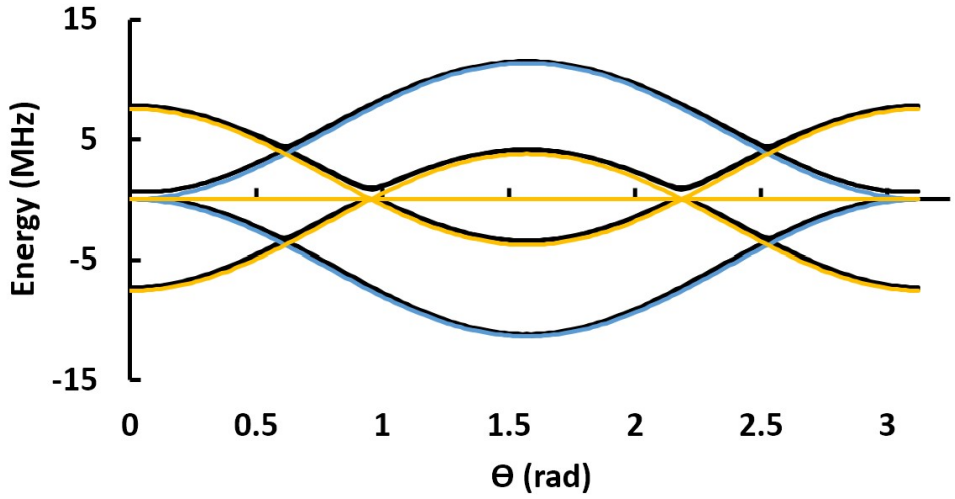

Figure 3.5: On resonance eigenenergy of $H_{2\text{atom},1}$ (blue), $H_{2\text{atom},0}$ (yellow) and Hamiltonian considering all possible m_j values of pp, ss' (black) as a function of θ at average atom separation at $3\times10^9/\text{cm}^3$ Rydberg atom density. Note the eigenenergies of the simplified Hamiltonians $H_{2\text{atom},1}$ and $H_{2\text{atom},0}$ only differ slightly from the full Hamiltonian, suggesting the simplification is reasonable, especially for short evolution times.

the systems described by $H_{2\text{atom},1}$ and $H_{2\text{atom},\text{-}1}$ behave identically, as their only difference is the direction of phase evolution. In addition, the $+-$ and $-+$ configurations described by $H_{2\text{atom},0}$ evolve identically. Thus, in simulations, the random m_j signs of the initial p states is taken into account by allocating 50% probability each to $H_{2\text{atom},1}$ and $H_{2\text{atom},0}$ when simulating the evolution of pairs of atoms in an ensemble. These simulations typically involve the evolution of ~10,000 independent pairs of atoms at random interatomic distances and orientations of the internuclear axis relative to $\hat{\boldsymbol{z}}$ (as discussed in more detail later).

The total population in p states normalized to the total Rydberg population can be retrieved at anytime during the simulation by computing the squared norm of the amplitude in first basis state, with the rest of the population split evenly between s and s'.

3.3 Ensemble of Four Rydberg Atoms Subject to an Electric Field

Beyond resonant energy transfer process, dipole-dipole interactions can also facilitate exchange or "excitation hopping" in a Rydberg atom gas, through ps to sp and ps' to $s'p$ couplings. [5, 30, 31, 33, 70, 71, 75, 76, 77, 78, 79, 80, 81, 82, 83, 84, 85, 86, 87] To evaluate the effect of excitation hopping on an ensemble initially excited to pp, one must consider more than two atoms and beyond nearest neighbor interactions. Thus, we also consider ensembles of four atoms to evaluate the effects of hopping.

To simulate hopping, additional dipole-dipole interactions need to be considered:

$$\langle ps(\pm\pm)|V_{DD}|sp(\pm\pm)\rangle = -\frac{\langle p|\hat{r}|s\rangle\,\langle s|\hat{r}|p\rangle}{3R^3}\left(-1+\frac{3}{2}\sin^2\theta\right) \tag{3.10}$$

(denoted V_{sp0}),

$$\langle ps'(\pm\pm)|V_{DD}|s'p(\pm\pm)\rangle = -\frac{\langle p|\hat{r}|s'\rangle\,\langle s'|\hat{r}|p\rangle}{3R^3}\left(-1+\frac{3}{2}\sin^2\theta\right) \tag{3.11}$$

(denoted $V_{s'p0}$),

$$\langle ps(+-)|V_{DD}|sp(+-)\rangle = \frac{\langle p|\hat{r}|s\rangle\,\langle s|\hat{r}|p\rangle}{3R^3}\left(\frac{3}{2}\sin^2\theta(\cos2\phi - i\sin2\phi)\right) \tag{3.12}$$

(denoted V_{sp1}),

$$\langle ps'(+-)|V_{DD}|s'p(+-)\rangle = \frac{\langle p|\hat{r}|s'\rangle\,\langle s'|\hat{r}|p\rangle}{3R^3}\left(\frac{3}{2}\sin^2\theta(\cos2\phi - i\sin2\phi)\right) \tag{3.13}$$

(denoted $V_{s'p1}$),

$$\langle ps(-+)|V_{DD}|sp(-+)\rangle = \frac{\langle p|\hat{r}|s\rangle\,\langle s|\hat{r}|p\rangle}{3R^3}\left(\frac{3}{2}\sin^2\theta(\cos2\phi + i\sin2\phi)\right) \tag{3.14}$$

(denoted V^*_{sp1}),

$$\langle ps'(-+)|V_{DD}|s'p(-+)\rangle = \frac{\langle p|\hat{r}|s'\rangle\,\langle s'|\hat{r}|p\rangle}{3R^3}\left(\frac{3}{2}\sin^2\theta(\cos2\phi + i\sin2\phi)\right) \tag{3.15}$$

(denoted $V^*_{s'p1}$).

Three Hamiltonians are needed to describe the scenarios corresponding to different combinations of signs of m_j for the respective atoms in the initial state.

$$H_{4\text{atom},2} = \begin{pmatrix}
0 & V_{RT1} & V_{RT1} & V_{RT1} & V_{RT1} & V_{RT1} & V_{RT1} & V_{RT1} & V_{RT1} & V_{RT1} & V_{RT1} & V_{RT1} & V_{RT1} & 0 & 0 & 0 & 0 & 0 & 0 \\
V^*_{RT1} & E & 0 & V_{s'p0} & 0 & V_{s'p0} & 0 & 0 & V_{sp0} & 0 & V_{sp0} & 0 & 0 & 0 & V_{RT1} & V_{RT1} & 0 & 0 & 0 \\
V^*_{RT1} & 0 & E & 0 & V_{sp0} & 0 & V_{sp0} & V_{s'p0} & 0 & V_{s'p0} & 0 & 0 & 0 & 0 & 0 & 0 & V_{RT1} & V_{RT1} & 0 \\
V^*_{RT1} & V_{s'p0} & 0 & E & 0 & V_{s'p0} & 0 & V_{sp0} & 0 & 0 & 0 & 0 & V_{sp0} & V_{RT1} & 0 & V_{RT1} & 0 & 0 & 0 \\
V^*_{RT1} & 0 & V_{sp0} & 0 & E & 0 & V_{sp0} & 0 & V_{s'p0} & 0 & 0 & V_{s'p0} & 0 & 0 & 0 & 0 & V_{RT1} & 0 & V_{RT1} \\
V^*_{RT1} & V_{s'p0} & 0 & V_{s'p0} & 0 & E & 0 & 0 & 0 & V_{sp0} & 0 & V_{sp0} & 0 & V_{RT1} & V_{RT1} & 0 & 0 & 0 & 0 \\
V^*_{RT1} & 0 & V_{sp0} & 0 & V_{sp0} & 0 & E & 0 & 0 & 0 & V_{s'p0} & 0 & V_{s'p0} & 0 & 0 & 0 & 0 & V_{RT1} & V_{RT1} \\
V^*_{RT1} & 0 & V_{s'p0} & V_{sp0} & 0 & 0 & 0 & E & 0 & V_{s'p0} & 0 & 0 & V_{sp0} & V_{RT1} & 0 & 0 & 0 & V_{RT1} & 0 \\
V^*_{RT1} & V_{sp0} & 0 & 0 & V_{s'p0} & 0 & 0 & 0 & E & 0 & V_{sp0} & V_{s'p0} & 0 & 0 & V_{RT1} & 0 & 0 & 0 & V_{RT1} \\
V^*_{RT1} & 0 & V_{s'p0} & 0 & 0 & V_{sp0} & 0 & V_{s'p0} & 0 & E & 0 & V_{sp0} & 0 & V_{RT1} & 0 & 0 & V_{RT1} & 0 & 0 \\
V^*_{RT1} & V_{sp0} & 0 & 0 & 0 & 0 & V_{s'p0} & 0 & V_{sp0} & 0 & E & 0 & V_{s'p0} & 0 & 0 & V_{RT1} & 0 & 0 & V_{RT1} \\
V^*_{RT1} & 0 & 0 & 0 & V_{s'p0} & V_{sp0} & 0 & 0 & V_{s'p0} & V_{sp0} & 0 & E & 0 & 0 & V_{RT1} & 0 & V_{RT1} & 0 & 0 \\
V^*_{RT1} & 0 & 0 & V_{sp0} & 0 & 0 & V_{s'p0} & V_{sp0} & 0 & 0 & V_{s'p0} & 0 & E & 0 & 0 & V_{RT1} & 0 & V_{RT1} & 0 \\
0 & 0 & 0 & V^*_{RT1} & 0 & V^*_{RT1} & 0 & V^*_{RT1} & 0 & V^*_{RT1} & 0 & 0 & 0 & 2E & 0 & 0 & 0 & 0 & 0 \\
0 & V^*_{RT1} & 0 & 0 & 0 & V^*_{RT1} & 0 & 0 & V^*_{RT1} & 0 & 0 & V^*_{RT1} & 0 & 0 & 2E & 0 & 0 & 0 & 0 \\
0 & V^*_{RT1} & 0 & V^*_{RT1} & 0 & 0 & 0 & 0 & 0 & 0 & V^*_{RT1} & 0 & V^*_{RT1} & 0 & 0 & 2E & 0 & 0 & 0 \\
0 & 0 & V^*_{RT1} & 0 & V^*_{RT1} & 0 & 0 & 0 & 0 & V^*_{RT1} & 0 & V^*_{RT1} & 0 & 0 & 0 & 0 & 2E & 0 & 0 \\
0 & 0 & V^*_{RT1} & 0 & 0 & 0 & V^*_{RT1} & V^*_{RT1} & 0 & 0 & 0 & 0 & V^*_{RT1} & 0 & 0 & 0 & 0 & 2E & 0 \\
0 & 0 & 0 & 0 & V^*_{RT1} & 0 & V^*_{RT1} & 0 & V^*_{RT1} & 0 & V^*_{RT1} & 0 & 0 & 0 & 0 & 0 & 0 & 0 & 2E
\end{pmatrix} \tag{3.16}$$

simulates the scenario where all p atoms start from the same m_j state ($pppp(++++)$ or $pppp(----)$). The Hamiltonian for $pppp(++++)$ is shown here, and the corresponding basis states (with states of m_j always being $++++$) are $pppp$, $ss'pp$, $s'spp$, $sps'p$, $s'psp$, $spps'$, $s'pps$, $pss'p$, $ps'sp$, $psps'$, $ps'ps$, $ppss'$, $pps's$, $sss's'$, $ss'ss'$, $ss's's$, $s'sss'$, $s'ss's$, $s's'ss$. All the interaction strengths V are functions of the internuclear vector between the two atoms involved, $\overrightarrow{\boldsymbol{R_{ab}}} = (R_{ab}, \theta_{ab}, \phi_{ab})$.

$$H_{4\text{atom},1} = \begin{pmatrix}
0 & V_{RT0} & V_{RT0} & V_{RT0} & V_{RT0} & V_{RT0} & V_{RT0} & V_{RT1} & V_{RT1} & V_{RT1} & V_{RT1} & V_{RT1} & V_{RT1} & 0 & 0 & 0 & 0 & 0 & 0 \\
V_{RT0} & E & 0 & V_{s'p0} & 0 & V_{s'p0} & 0 & 0 & V_{sp1} & 0 & V_{sp1} & 0 & 0 & 0 & V_{RT1} & V_{RT1} & 0 & 0 & 0 \\
V_{RT0} & 0 & E & 0 & V_{sp0} & 0 & V_{sp0} & V_{s'p1} & 0 & V_{s'p1} & 0 & 0 & 0 & 0 & 0 & 0 & V_{RT1} & V_{RT1} & 0 \\
V_{RT0} & V_{s'p0} & 0 & E & 0 & V_{s'p0} & 0 & V_{sp1} & 0 & 0 & 0 & 0 & V_{sp1} & V_{RT1} & 0 & V_{RT1} & 0 & 0 & 0 \\
V_{RT0} & 0 & V_{sp0} & 0 & E & 0 & V_{sp0} & 0 & V_{s'p1} & 0 & 0 & V_{s'p1} & 0 & 0 & 0 & 0 & V_{RT1} & 0 & V_{RT1} \\
V_{RT0} & V_{s'p0} & 0 & V_{s'p0} & 0 & E & 0 & 0 & 0 & V_{sp1} & 0 & V_{sp1} & 0 & V_{RT1} & V_{RT1} & 0 & 0 & 0 & 0 \\
V_{RT0} & 0 & V_{sp0} & 0 & V_{sp0} & 0 & E & 0 & 0 & 0 & V_{s'p1} & 0 & V_{s'p1} & 0 & 0 & 0 & 0 & V_{RT1} & V_{RT1} \\
V^*_{RT1} & 0 & V^*_{s'p1} & V^*_{sp1} & 0 & 0 & 0 & E & 0 & V_{s'p0} & 0 & 0 & V_{sp0} & V_{RT0} & 0 & 0 & 0 & V_{RT0} & 0 \\
V^*_{RT1} & V^*_{sp1} & 0 & 0 & V^*_{s'p1} & 0 & 0 & 0 & E & 0 & V_{sp0} & V_{s'p0} & 0 & 0 & V_{RT0} & 0 & 0 & 0 & V_{RT0} \\
V^*_{RT1} & 0 & V^*_{s'p1} & 0 & 0 & V^*_{sp1} & 0 & V_{s'p0} & 0 & E & 0 & V_{sp0} & 0 & V_{RT0} & 0 & 0 & V_{RT0} & 0 & 0 \\
V^*_{RT1} & V^*_{sp1} & 0 & 0 & 0 & 0 & V^*_{s'p1} & 0 & V_{sp0} & 0 & E & 0 & V_{s'p0} & 0 & 0 & V_{RT0} & 0 & 0 & V_{RT0} \\
V^*_{RT1} & 0 & 0 & 0 & V^*_{s'p1} & V^*_{sp1} & 0 & 0 & V_{s'p0} & V_{sp0} & 0 & E & 0 & 0 & V_{RT0} & 0 & V_{RT0} & 0 & 0 \\
V^*_{RT1} & 0 & 0 & V^*_{sp1} & 0 & 0 & V^*_{s'p1} & V_{sp0} & 0 & 0 & V_{s'p0} & 0 & E & 0 & 0 & V_{RT0} & 0 & V_{RT0} & 0 \\
0 & 0 & 0 & V^*_{RT1} & 0 & V^*_{RT1} & 0 & V_{RT0} & 0 & V_{RT0} & 0 & 0 & 0 & 2E & 0 & 0 & 0 & 0 & 0 \\
0 & V^*_{RT1} & 0 & 0 & 0 & V^*_{RT1} & 0 & 0 & V_{RT0} & 0 & 0 & V_{RT0} & 0 & 0 & 2E & 0 & 0 & 0 & 0 \\
0 & V^*_{RT1} & 0 & V^*_{RT1} & 0 & 0 & 0 & 0 & 0 & 0 & V_{RT0} & 0 & V_{RT0} & 0 & 0 & 2E & 0 & 0 & 0 \\
0 & 0 & V^*_{RT1} & 0 & V^*_{RT1} & 0 & 0 & 0 & 0 & V_{RT0} & 0 & V_{RT0} & 0 & 0 & 0 & 0 & 2E & 0 & 0 \\
0 & 0 & V^*_{RT1} & 0 & 0 & 0 & V^*_{RT1} & V_{RT0} & 0 & 0 & 0 & 0 & V_{RT0} & 0 & 0 & 0 & 0 & 2E & 0 \\
0 & 0 & 0 & 0 & V^*_{RT1} & 0 & V^*_{RT1} & 0 & V_{RT0} & 0 & V_{RT0} & 0 & 0 & 0 & 0 & 0 & 0 & 0 & 2E
\end{pmatrix} \tag{3.17}$$

simulates the scenario where one p atom starts from a state with a different sign of m_j than the rest. The Hamiltonian for $pppp(-+++)$ is shown here, and the basis states remain the same as for the previous Hamiltonian except all the states of m_j are now $-+++$. Additionally, because each of the four atoms can be randomly chosen as atom 1, only considering the case where atom 1 is in a different m_j state is sufficient for simulations.

$$H_{4\text{atom},0} = \begin{pmatrix}
0 & V_{RT1}^* & V_{RT1}^* & V_{RT0} & V_{RT0} & V_{RT0} & V_{RT0} & V_{RT0} & V_{RT0} & V_{RT0} & V_{RT0} & V_{RT1} & V_{RT1} & 0 & 0 & 0 & 0 & 0 & 0 \\
V_{RT1} & E & 0 & V_{s'p1} & 0 & V_{s'p1} & 0 & 0 & V_{sp1} & 0 & V_{sp1} & 0 & 0 & 0 & V_{RT1} & V_{RT1} & 0 & 0 & 0 \\
V_{RT1} & 0 & E & 0 & V_{sp1} & 0 & V_{sp1} & V_{s'p1} & 0 & V_{s'p1} & 0 & 0 & 0 & 0 & 0 & 0 & V_{RT1} & V_{RT1} & 0 \\
V_{RT0} & V_{s'p1}^* & 0 & E & 0 & V_{s'p0} & 0 & V_{sp0} & 0 & 0 & 0 & 0 & V_{sp1} & V_{RT0} & 0 & V_{RT0} & 0 & 0 & 0 \\
V_{RT0} & 0 & V_{sp1}^* & 0 & E & 0 & V_{sp0} & 0 & V_{s'p0} & 0 & 0 & V_{s'p1} & 0 & 0 & 0 & 0 & V_{RT0} & 0 & V_{RT0} \\
V_{RT0} & V_{s'p1}^* & 0 & V_{s'p0} & 0 & E & 0 & 0 & 0 & V_{sp0} & 0 & V_{sp1} & 0 & V_{RT0} & V_{RT0} & 0 & 0 & 0 & 0 \\
V_{RT0} & 0 & V_{sp1}^* & 0 & V_{sp0} & 0 & E & 0 & 0 & 0 & V_{s'p0} & 0 & V_{s'p1} & 0 & 0 & 0 & 0 & V_{RT0} & V_{RT0} \\
V_{RT0} & 0 & V_{s'p1}^* & V_{sp0} & 0 & 0 & 0 & E & 0 & V_{s'p0} & 0 & 0 & V_{sp1} & V_{RT0} & 0 & 0 & 0 & V_{RT0} & 0 \\
V_{RT0} & V_{sp1}^* & 0 & 0 & V_{s'p0} & 0 & 0 & 0 & E & 0 & V_{sp0} & V_{s'p1} & 0 & 0 & V_{RT0} & 0 & 0 & 0 & V_{RT0} \\
V_{RT0} & 0 & V_{s'p1}^* & 0 & 0 & V_{sp0} & 0 & V_{s'p0} & 0 & E & 0 & V_{sp1} & 0 & V_{RT0} & 0 & 0 & V_{RT0} & 0 & 0 \\
V_{RT0} & V_{sp1}^* & 0 & 0 & 0 & 0 & V_{s'p0} & 0 & V_{sp0} & 0 & E & 0 & V_{s'p1} & 0 & 0 & V_{RT0} & 0 & 0 & V_{RT0} \\
V_{RT1}^* & 0 & 0 & 0 & V_{s'p1}^* & V_{sp1}^* & 0 & 0 & V_{s'p1}^* & V_{sp1}^* & 0 & E & 0 & 0 & V_{RT1}^* & 0 & V_{RT1}^* & 0 & 0 \\
V_{RT1}^* & 0 & 0 & V_{sp1}^* & 0 & 0 & V_{s'p1}^* & V_{sp1}^* & 0 & 0 & V_{s'p1}^* & 0 & E & 0 & 0 & V_{RT1}^* & 0 & V_{RT1}^* & 0 \\
0 & 0 & 0 & V_{RT0} & 0 & V_{RT0} & 0 & V_{RT0} & 0 & V_{RT0} & 0 & 0 & 0 & 2E & 0 & 0 & 0 & 0 & 0 \\
0 & V_{RT1}^* & 0 & 0 & 0 & V_{RT0} & 0 & 0 & V_{RT0} & 0 & 0 & V_{RT1} & 0 & 0 & 2E & 0 & 0 & 0 & 0 \\
0 & V_{RT1}^* & 0 & V_{RT0} & 0 & 0 & 0 & 0 & 0 & 0 & V_{RT0} & 0 & V_{RT1} & 0 & 0 & 2E & 0 & 0 & 0 \\
0 & 0 & V_{RT1}^* & 0 & V_{RT0} & 0 & 0 & 0 & 0 & V_{RT0} & 0 & V_{RT1} & 0 & 0 & 0 & 0 & 2E & 0 & 0 \\
0 & 0 & V_{RT1}^* & 0 & 0 & 0 & V_{RT0} & V_{RT0} & 0 & 0 & 0 & 0 & V_{RT1} & 0 & 0 & 0 & 0 & 2E & 0 \\
0 & 0 & 0 & 0 & V_{RT0} & 0 & V_{RT0} & 0 & V_{RT0} & 0 & V_{RT0} & 0 & 0 & 0 & 0 & 0 & 0 & 0 & 2E
\end{pmatrix} \tag{3.18}$$

simulates the scenario where two p atoms start from states with negative m_j and the other two have positive m_j. The Hamiltonian for $pppp(--++)$ is shown here, and the basis state remains the same as the previous Hamiltonian except all the states of m_j are now $--++$.

Because which atom is labeled atom 1, atom 2, etc. is random, and flipping signs of all m_j only results in a different direction of phase evolution - with no effects on the population in each of the basis states, these three Hamiltonians are sufficient to simulate all possible configurations of the four atom ensemble. To take into account the random signs of m_j for the p states at the beginning of the evolution, we allocate 12.5%/50%/37.5% probability to $H_{4atom,2}/H_{4atom,1}/H_{4atom,0}$ when simulating four atom ensembles. Simula-

tion of the Rydberg atom gas ensemble typically involves ~10,000 randomly scattered four atom configurations (discussed in more detail later).

The probability of finding any one atom in a p state can be retrieved anytime during a simulation using

$$P(p) = \frac{1}{2}(1 + P(pppp) - P(sss's') - P(ss'ss') - P(ss's's) \\ - P(s'sss') - P(s'ss's) - P(s's'ss)), \tag{3.19}$$

where $P(x)$ represents the probability for finding the atoms in a particular basis state, x. Alternatively, we can write $P(s) = P(s') = \frac{1}{2}(1 - P(p))$.

3.4 Simulating Rydberg Atom Gases Using Two or Four Rydberg Atom Ensembles

With the law of larger numbers and the assumption that beyond nearest, or beyond third-nearest, neighbor interactions are weak, then by repeated simulation of the dynamics of two or four Rydberg atom ensembles, respectively, with random spatial configurations weighted according to their probability within a larger ensemble of a given density, we can simulate the dynamics within the larger ensemble. In that case, the final population distributions obtained for the individual two or four atom ensembles are incoherently summed to obtain the result for the full ensemble. This is known as the Monte Carlo method. In a typical simulation, 5000 to 10000 random ensembles are sampled. More details on the sampling process are discussed below.

All the Hamiltonians described previously require the identification of specific spatial coordinates of all atoms involved. For two atom ensembles, one ion core is placed at the origin ($R = 0, \theta = 0, \phi = 0$), and the distance between the two atoms is chosen to follow the nearest neighbor distribution function, $G(R) = 4\pi\rho R^2 e^{-\frac{4}{3}\pi\rho R^3}$, where ρ is the density of the Rydberg atom gas. The orientation angles, θ and ϕ, for the second atom are selected based on a uniform distribution between $(0, \pi)$ and $(0, 2\pi)$ respectively. To simulate four atom ensembles, 99 atoms, each described by Cartesian coordinates (x_i, y_i, z_i) are first randomly placed in a cube, the length of each edge measuring $\sqrt[3]{\frac{100}{\rho}}$, assuming a uniform distribution along each of the three spatial coordinates. We then place an atom at the center of the cube. This atom, along with its three nearest neighbors define an ensemble of four. The relative position vector between each pair $\overrightarrow{\boldsymbol{R_{ab}}} = (R_{ab}, \theta_{ab}, \phi_{ab})$ is derived from their respective Cartesian coordinates and plugged into the different Hamiltonians.

To include the thermal motion of atoms, each atom is assigned a velocity $\overrightarrow{\boldsymbol{v}} = (v_x, v_y, v_z)$, where the values of v_x, v_y, v_z each follow Gaussian distributions with mean values of 0 and standard deviation $\sqrt{\frac{kT}{m}}$. Beyond thermal motion, the spatial dependence of the dipole-dipole interaction exerts forces on the atoms, $\left|\overrightarrow{\boldsymbol{F_{DD}}}\right| = \left|\frac{\partial\langle pp|V_{DD}|ss'\rangle}{\partial R}\right| \leq \left|\frac{3\langle p|\hat{r}|s\rangle\langle p|\hat{r}|s'\rangle}{2R^4}\right|$. The acceleration of an atom due to dipole-dipole forces is $\frac{\left|\overrightarrow{\boldsymbol{F_{DD}}}\right|}{m}$, where m is the mass of a ^{85}Rb atom. The acceleration of an atom that is at the average interatomic distance, R_{avg}~3.8μm away from its nearest neighbor at a Rydberg density of $3 \times 10^9/\text{cm}^3$ is $0.03\mu\text{m}/\mu\text{s}^2$. Thus, over the typical timescale ($<1\mu$s) of our experiments, the effects of dipole-dipole induced acceleration

is much smaller than the ~0.19μm/μs average relative thermal velocity between a pair of atoms. Thus, the effects of dipole-dipole induced motion can be neglected in simulations. With thermal motion of atoms being considered, the coordinates of each atom are now a function of time $(x_i(t), y_i(t), z_i(t)) = (x_i(0) + v_{xi} \cdot t, y_i(0) + v_{yi} \cdot t, z_i(0) + v_{zi} \cdot t)$, and the relative position of the atoms $\overrightarrow{\boldsymbol{R_{ab}}} = (R_{ab}, \theta_{ab}, \phi_{ab})$ must be re-analyzed at each time step during the simulation. The resulting time-dependent Hamiltonian simulates the decoherence due to thermal motion of atoms, and the coupling of electronic and nuclear degrees of freedom.

Our MOT has a density distribution that is approximately Gaussian, rather than uniform. This also needs to be taken into account to properly model the experimental conditions. In the experiments described in this dissertation, Rydberg atoms are excited within a narrow cylinder created by the intersection of the tightly focused blue laser beam and the spherical Gaussian distribution of the MOT, which has a relatively large diameter. Accordingly, the Rydberg density approximately follows a 1D Gaussian distribution. To simulate this, the density of the ensemble could be changed from a constant to a variable that follows a Gaussian distribution. However, in practice, this approach did not work well as the simulation did not run well at extremely low densities. As an alternative, the behavior of the Rydberg ensemble was computed at several fixed densities, and the results were summed with weights reflecting the measured Gaussian distribution, i.e., integral of area within 1D Gaussian distribution where y value falls within certain range. For example, for an ensemble with a peak density of $3 \times 10^9/\text{cm}^3$, a parameter A of the ensemble

can be approximated as $A(\text{ensemble}) = 0.454 \cdot A(3 \times 10^9/\text{cm}^3) + 0.178 \cdot A(2.5 \times 10^9/\text{cm}^3) + 0.129 \cdot A(2 \times 10^9/\text{cm}^3) + 0.101 \cdot A(1.5 \times 10^9/\text{cm}^3) + 0.080 \cdot A(1 \times 10^9/\text{cm}^3) + 0.058 \cdot A(0.5 \times 10^9/\text{cm}^3)$, independent of the width of the spatial distribution.

Beyond those explicitly discussed here, other parameters subject to inhomogeneity (for example electric field) can also be simulated by changing the parameter from a constant to a variable following a model distribution. Based on estimates, it is assumed that the variation of other experimental parameters does not play a critical role in the experimental results, and therefore, they are not included in the simulations.

3.5 Numerical Tricks for Higher Accuracy and Faster Calculation

Time-dependent simulations of the behavior of a quantum ensemble are straightforward, in principle, as only the time dependent Schrödinger equation $i\hbar\frac{\partial}{\partial t}|\Psi(t)\rangle = \hat{H}|\Psi(t)\rangle$ is needed, given the Hamiltonians presented above. In practice though, applying the Hamiltonians directly can result in numerical difficulties. For example, the amplitudes in coupled basis states can oscillate back and forth at very high frequencies due to (on or off resonant) Rabi oscillations, and to accurately compute the time-dependent amplitude in each basis state, the sample rate of the evolution must be significantly higher than the highest Rabi oscillation frequency within the ensemble [88]. This can be computationally time-consuming. Moreover, with each time step, truncation errors always

occur in numerical simulations. With a high sampling rate and long evolution times, the accumulated truncation error can render the simulation inaccurate.

Thus, the key to fast and accurate simulations is to reduce the Rabi frequency associated with the coupling between the various basis states. Using the eigenstates of the Hamiltonian as a basis can solve the problem. Being eigenstates, the population in those basis states remains constant as long as the Hamiltonian remains the same. If the Hamiltonian is unchanged, only phase evolution, which is linear in time, needs to be taken into consideration. Therefore, to calculate the behavior of an ensemble at any given time, one can first map the initial conditions onto the system eigenstates, then calculate the phase evolution of each eigenstate from the initial time to the final time, before mapping the amplitudes back to the bare, uncoupled levels, whose populations are our experimental observables. Of course, to account for the change of the Hamiltonian due to atom motion (or a change in detuning due to a pulsed-electric field, as discussed in next chapter), the evolution of the system still needs to be broken up into separate intervals, as the eigenstates of the Hamiltonian and the projections to/from the uncoupled eigenstate basis change. But given that atom motion is slow, and there are relatively few detuning steps within the experiments, the Hamiltonian does not change much as a function of time and/or it changes only a few times during the evolution (due to the application of control fields). Thus the required temporal sampling rate is not high. Accordingly, by mapping the ensemble onto the system eigenstates, the evolution can be calculated quickly and accurately, even if the Hamiltonian is time-dependent.

In the next chapter we describe experiments in which the system is coherently transported back and forth between detuning values of 0 and $\pm E$, relative to energy transfer resonance, using pulsed electric fields. To take better advantage of the RAM capabilities of modern computers to accelerate the calculation, a lot of repeatedly used values can be pre-calculated and stored. In a typical simulation involving 400ns of system evolution, the quantum states are evaluated every 4ns. For each 4ns period featuring a different Hamiltonian, e.g., due to atom motion, the results of (1) mapping the bare states to eigenstates, (2) evolving the system for 4ns, and (3) mapping back to the bare states, can all be multiplied together as one matrix and pre-calculated for different scenarios of the ensemble in the presence of different control fields at that particular time. In this way, for different control scenarios, all that is required to evaluate the system at a given time is to evolve the system 4ns at a time from the initial condition utilizing those pre-calculated evolution matrices. Additionally, amplitudes in each basis state at a particular evolution time can be stored, reducing computational time in cases where the system evolves identically from the start of the simulation up to a particular time.

3.6 Comparison Between Simulation Results Based on Two or Four Rydberg Atom Ensembles

To better understand the individual effects of the inhomogeneous atom distribution, inhomogeneous orientation, and hopping effects on the evolution of the Rydberg ensemble (see chapter 5 for more details on the effects of excitation hopping), and to gauge whether the model used in the simulations captures the essential aspects of the experiments, two routine measurements are performed and their results are compared with simulation data: (1) measurement of the time-dependent population in p, s, and s' states as a function of time, after an ensemble of initially excited p atoms is suddenly energy tuned to enable pp to ss' resonant energy transfer; and (2) measurement of the resonance lineshape, i.e., the population transfer probability from pp to ss' as a function of a static electric field induced detuning.

3.6.1 Population in p, s and s' states as a Function of Time

When an isolated pair of stationary p atoms is suddenly brought into energy transfer resonance with ss' (i.e., the strong dipole-dipole coupling between the atoms is suddenly switched on), one would expect Rabi oscillations in the probability of finding the atom pair in pp or ss' states as a function of time.

The population in pp and ss' as a function of time should be

$$P(pp(t)) = \frac{1}{2}(1 + \cos\Omega t), \tag{3.20}$$

$$P(ss'(t)) = \frac{1}{2}(1 - \cos\Omega t) \tag{3.21}$$

respectively, with $\Omega = 2|\langle pp| V_{DD} |ss'\rangle|$. As discussed previously, the dipole-dipole interaction strength is a function of interatomic distance, as well as the angle between the interatomic axis and the external electric field. Therefore, within each local ensemble of two or four atoms, atom pairs oscillate between pp and ss' configurations at different Rabi frequencies, resulting in a rapid dephasing of the Rabi oscillations when the results from individual local ensembles are integrated over the whole. To directly see the effects of dephasing, a series of five simulations were performed to determine the time dependent populations in pp and ss', including system inhomogeneities at various levels. These are: (1) a single pair of atoms with an interatomic distance equal to the average nearest neighbor separation at a density ρ $\left(R = R_{\text{avg}} = \sqrt[3]{-\frac{3}{4\pi\rho}\ln 0.5}\right)$, and average angular coupling strength (so that $\langle pp| V_{DD} |ss'\rangle = -\frac{\langle p|\hat{r}|s\rangle\langle p|\hat{r}|s'\rangle}{6R^3}$); (2) ensembles of atom pairs with interatomic distances varying according to the nearest neighbor distribution function for a random ensemble at density ρ, but with the same average angular coupling strength for all pairs; (3) ensembles of atom pairs at density ρ with varying interatomic distances as well as orientation angles; (4) ensembles of four atom groups at density ρ with random relative positions; and (5) ensembles of four atom groups with random relative positions, and a Gaussian density distribution peaking at density ρ.

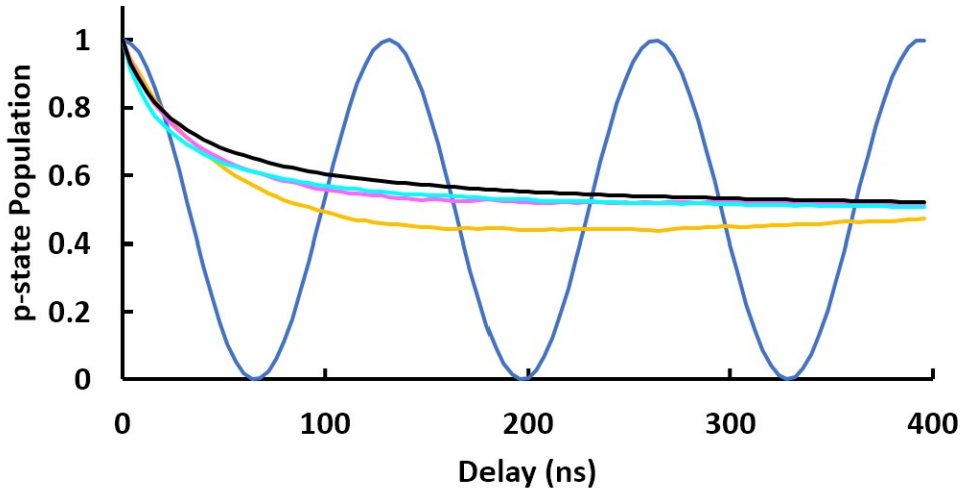

Figure 3.6: Simulated p-state population (normalized to total population) as a function of time when an ensemble of p atoms with peak Rydberg density $\rho \sim 3 \times 10^9/\text{cm}^3$ is suddenly tuned to energy transfer resonance with ss', for: (blue) a single pair of atoms separated by the average interatomic distance at density ρ and average angular coupling strength; (yellow) ensembles of atom pairs at density ρ with varying interatomic distances but average angular coupling strength; (magenta) ensembles of atom pairs at density ρ with varying interatomic distances as well as orientation angles; (cyan) ensembles of four atom groups at density ρ with random relative positions; and (black) ensembles of four atom groups with a Gaussian density distribution peaking at density ρ and random relative positions.

In all cases, the probability that the initial population remains in the state pp is computed as a function of time after an initial ensemble of p atoms is suddenly brought into energy transfer resonance, pp to ss' (see Figure 3.6).

It is clear that as the system become less ordered from (1) to (5), the the decay of the Rabi oscillations happens faster, suggesting faster dephasing, which is what we expect. It is remarkable that the results of the relatively simple simulations corresponding to (3) (atom pairs with varying interatomic distances and random orientations) are nearly identical to those of (4) which

includes four atoms and non-nearest neighbor interactions. Apparently, the time-dependent populations for on resonance cases are not strongly affected by non-nearest neighbor interactions, as previous research on similar systems has found [30, 70, 81, 82].

Figure 3.7 shows a comparison between simulation (5) (four atom groups with a Gaussian density distribution and random relative positions) results with experimental data collected at the same peak density. The agreement between measurement and simulation is quite good, although not perfect. The limitations of the 4-atom model will be discussed later, and the imperfections of the experiments will be discussed in Chapter 4.

3.6.2 Lineshape of pp to ss' Transition

When a single pair of p atoms is suddenly brought near pp to ss' energy transfer resonance, but with the bare states detuned by an energy δ from perfect resonance, one would expect off resonance Rabi oscillations in the pp or ss' populations. The population (normalized to total population) in ss' as a function of time is

$$P(ss'(t)) = \frac{\Omega^2}{\widetilde{\Omega}^2}\sin^2\frac{\widetilde{\Omega}t}{2}, \tag{3.22}$$

with $\Omega = 2|\langle pp|\, V_{DD}\, |ss'\rangle|$, $\widetilde{\Omega} = \sqrt{\Omega^2 + \delta^2}$. Accordingly, if an ensemble of p atoms is brought near resonance for an extended period of time (500ns), the ensemble would dephase and one might expect the population in ss' to simply be

$$P(ss') = \frac{\Omega^2}{2\widetilde{\Omega}^2} = \frac{1}{2}\frac{\Omega^2}{\Omega^2 + \delta^2}, \tag{3.23}$$

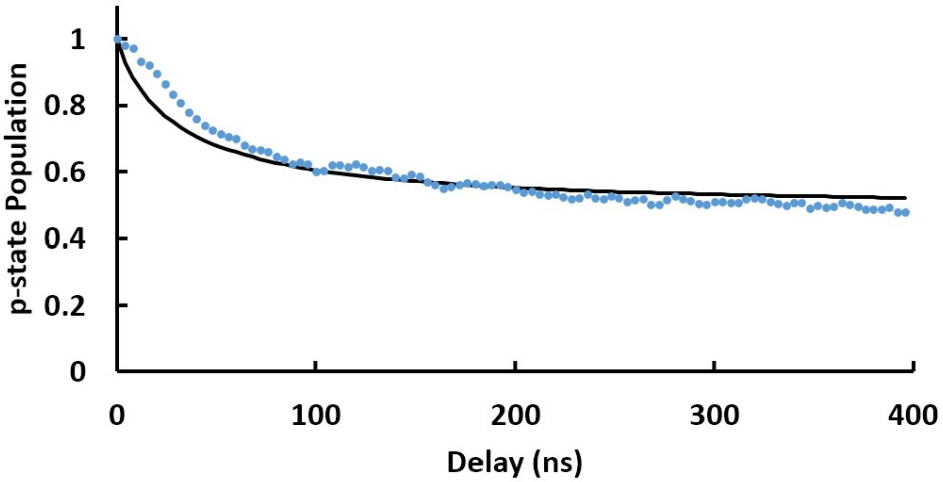

Figure 3.7: Population in p state (normalized to total population) as a function of time after an ensemble of $32p$ atoms with peak density $\rho{\sim}3 \times 10^9/\mathrm{cm}^3$ is brought onto energy transfer resonance, pp to ss'. Shown are experimental (blue dots) and simulation (black line) results based on ensembles of four atom groups with a Gaussian density distribution and random relative positions. The experimental data is normalized to 1 at $t = 0$, and to 0.5 at the maximum delay. The latter based on the assumption that the experimental evolution time is sufficiently long that the system has reached a maximally mixed state with 50% probability of finding the system in the pp or ss' configuration.

i.e., exhibiting a Lorentzian lineshape as a function of detuning. However, the effect of inhomogeneity in Rydberg atom gas is beyond fast dephasing, and the inhomogeneity in the dipole-dipole coupling between atoms changes the resonance lineshape as well. Considering the variations in interatomic distances between atom pairs in a random ensemble (following the nearest neighbor distribution function), the predicted lineshape changes from a Lorentzian to a cusp [36]

$$P(ss') = \frac{a}{2}\left\{\mathrm{Ci}(a)\sin(a)\left[\frac{\pi}{2} - \mathrm{Si}(a)\right]\cos(a)\right\}, \tag{3.24}$$

where $a = \frac{2\Omega}{3\delta}$, $\mathrm{Si}(x) = \int_0^x \frac{\sin(u)}{u}du$ is the sine integral, $\mathrm{Ci}(x) = \gamma + \ln(x) + \int_0^x \frac{\cos(u)-1}{u}du$ is the cosine integral, and $\gamma \approx 0.577216$ is Euler's constant [89].

The Lorentzian lineshape describes the case for one or more pairs of atoms with a fixed interatomic distance and average angular coupling strength. The cusp lineshape describes the case for ensembles of pairs of atoms at a fixed density with varying interatomic distances, but average angular coupling strength. However, the actual Rydberg atom ensembles used in the experiments are more complicated. To understand the roles of additional inhomogeneities, we perform simulations for the following additional cases: (3) ensembles of pairs of atoms at a fixed density with random interatomic distances and orientation angles; (4) ensembles of four atom groups at a fixed density and random relative positions; and (5) ensembles of four atom groups with a Gaussian density distribution and random relative positions. The lineshapes corresponding to all five cases are compared in Figure 3.8.

As the system becomes less ordered from case (1) to (3), the lineshape becomes narrower at small detunings, but with more pronounced wings at large

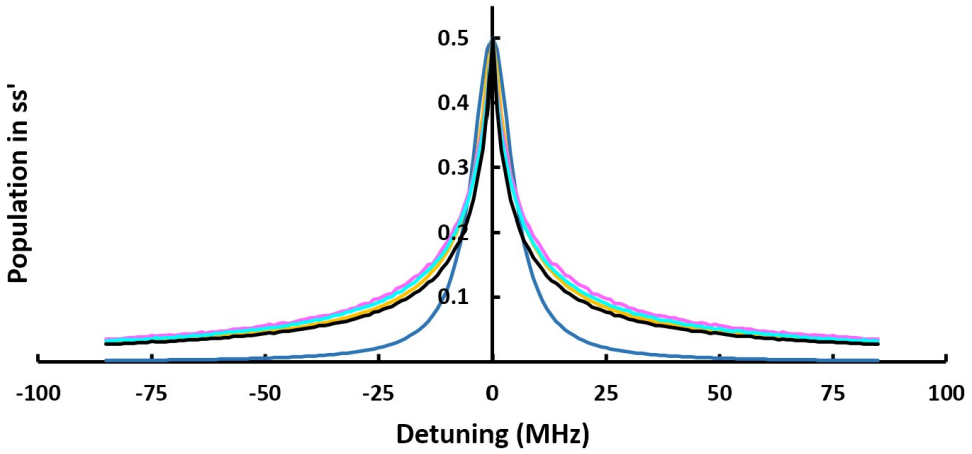

Figure 3.8: Population in ss' (normalized to total population) as a function of detuning, 500ns after an ensemble of p atoms with peak Rydberg density $\rho = 2 \times 10^9/\text{cm}^3$ is suddenly tuned near the pp to ss' energy transfer resonance. (blue) A pair of atoms with interatomic distance corresponding to the average nearest neighbor separation at density ρ and average angular coupling strength; (yellow) Ensembles of pairs of atoms at density ρ with varying interatomic distances but average angular coupling strength; (magenta) Ensembles of pairs of atoms at density ρ with varying interatomic distances and random orientation angles; (cyan) Ensembles of four atom groups at density ρ with random relative positions; (black) Ensembles of four atom groups with a Gaussian density distribution peaking at density ρ and random relative positions.

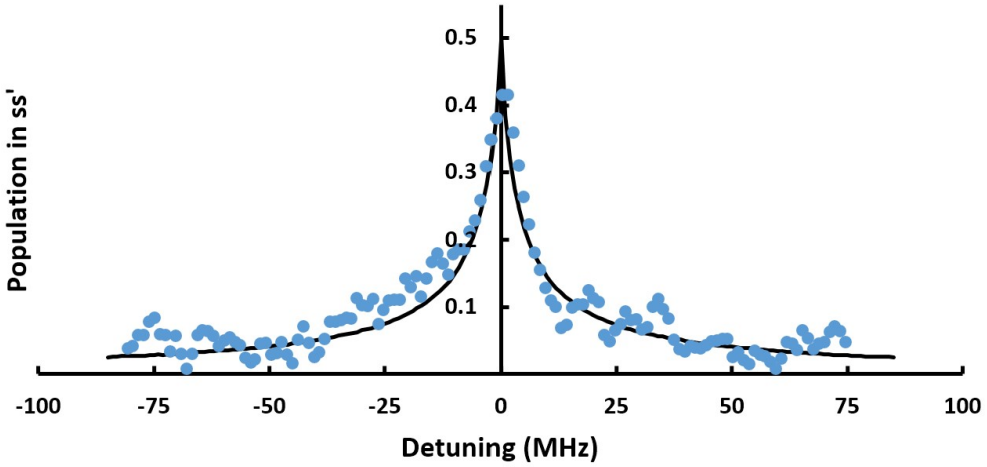

Figure 3.9: Population in ss' state (normalized to total population) as a function of detuning, 500ns after an ensemble of p atoms with peak Rydberg density ρ~$2 \times 10^9/\text{cm}^3$ is tuned near pp to ss' energy transfer resonance, according to: experimental results (blue dots - vertically rescaled ($y' = ay + b$) to best fit the simulation results) and simulations (black line) based on ensembles of four atom groups with a Gaussian density distribution peaking at density ρ and random relative positions (black line).

detunings, while the FWHM remains the same. Cases (4) and (5) produce a somewhat narrower lineshape. Comparing case (5) with experimental results (Figure 3.9), the FWHM of the simulated lineshape is slightly narrower than observed experimentally, but overall the simulated lineshape reproduces the experimental results nicely.

Because the analytical cusp lineshape is very similar to the experimental lineshape and the simulated lineshapes using two or four atom group ensembles, the cusp lineshape expression can be used to fit the experimental data and extract the FWHM of experimental lineshape. Lineshapes have been measured at different Rydberg atom densities. The FWHM of the measured lineshapes can be compared to simulations or analytical results as shown in

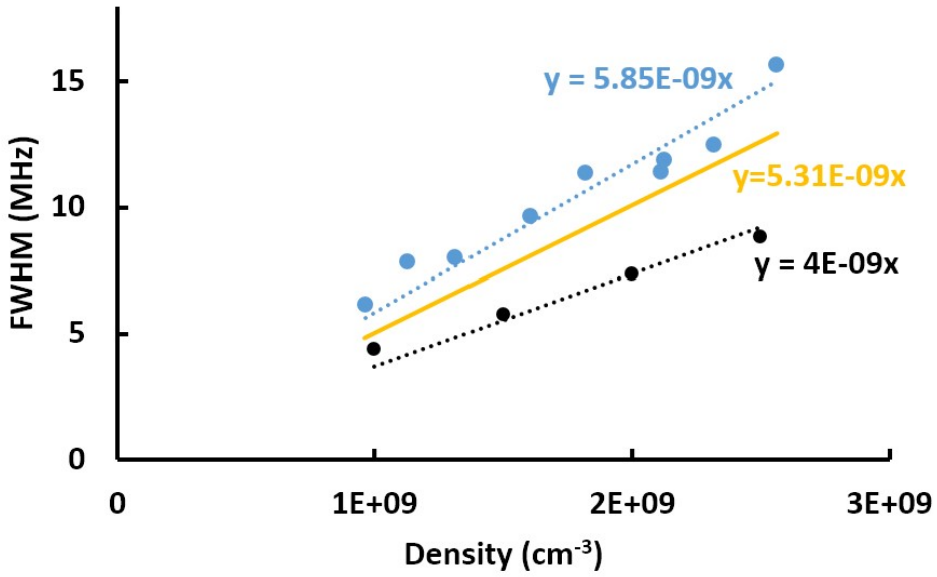

Figure 3.10: FWHM of pp to ss' resonance lineshapes as a function of Rydberg atom density, according to experimental results (blue dots with blue dotted linear fit), analytical calculations considering pairs of atoms at peak density with varying interatomic distances but average angular coupling strength (yellow line), and simulations with ensembles of four atom groups with a Gaussian density distribution and random relative positions (black dots with black dotted linear fit). Note that the FWHM of the lineshapes from the four atom groups simulations fall slightly above (below) the linear fit at lower (higher) densities. This is because the number of lineshapes at different densities included in the weighted sum representing the Gaussian distribution is smaller at low densities, resulting in a less accurate approximation.

Figure 3.10.

The FWHM of the four atom simulation results is consistently smaller than experimental values. This could be attributed to ignoring thermal motion of atoms in this particular simulation, the inaccuracy of Rydberg density determination from MOT fluorescence, the inaccuracy of extracting the FWHM from noisy experimental data, and/or several other possible reasons discussed

in next section.

3.7 Rydberg Blockade

In the experiments, due to the narrow linewidth of the Rydberg excitation, short range dipole-dipole interactions can shift the energies of closely spaced atoms beyond the Rydberg excitation bandwidth. This so called Rydberg blockade can prohibit the excitation of pairs of atoms with small interatomic separations [16, 17, 18]. The approximate excitation bandwidth in our experiments is the convolution of the natural linewidth of the $5p$ state (Lorentzian, FWHM~6.1MHz) [67] from which the blue laser excites Rydberg states, with the frequency spectrum of the pulsed blue laser (approximately a Sinc function with a ~3.3MHz FWHM), resulting in an effective excitation bandwidth of $\approx$ 6.9MHz. In experiments, the laser excitation occurs in a field for which pairs of atoms are detuned from the pp to ss' energy transfer resonance by δ=85MHz. Accordingly, the pp to ss' interaction dominates the van der Waals-like couplings responsible for the Rydberg blocakde. In the limit of $\delta \gg |\langle pp| V_{DD} |ss'\rangle|$, the energy shift of the atom pair eigenstates due to the off-resonant dipole-dipole interaction is approximately

$$\Delta E = \frac{1}{2}\left(\sqrt{4|\langle pp| V_{DD} |ss'\rangle|^2 + \delta^2} - \delta\right) \approx \frac{|\langle pp| V_{DD} |ss'\rangle|^2}{\delta}. \tag{3.25}$$

Using dipole-dipole interaction strengths derived above (equations 3.4, 3.5, 3.6), we can write

$$\Delta E = \frac{1022}{R^6} \cdot \frac{9}{4}\sin^4\theta \text{ MHz} \cdot \mu\text{m}^6 \tag{3.26}$$

(for $pp(\pm\pm)$ initial states),

$$\Delta E = \frac{1022}{R^6}\left(-1+\frac{3}{2}\sin^2\theta\right)^2 \text{ MHz}\cdot\mu\text{m}^6 \tag{3.27}$$

(for $pp(\pm\mp)$ initial states).

Comparing ΔE with the 6.9MHz linewidth (suppose the excitation spectrum is a box function with a width of 6.9MHz), we can define a Rydberg blockade radius as the nearest separation of the two excited atoms in our experiments, as

$$R_{blockade} = 2.3\sqrt[3]{\frac{3}{2}}\sin^{\frac{2}{3}}\theta\ \mu\text{m} \tag{3.28}$$

(for $pp(\pm\pm)$ initial states),

$$R_{blockade} = 2.3\left(-1+\frac{3}{2}\sin^2\theta\right)^{\frac{1}{3}}\ \mu\text{m} \tag{3.29}$$

(for $pp(\pm\mp)$ initial states).

This gives a maximum Rydberg blockade radius of ~2.6μm. To simulate the potential impact of the Rydberg blockade, we can simply eliminate from the Monte Carlo calculations any randomly selected 2 or 4 atom ensembles that contain two or more Rydberg atoms separated by less than the (angle-dependent) blockade radius.

An additional complication to the blockade effect is the role of saturation of the Rydberg excitation. In experiments, a sufficiently large blue laser intensity is used to ensure that the product of the on-resonance Rabi frequency and the blue laser duration is significantly larger than π. As a result, even pairs

of atoms with energies outside the excitation bandwidth can still be efficiently excited. Accordingly, the effective Rydberg blockade radius would be less than that calculated above. Thus, the results of simulations based on the assumption that there is a minimum atom separation equal to the maximum Rydberg blockade radius derived above, as well as others that completely ignore the blockade effect, are both provided here for comparison with experiment (see Figures 3.11 and 3.12). The conditions of actual experiments fall somewhere between these two limiting cases. The impact of Rydberg blockade on the measurement results will again be considered in Figures 4.2 and 4.4. Given that the simulation results including blockade effects do not provide consistently better agreement with experiments, in later chapters, only the simpler model that does not consider Rydberg blocakde is used.

3.8 Limitations of Current Simulations

Although several additional considerations have been taken into account to simulate the evolution of a Rydberg gas in this dissertation as compared to previous efforts [5, 30, 37], there are still some effects that the current model does not include. The first is the non-zero rise and fall times of the detuning pulses. In simulations, the jump between different detunings is considered to be instantaneous. In reality, the rise and fall times for the AWG are ~2ns, with some ringing in the applied voltage pulse persisting for ~5ns after the detuning jump. How this imperfect detuning transition affects the experimental results will be briefly discussed in the next chapter in the context of other

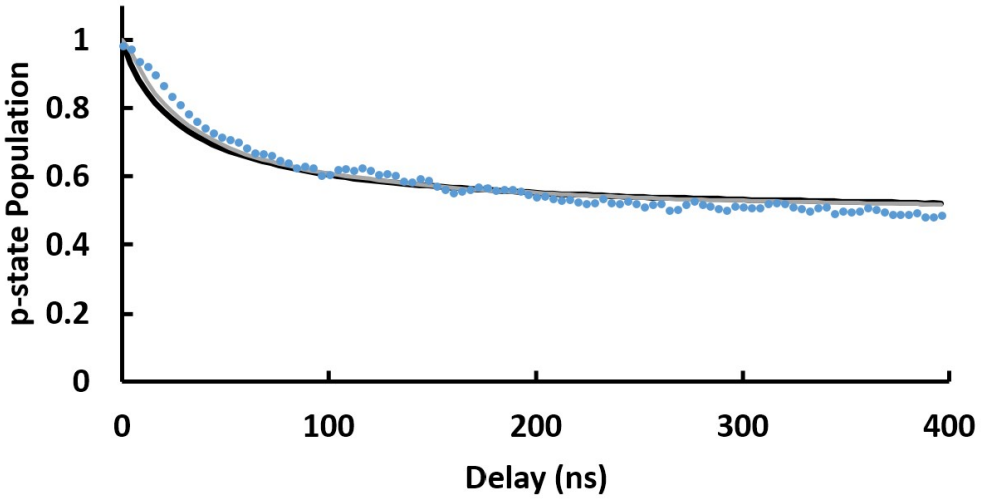

Figure 3.11: Population in p state (normalized to total population) as a function of time after an ensemble of $32p$ atoms with peak density $\rho \sim 3 \times 10^9/\mathrm{cm}^3$ is brought into energy transfer resonance, pp to ss'. Shown are experimental (blue dots) and simulation results considering (grey line) or not considering (black line) Rydberg blockade effects based on ensembles of four atom groups with a Gaussian density distribution and random relative positions.

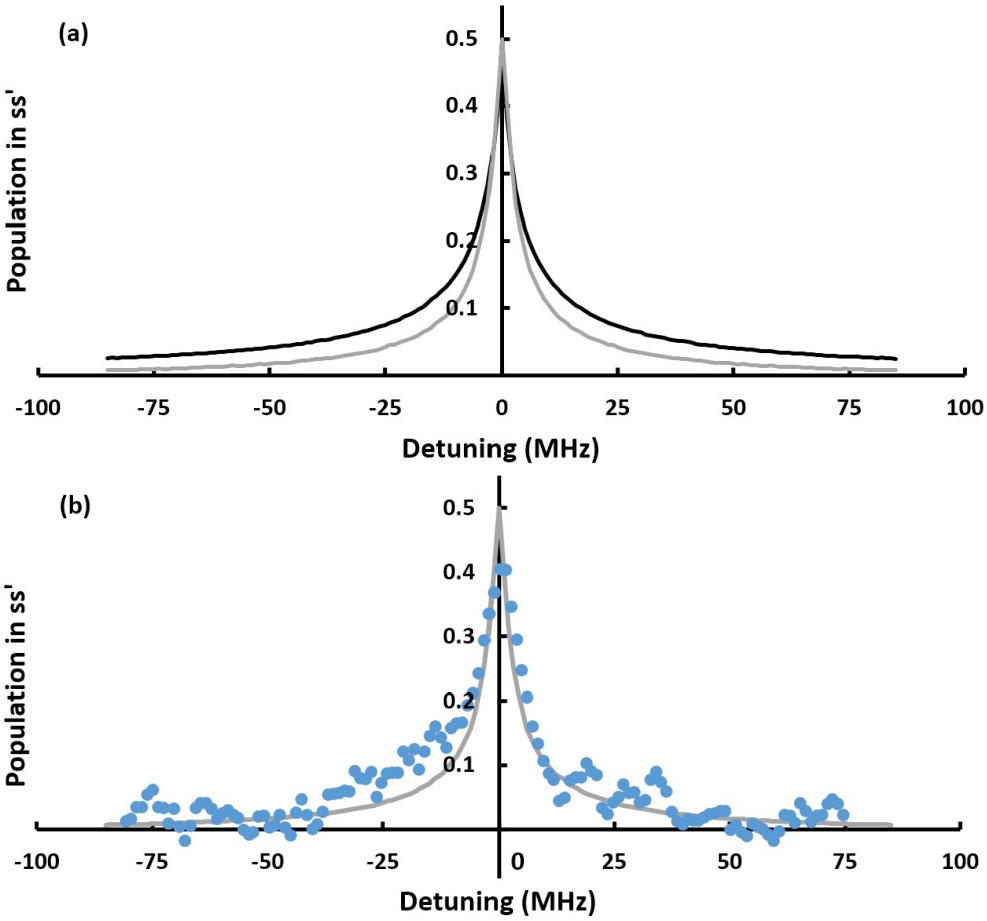

Figure 3.12: Population in ss' state (normalized to total population) as a function of detuning, 500ns after an ensemble of p atoms with peak Rydberg density ρ~$2\times10^9/\mathrm{cm}^3$ is tuned near pp to ss' energy transfer resonance. Shown are comparisons between (a) simulation results considering (grey line) or not considering (black line) Rydberg blockade and (b) experimental data (blue dots - vertically rescaled ($y' = ay + b$) to best fit the simulation results). The agreement between simulation and experiment in (b) should be compared to that in Figure 3.9. Inclusion of the blockade effect does not improve the agreement between measurement and simulation. All simulations are based on ensembles of four atom groups with a Gaussian density distribution peaking at density ρ and random relative positions.

measurements, but it has not been modeled in the simulations. Additionally, the current simulations did not take into consideration the effects of blackbody radiation or spontaneous decay of p, s and s' states, with the s and s' states having lifetimes of ~20μs [90, 91]. Given that the experiments and simulations considered in this dissertation are concerned with the system evolution over times <1μs, spontaneous decay and blackbody redistribution should not have a significant impact on the results. However, these effects cannot be reasonably neglected in simulations extending to significantly longer times. Another approximation that could not be readily extended to longer evolution times is the neglect of dipole-dipole induced acceleration of atoms, as previously discussed. Last but not least, although simulations based on four atom ensembles include excitation hopping effects at some level, hopping beyond four atoms may be important under some conditions. While hopping apparently does not play an important role in the on resonance energy transfer discussed in this chapter, it is more important for the off-resonance cases [71, 78, 79, 80, 84, 85, 86], as discussed in Chapter 5.

Armed with reasonably accurate simulation models and a good understanding of the behavior of Rydberg atom gas subject to *resonant* dipole-dipole interactions, it is now time to discuss the behavior of Rydberg atom gas subject to *near resonant* dipole-dipole interactions, which is the focus of chapter 4.

Chapter 4

Suppressing Dephasing in a Rydberg Atom Gas

Towards the end of the last chapter, the effects of dephasing in a random dipole-dipole coupled gas were shown through the results of simulations and experiments. Specifically, the amplitude of Rabi oscillations between pp and ss' (continuing the abbreviation from last chapter) decays rapidly for the ensemble as a whole, because the Rabi frequency varies substantially across local micro-ensembles due to variations in the dipole-dipole interaction strength throughout the Rydberg gas. In this chapter we describe an approach for observing Rabi oscillations in a random Rydberg ensemble, despite those inhomogeneities. Although the techniques discussed in this chapter may not increase the dephasing time of a random Rydberg atom gas to be on par with more ordered ensembles like a Rydberg atom lattice or Rydberg atom tweezer

arrays, the quantum control techniques we demonstrate should also be applicable for more ordered systems, as will be discussed in chapter 7. In addition, the techniques explored in this chapter might also be employed to reduce local decoherence as well.

Extracting quantum information from noisy inhomogeneous environments has long been an active area of research, from quantum error correction codes [92, 93, 94, 95, 96, 97, 98, 99, 100, 101, 102, 103, 104] to dynamical decoupling [105, 106, 107, 108, 109, 110, 111, 112, 113, 114]. In this chapter, we describe the use of detuning jump sequences to suppress dephasing in an inhomogeneous ensemble. The sequence used in this chapter was originally developed by Kutteruf and Jones for measuring coherence times in dipole-dipole coupled gases [37]. The principle of the sequence is very similar to that of quasi-phase-matching used in nonlinear optics [115, 116, 117], which was also engineered to suppress dephasing. Thus, by employing the same sequence as Kutteruf and Jones, over time scales shorter than the dephasing time in a Rydberg gas ensemble, suppression of dephasing can be achieved.

4.1 Suppressing Dephasing with Detuning Jumps

Using the models discussed in the previous chapter, consider a single pair of p atoms detuned, at $t = 0$, from the pp to ss' energy transfer resonance by an energy δ. Then, assuming microscopic coherence is preserved within the atom pair (e.g., the atoms are not moving relative to each other or subject to other

time-dependent interactions), the population in ss' as a function of time is

$$P(ss'(t)) = \frac{\Omega^2}{2\widetilde{\Omega}^2}\left(1 - \cos\widetilde{\Omega}t\right), \tag{4.1}$$

with $\Omega = 2|\langle pp|\, V_{DD}\, |ss'\rangle|$, $\widetilde{\Omega} = \sqrt{\Omega^2 + \delta^2}$. Suppose the detuning is equal to δ for a time $T/2$ before shifting to $-\delta$ for an additional time $T/2$. Then the population in ss' at time T is

$$P(ss'(T)) = \frac{\Omega^2}{2\widetilde{\Omega}^2}\left(1 - \cos\widetilde{\Omega}T + \frac{\delta^2}{\widetilde{\Omega}^2}\left(3 + \cos\widetilde{\Omega}T - 4\cos\frac{\widetilde{\Omega}T}{2}\right)\right). \tag{4.2}$$

In the limit of $\delta \gg \Omega$,

$$P(ss'(T)) = \frac{2\Omega^2}{\widetilde{\Omega}^2}\left(1 - \cos\frac{\widetilde{\Omega}T}{2}\right). \tag{4.3}$$

If $\mathcal{N}$ jumps between positive and negative detunings are made during the total interval T, with a time at a given detuning δ of $\frac{T}{2\mathcal{N}}$, then in the limit of $\delta \gg \Omega$ and net population transfer $\ll 1$, we have

$$P(ss'(T)) = \frac{2\mathcal{N}^2\Omega^2}{\widetilde{\Omega}^2}\left(1 - \cos\frac{\widetilde{\Omega}T}{2\mathcal{N}}\right). \tag{4.4}$$

Now consider a random Rydberg ensemble consisting of many pairs of Rydberg atoms featuring different $\widetilde{\Omega}$ following a distribution of $f(\widetilde{\Omega})$ (with $\int f(\widetilde{\Omega})\, d\widetilde{\Omega} = 1$) subject to the same jump sequence. The population in ss' in the ensemble can be written as $P(ss'(T)) = \int \frac{2\mathcal{N}^2\Omega^2}{\widetilde{\Omega}^2}\left(1 - \cos\frac{\widetilde{\Omega}T}{2\mathcal{N}}\right) f(\widetilde{\Omega})\, d\widetilde{\Omega}$. This means the ensemble integrated population should still exhibit (damped)

Rabi oscillations, but with a frequency given by the ensemble average of $\frac{\widetilde{\Omega}}{2\mathcal{N}}$. Interestingly, the damping rate, or the inverse of the effective dephasing time, scales with the width of the $\frac{\widetilde{\Omega}}{2\mathcal{N}}$ distribution, decreasing as $\frac{1}{2\mathcal{N}}$ for $\mathcal{N}$ jumps as compared to an ensemble not subject to detuning jumps. In addition, the amplitude of Rabi oscillations increases by a factor of $4\mathcal{N}^2$ as compared to an ensemble not subject to detuning jumps (in the limit of $\delta \gg \Omega$ and net population transfer $\ll 1$).

Taking a closer look at the generalized Rabi frequency, $\widetilde{\Omega} = \sqrt{\Omega^2 + \delta^2}$, in the large detuning regime, $\widetilde{\Omega} \approx \delta + \frac{\Omega^2}{2\delta}$. For our dipole-dipole mediated resonant energy transfer, the resonance frequency is not affected by the inhomogeneous atom distribution within the Rydberg atom gas ensemble, meaning the detuning δ is well-defined (assuming any electric field inhomogeneity across the ensemble is negligible). Thus, the spread in $\widetilde{\Omega}$ comes solely from the $\left|\frac{\Omega^2}{2\delta}\right|$ term, decreasing as the detuning increases. To summarize, large jump numbers $\mathcal{N}$, paired with large detuning, results in a significant increase in dephasing time.

Another useful parameter to examine is the number of Rabi oscillations that can be observed within the dephasing time. This, for example, might determine the number of quantum logic operations that can be performed for a physical architecture, since the Rabi oscillation frequency sets an effective "clock speed" while the dephasing time determines the useful lifetime of stored information (if no other dephasing suppression sequences like echo sequences are performed). In this regard, an ensemble subject to the detuning jump sequence exhibits no difference from an ensemble subject to large detuning Rabi oscillations with no jumps, as both the Rabi oscillation frequency and

the dephasing rate are decreased by a factor of $2\mathcal{N}$ when an ensemble is subject to $\mathcal{N}$ jumps. However, thanks to the amplitude amplification term $\frac{2\mathcal{N}^2\Omega^2}{\tilde{\Omega}^2}$, the jump sequence can facilitate larger population transfer to ss' states, as compared to the no jump, large detuning case. The ability to achieve large uniform population transfer is desirable for engineering quantum control sequences which might require the specific population transfer probabilities between two states. Additionally, for applications that do not necessarily require large uniform population transfer, larger population transfer can still be helpful because it can yield a better signal to noise ratio for measurements based on that transfer.

4.2 Experimental Demonstration of Dephasing Suppression

To experimentally verify if the jump sequences can actually suppress dephasing, as predicted, we first create a random Rydberg ensemble of $32p$ atoms using a 300ns Rydberg excitation laser pulse (produced via AOM chopping of the 480nm CW laser). The laser excites atoms from the upper MOT trap state ($5p_{3/2}$) to the $32p$ level (enabled by Stark mixing in the applied electric field) in an external field of ~12 V/cm (i.e., detuned by +0.5V/cm or +85MHz from resonance). The large initial detuning essentially turns off the resonant dipole-dipole interaction during the laser excitation. The Rydberg atoms are then exposed to detuning jump sequences featuring 0/1/2 jump cycles. In each jump cycle, pairs of Rydberg atoms are tuned +0.06/+0.09/+0.15V

/cm (+10/+15/+25MHz) from resonance for some amount of time, and then tuned to −0.06/−0.09/−0.15V/cm (−10/−15/−25MHz) for the same amount of time. For 0 jump cycles, the atoms are held at the same detuning relative to resonance for the entire duration of the allowed interaction. The total time for 0/1/2 jump sequences is scanned from 0-400ns. After the interaction time, the system is rapidly tuned +0.5V/cm off resonance again, turning off the resonant interaction, and the atoms are then ionized and, state populations measured, with SSFI.

The performance of the jump sequences introduced above has been experimentally verified through their ability to restore Rabi oscillations among atom pairs in random Rydberg gas with many atoms. Previously, because of the wide range of separations and different orientations of atoms within a Rydberg gas, dipole-dipole interaction mediated Rabi flopping between different atom pair states has not been experimentally observed in Rydberg gases consisting of more than a few atoms. To our best knowledge, with the help of jump sequences, we have made the first observation of Rabi flopping in random dipole-dipole coupled systems with more than a few atoms. The effect of the jump sequences on the coupled atom population dynamics has been explored as a function of both Rydberg density (Figures 4.2, 4.3) and jump detuning (Figures 4.4, 4.5).

For each detuning and density combination, the p state population (normalized to the total Rydberg population) is measured as a function of time after an ensemble of initially excited p atoms is tuned on resonance, held at a constant detuning from resonance, or subject to 1 (magenta) or 2 (yellow)

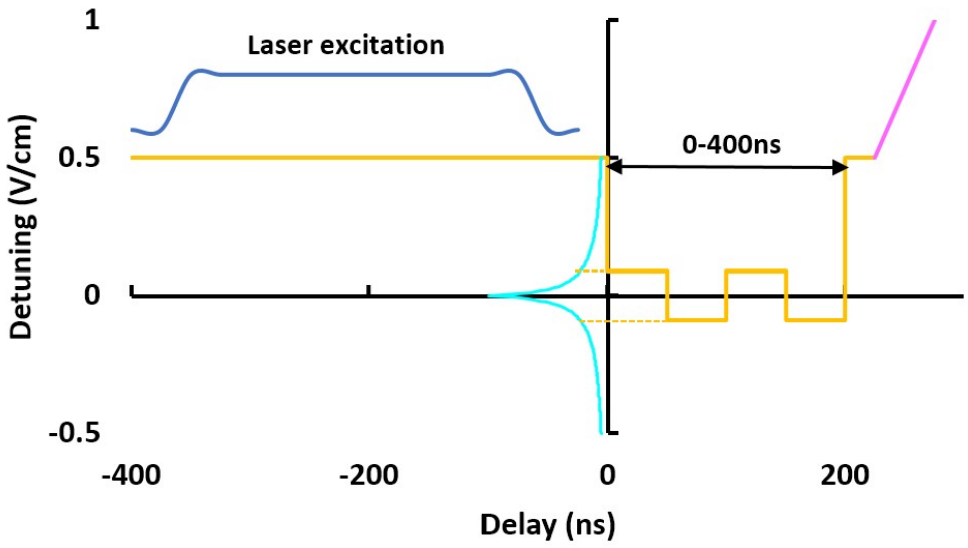

Figure 4.1: Voltage across the field plates as a function of time during a jump experiment, determined by voltages applied to both the front plate (connected to AWG, yellow) and back plate (connected to trigger transformer for SSFI, magenta). The AOM chopped blue laser pulse (blue) creates a Rydberg gas via Stark assisted excitation of $5p$ atoms to the $32p$ state while the pp to ss' interaction is tuned far (~85MHz) from resonance. In the example illustrated, voltage pulses from the AWG then tune the system about the resonance (shown are 2 detuning jump cycles at $\pm$0.09V/cm (corresponding to relative energy shifts of $\pm$15MHz) for a total interaction time of 200ns). The resonance lineshape (or interaction strength) in the relevant fields is shown in cyan. After the control pulse sequence, the atoms are ionized and populations in different Rydberg states measured via SSFI.

jump cycles. During each experimental scan of delay time, the apparatus takes 80 measurements of p population at $t = 0$, and 10 measurements at each delay, from 4-400ns with 4ns time steps. Additionally, to reduce noise, the oscilloscope recording the data is set to output the average of the previous 16 data traces, instead of the current trace. Therefore, the recorded signal at each delay step is a weighted average of the current step (5/8ths) and the previous step (3/8ths). Five scans are performed and averaged for each measurement type.

While the TOF signal corresponding to pure p state population can be recovered from the $t = 0$ data, the TOF signal corresponding to zero p state population cannot be accurately determined experimentally, due to some overlap of the s' and p signals in the TOF signal. Therefore, to compare the delay dependent population transfer measurements to simulations, a single constant is used to normalize the measured p state population for the on resonance case to the simulation results. That same constant is then used to normalize the no jump and jump sequence data as well.

As shown in Figures 4.2 and 4.4, the experimental and simulation results are generally in good agreement, especially at low densities and high detunings, given the experimental noise. Quantitatively, the dephasing time as a function of density or detuning is not easily extracted from the measurements due to the rapid decay of the Rabi oscillations, and experimental noise (more discussion in chapter 5). Qualitatively, the frequency of the observed Rabi oscillations reduces by roughly a factor of $2\mathcal{N}$ as jump number increases, as the theoretical model predicts. The amplitude of the population transfer increases as detuning

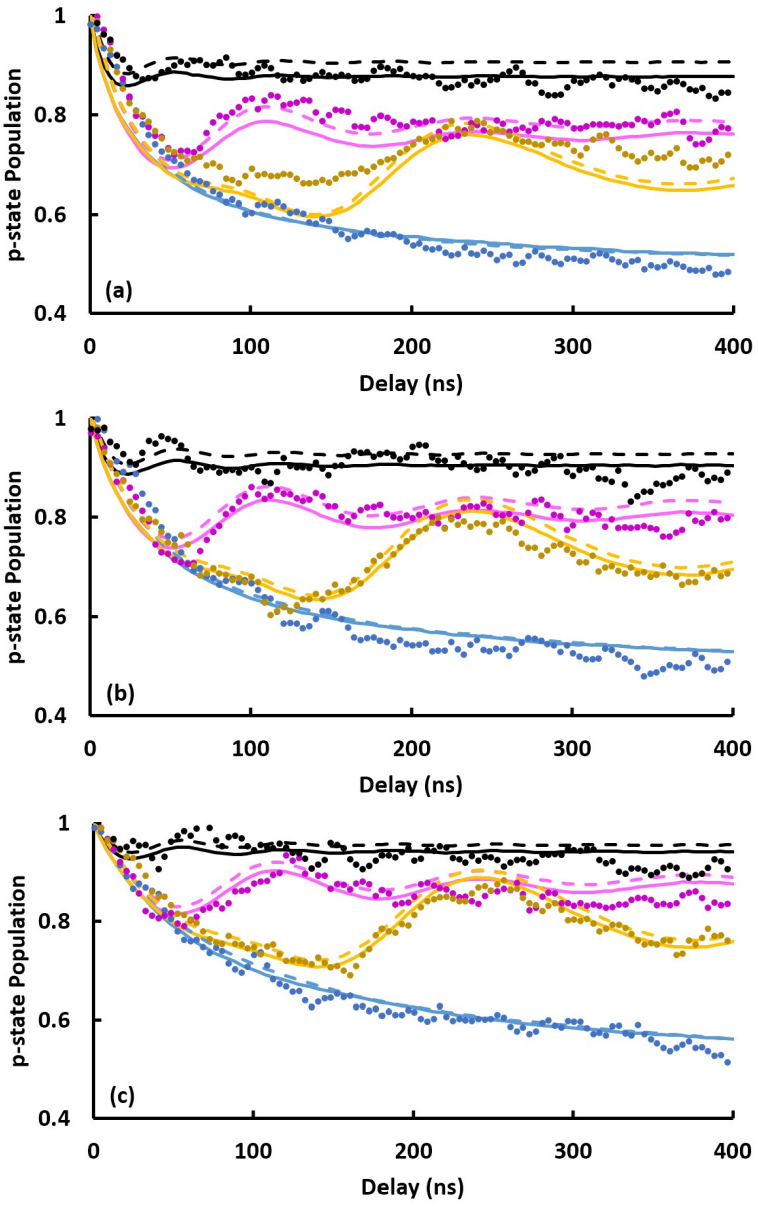

Figure 4.2: Experimental data (dots) and simulation results based on 4-atom group ensembles considering Gaussian distribution of density and considering (lines)/not considering (dashed lines) Rydberg blockade for p state population (normalized to the total Rydberg population) as a function of time after an ensemble of initially excited p atoms with peak Rydberg density of (a)~$3 \times 10^9/\text{cm}^3$, (b)~$2 \times 10^9/\text{cm}^3$, and (c)~$1 \times 10^9/\text{cm}^3$ is tuned on resonance (blue) or +15MHz (black) on the positive field side of resonance for $t > 0$, or subject to 1 (magenta) or 2 (yellow) jump cycles at detunings of $\pm$15MHz.

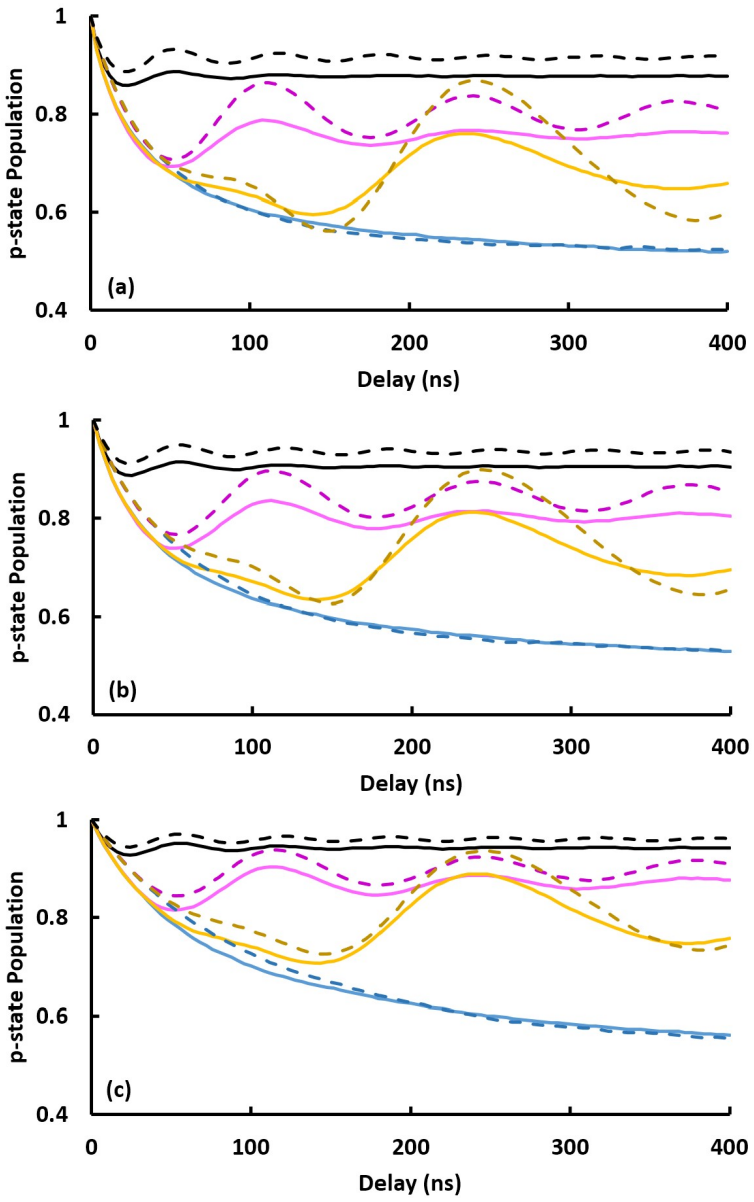

Figure 4.3: Simulation results based on 4-atom group ensembles (lines, considering Gaussian distribution of density) or 2-atom group ensembles (dashed lines, considering Gaussian distribution of density), not including Rydberg blockade effects, for p state population (normalized to the total Rydberg population) as a function of time after an ensemble of initially excited p atoms with peak Rydberg density of (a)~$3\times10^9/\text{cm}^3$, (b)~$2\times10^9/\text{cm}^3$, and (c)~$1\times10^9/\text{cm}^3$ is tuned on resonance (blue) or +15MHz (black) on the positive field side of resonance for $t > 0$, or subject to 1 (magenta) or 2 (yellow) jump cycles at detunings of $\pm$15MHz.

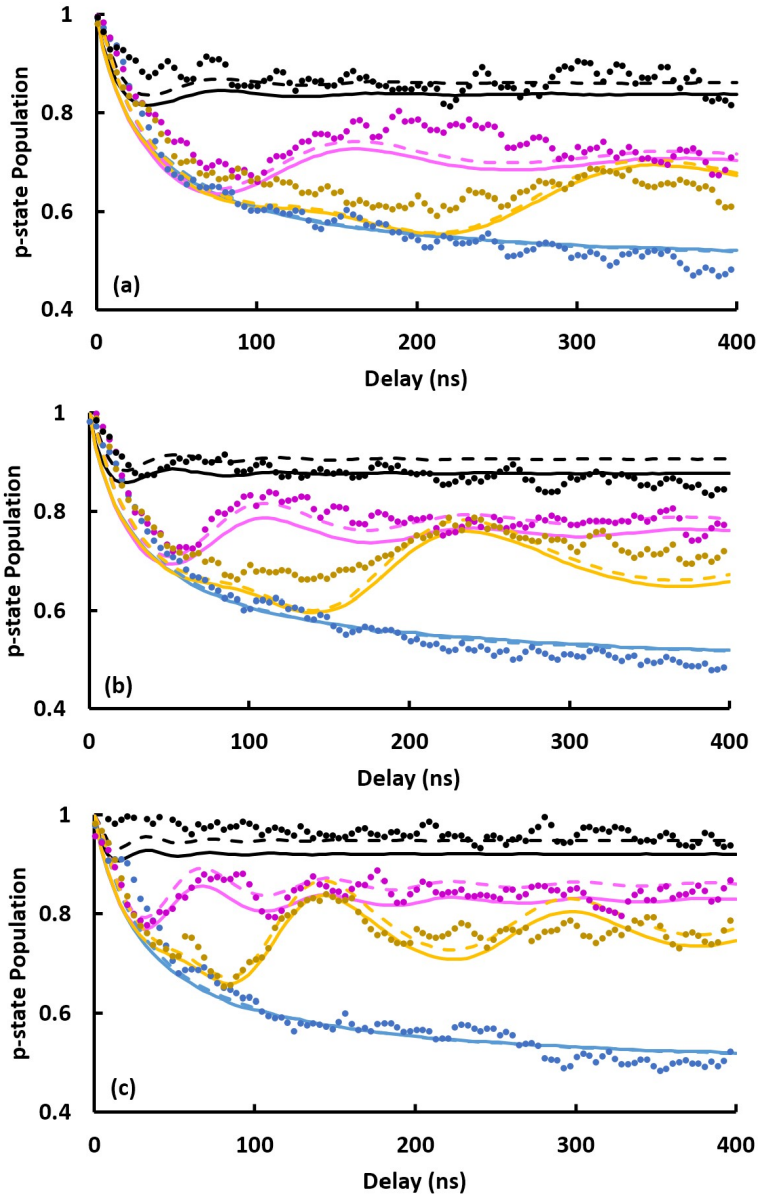

Figure 4.4: Experimental data (dots) and simulation results based on 4-atom group ensembles considering Gaussian distribution of density, considering (lines)/not considering (dashed lines) Rydberg blockade, for p state population (normalized to the total Rydberg population) as a function of time after an ensemble of initially excited p atoms with peak Rydberg density of $\sim 3 \times 10^9/\text{cm}^3$ is tuned on resonance (blue), or to (a)+10MHz, (b)+15MHz, and (c)+25MHz (black) on the positive field side of resonance for $t > 0$, or subject to 1 (magenta) or 2 (yellow) jump cycles at detunings of (a)$\pm$10MHz, (b)$\pm$15MHz, and (c)$\pm$25MHz.

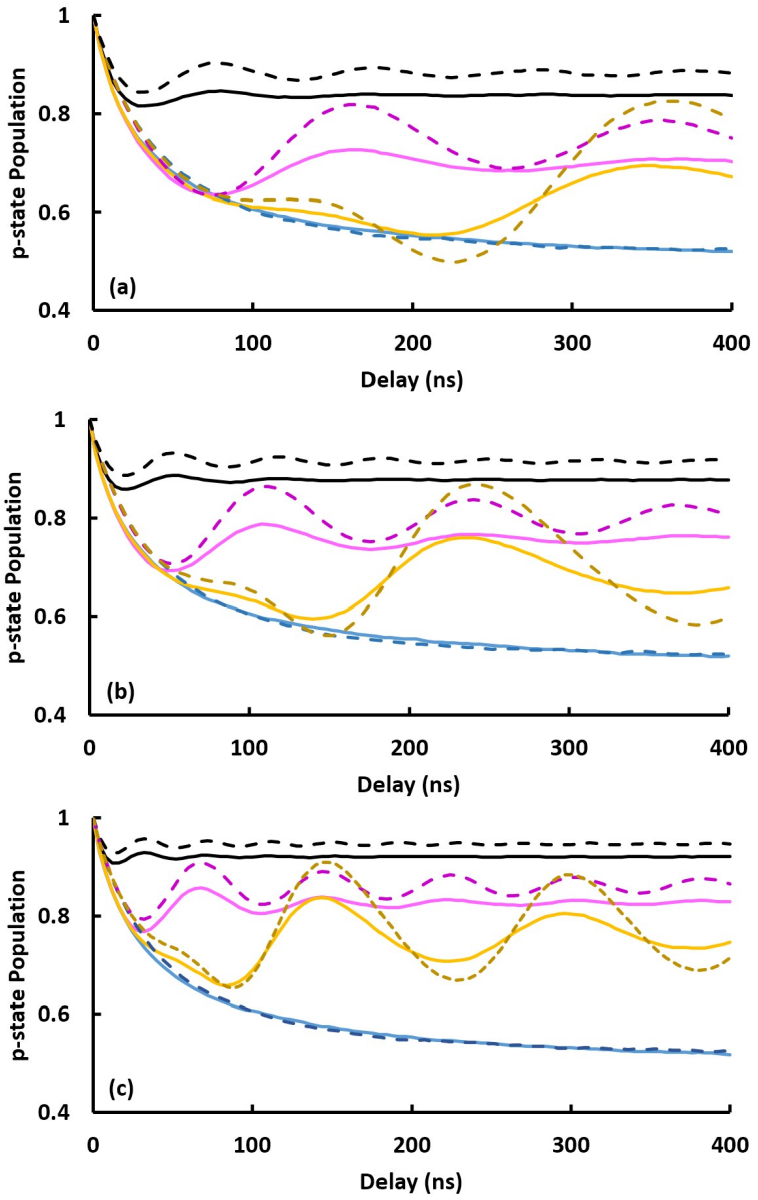

Figure 4.5: Simulation results based on 4-atom group ensembles (lines, considering Gaussian distribution of density) or 2-atom group ensembles (dashed-lines, considering Gaussian distribution of density), not including Rydberg blockade effects, for p state population (normalized to total population) as a function of time after an ensemble of initially excited p atoms with peak Rydberg density of $\sim 3 \times 10^9/\text{cm}^3$ is tuned on resonance (blue), or to (a)+10MHz, (b)+15MHz, and (c)+25MHz (black) on the positive field side of resonance for $t > 0$, or subject to 1 (magenta) or 2 (yellow) jump cycles at detunings of (a)$\pm$10MHz, (b)$\pm$15MHz, and (c)$\pm$25MHz.

decreases or density increases, for all off resonance cases and jump cases, which is to be expected. However, the observed amplitude increase is less than the theoretically predicted value of $4\mathcal{N}^2$, because that expression assumes $\delta \gg \Omega$, and net population transfer $\ll 1$. Neither of these assumptions is rigorously met under the conditions accessible to measurements with satisfactory signal to noise.

A comparison of simulation results using 4-atom or 2-atom group ensembles (Figures 4.3 and 4.5) showcases the impact of beyond nearest neighbor interactions, e.g., excitation hopping effects, on the Rydberg gas dynamics [5, 30, 31, 33, 70, 71, 75, 76, 77, 78, 79, 80, 81, 82, 83, 84, 85, 86, 87]. While good agreement between experiment and simulation results based on both 4-atom and 2-atom group ensembles for the population dynamics in the *on resonance* case (see chapter 3), for the off resonance cases, the experimental data and different simulation models show noticeable differences in the Rabi oscillation amplitude and decay time. In particular, the faster decay of the Rabi oscillations in the experiment and 4 atom simulations suggests that beyond nearest neighbor effects are more important for off resonance conditions. Chapter 5 includes a more detailed exploration of excitation hopping, particularly in the off-resonance case, and how hopping affects the population transfer properties within the Rydberg ensemble.

4.3 Experimental Imperfections and Their Effects

While the experiments are designed to implement the theoretical detuning jump sequences, there are a few notable imperfections. One is that the initial laser excitation of the Rydberg atoms does not produce a pure p state ensemble. With a detuning field of only +0.5V/cm (rather than infinity), the coupling between pp and ss' atom pairs is not zero. Therefore, the eigenstate which the laser excites at detuning field of +0.5V/cm is actually a coherent mixture of pp and ss', rather than pure p. As a result, the maximum possible ss' population after projecting to the positive side of resonance is slightly larger than on the negative side of resonance at the same detuning. Accordingly, there is an asymmetry when the jump sequences are performed. To check how much this affects the overall performance of the jump sequences in terms of revealing Rabi oscillations in the population transfer, simulations have been performed at a Rydberg atom density of $3 \times 10^9/\text{cm}^3$, computing the population transfer to ss' after 0,1,2 jumps and a detuning of $\pm$25MHz. These conditions match those of the measurements in which the effects of non-infinite initial detuning are expected to be largest.

Figure 4.6 compares the results of simulations in which the system is initially prepared as an ensemble of pure p state (i.e., infinitely far from resonance) to the experimental case in which the Stark eigenstates are initially excited at a field +0.5V/cm off resonance. The simulation results show that the finite initial detuning results in somewhat different long-term populations

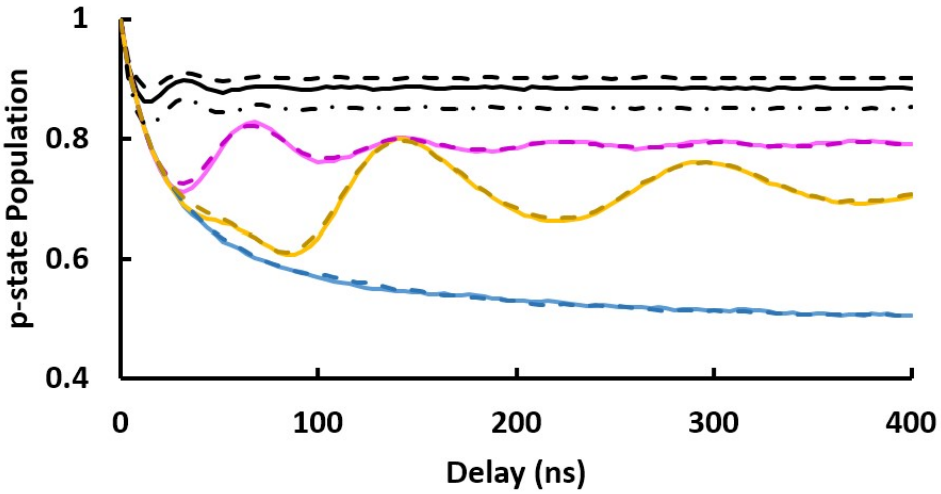

Figure 4.6: Simulation results based on 4-atom group ensembles of population in p state (normalized to total population) as a function of time when a Rydberg ensemble at density of $3 \times 10^9/\text{cm}^3$ is tuned on-resonance (blue) or subject to 1 (magenta) or 2 (yellow) jumps at detunings of $\pm$25MHz, starting from a pure p state population (solid lines) or starting from the nominal pp eigenstate +0.5V/cm off resonance (dashed lines). The black curves show the results when the system is tuned to one side of resonance (+/−25MHz) starting from a pure p state (solid black) or from the pp eigenstate at +0.5V/cm off resonance (black dash/black dash dot).

at positive and negative detunings for the no jump case (i.e., when the system is left on one side of resonance for the entire evolution time), but has essentially no effect on the population dynamics when various jump sequences are applied.

Another experimental imperfection is that the detuning jumps are not instantaneous, but rather, subject to a switching time of ~2ns. To check that the experimental population transfer in the presence of the detuning jump sequences is dominated by the system evolution between field transitions, rather than unwanted population transfer induced during the transitions themselves,

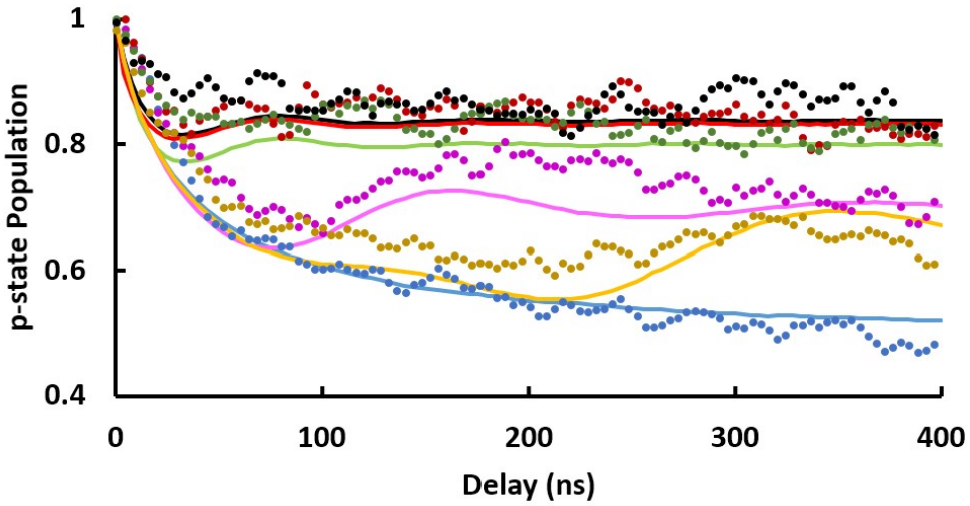

Figure 4.7: Experimental data (dots) and simulation results based on 4-atom group ensembles (lines, considering Gaussian distribution of density) showing p state population (normalized to total population) as a function of time when an ensemble of p atoms with peak Rydberg density of $\sim 3 \times 10^9/\text{cm}^3$ is tuned to dipole-dipole resonance (blue) or to $+/-10$MHz (black/green) away from resonance for $t > 0$, or subject to 1 (magenta) or 2 (yellow) time-symmetric jump cycles at detunings of ± 10MHz, or subject to single asymmetric jump (red) with the system held at $+10$MHz detuning for $t-2$ns before transitioning to -10MHz detuning for only 2ns.

measurements and simulations have also been performed using asymmetric jump sequences in which the system evolves primarily on the positive side of the resonance, spending only 2ns per jump cycle on the negative side.

Figure 4.7 shows the result for such an asymmetric sequence, featuring a detuning of $+0.06$V/cm ($+10$MHz) (to maximize population transfer and thus achieve better SNR ratio) for 0-400ns before a jump to -0.06V/cm for 2ns. As the results show, the effect of non-instantaneous jumping transitions is negligible, completely overwhelmed by experimental noise.

Despite the experimental imperfections, suppression of dephasing to the

point of achieving the first observation of Rabi flopping in random dipole-dipole coupled systems with more than a few atoms is nonetheless quite useful. With underdamped Rabi oscillations, detuning jump sequences now enable us to analyze their decay, thus providing insights into how the dephasing of the cold Rydberg atom gas ensemble behaves under different conditions, as will be discussed in chapter 5.

Chapter 5

Effects of Different Dephasing Mechanisms in Rydberg Gas Ensembles

In chapter 3, two main mechanisms of dephasing in a Rydberg gas were introduced: (1) Differences in Rabi frequencies for near resonant energy transfer within local atom groups due to the variation in atom separation and relative orientation among small groups (2 or 4 atoms) within the larger ensemble and (2) excitation hopping (sp to ps or $s'p$ to ps') between different atoms. Both mechanisms have been studied extensively in previous research [5, 31, 33, 70, 71, 75, 76, 77, 78, 79, 80, 81, 82, 83, 84, 85, 86, 87]. The consensus is that hopping does not play a major role in the dynamics if the system is tuned to a Förster resonance, i.e., on dipole-dipole coupled energy trans-

fer resonance [70, 81, 82]. This is because resonant dipole-dipole interactions shift the eigenenergies of nearest neighbor atoms substantially. Accordingly, the energies of few atom groups with excitations/de-excitations distributed differently between different atom sites are not degenerate, suppressing what have been called "always resonant" exchange interactions. In the time-domain, the excitation hopping between nearest neighbors is suppressed by the rapid Rabi cycling between nearest neighbors [70, 85]. This conclusion is also supported by the results of the simulations described in chapter 3. On the other hand, in the far off resonance case, strong resonant nearest neighbor interactions are essentially turned off. Thus, hopping is the dominant interaction [71, 78, 79, 80, 84, 86], and the dominant mechanism for dephasing. Although some previous studies have considered how the hopping interaction changes the resonant energy transfer lineshape [31, 75, 81, 82], the dynamics of systems in the intermediate regime where atoms are neither on, nor very far off, resonance (and, therefore, are exposed to both mechanisms), remain largely unexplored beyond theoretical acknowledgement that both mechanisms play a role in this regime [33, 75, 76, 77].

This chapter quantitatively explores how the relative importance of the two dephasing mechanisms evolves as the detuning and/or density changes. This is achieved by analyzing the dephasing properties of a system subject only to mechanism (1) through simulations based on 2 atom group ensembles, subject to mechanism (1) and limited effects of mechanism (2) through simulations based on 4 atom group ensembles, and experiments subject to both (1) and (2), (as well as other processes that are assumed to play only a minor role under

our experimental conditions, e.g., spontaneous emission, atom motion etc.) Beyond exploring the dephasing properties of near resonance Rabi oscillations and "amplified" near resonance Rabi oscillation with detuning jumps, this chapter will also examine the use of Ramsey interference experiments and simulations to characterize dephasing in the far off resonance regime.

5.1 Extracting Dephasing Properties from Rabi Oscillations

Dephasing in the vicinity of the energy transfer resonance can be characterized through the decay of the Rabi oscillations observed in time-domain measurements, or through the width of the Rabi frequency peak in the Fourier transform of time domain data and simulations. With a discrete Fourier transform (e.g., FFT) the resolution of the frequency spectrum is determined by the inverse of the maximum measurement or simulation time. For example, data extending to 1μs will have a frequency resolution of 1MHz. Extending measurements/simulations to longer times will provides better frequency resolution, but a frequency resolution much better than the width of the Rabi peak does not convey significant additional information, and there are practical limitations to the maximum observation time in experiments and simulations. For experiments, spontaneous decay and atom motion need to be taken into consideration at longer evolution times, which could otherwise both be ignored in the context of short evolution times. For simulations, the temporal sampling rate must be high enough to reconstruct the oscillations (in our case

500MHz for off resonance case and 250MHz for 1 jump case) and extending the simulation time while meeting the requirement of high temporal sampling rate is limited by available computational time and resources.

For ease of comparison of FFT spectra, "zero padding" of the time domain data to longer times can be used. As illustrated in Figure 5.1, this increases the density of points in the frequency spectrum without increasing the actual resolution of the measurement/simulation, the latter determined by the maximum system observation time (prior to zero padding).

To accurately extract the frequency spectrum, the simulations of p population as a function of time in this chapter are performed at a 500MHz temporal sampling rate and extend to a maximum observation time of 4μs for off resonance cases, or a 250MHz temporal sampling rate extending to 8μs for the 1 jump cases. The frequency spectra for the 2 jump cases are not considered due to the kinks of population transfer at early evolution times, which alters the frequency spectrum profile, prohibiting accurate analysis of dephasing properties. Experimental data for the 0/1 jump cases was taken at a 250MHz temporal sampling rate with a maximum observation time of 400ns. The data are zero padded to 800ns prior to Fourier transforming.

5.2 Dephasing Properties of Near Resonance Rabi Oscillations

In chapter 4, the effects of dephasing are qualitatively shown in comparisons of the p population evolution observed in experiments and calculated in sim-

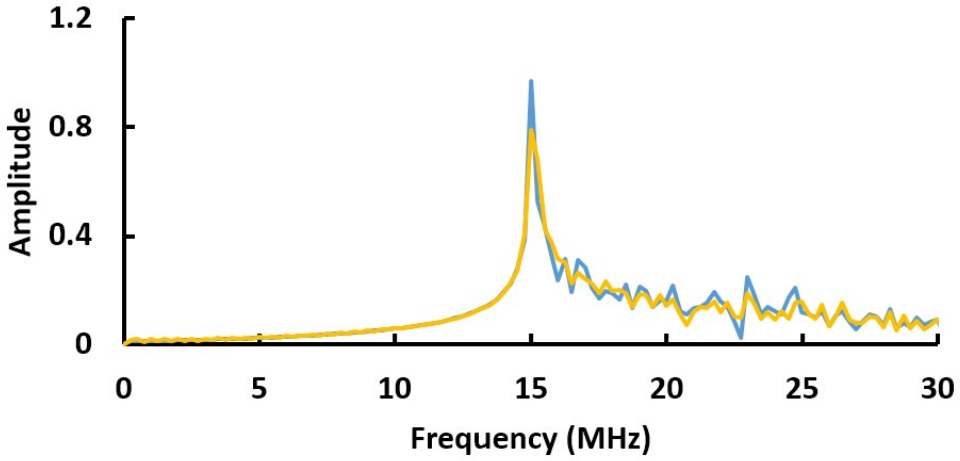

Figure 5.1: Frequency spectra extracted from simulation data based on 2-atom group ensembles for p state population as a function of time extending to 4μs (blue) or 2μs then zero padded to 4μs (yellow) after an ensemble of initially excited p atoms with Rydberg density of $0.5 \times 10^9/\text{cm}^3$ is tuned +15MHz from resonance. The temporal sampling rate is 500MHz in both cases. Note the frequency peak is less sharp in the padded case, illustrating the fact that when zero padding is used, the resolution is limited to the maximum observation time, not the density of points in the spectrum.

ulations based on 4/2-atom group ensembles (see Figures 4.2, 4.3, 4.4, 4.5). Here, to better explore the problem, the frequency spectra describing the system evolution, under the various scenarios discussed in chapter 4 (different density, different detuning, experiment/simulation with different models) are extracted and compared (see Figures 5.2, 5.3, 5.4, 5.5, 5.6, 5.7, 5.8, 5.9).

All the frequency spectra indicate that as more excitation hopping is allowed to take place (moving from simulated 2-atom group ensembles, to simulated 4-atom group ensembles, to actual experimental conditions), the width of the Rabi peak noticeably grows, suggesting that the hopping effect is a non-negligible contributor to dephasing in near resonance energy transfer processes. It is also notable that the frequency spectra obtained for the 1 jump control sequences very closely resembles a scaled version of the frequency spectrum obtained when the system is tuned to one side of the resonance. With the 1 jump sequence, the peak spectral amplitude is increased by a factor of four and the Rabi frequency is divided by a factor of two, precisely as equation 4.4 predicts.

Figures 5.2, 5.3, 5.4, 5.5 show that as the Rydberg density increases, the Rabi peak broadens, indicating faster dephasing, as expected. The experimental spectra for the 0 jump case (Figure 5.2) do not have sufficient signal to noise to make a meaningful comparison. The 1 jump measurements show a clear increase in the width of the Rabi peak with increasing density, but the signal to noise precludes a quantitative determination of the density dependence. A more detailed analysis can be made for the simulations. With increasing density, the changes in the widths of the peaks for the 4-atom group ensembles are

not significantly different from those for the 2-atom group ensembles. In the 0 jump cases, the FWHM of the Rabi peak is roughly 2.7MHz, 1.8MHz, 0.8MHz (3.4 : 2.2 : 1) for densities of $3\times10^9/\text{cm}^3$, $2\times10^9/\text{cm}^3$, $1\times10^9\text{cm}^3$ respectively in the 2-atom groups based simulations, or 21.5MHz, 16.7MHz, 7.5MHz (2.9 : 2.2 : 1) for the same densities, respectively, in 4-atom groups based simulations, indicating that: (1) the relative impact of hopping (which cannot occur in the 2-atom groups based simulations) is independent of density, and (2) the dephasing rate increases in proportion to the density.

Figures 5.6, 5.7, 5.8, 5.9 show experimental and simulated Rabi spectra at constant density but different detunings. The signal to noise in the experimental spectra is, again, insufficient for a quantitative analysis. However, we can extract additional physics from the simulations. The simulations based on 2-atom group ensembles (Figures 5.8(b) and 5.9(b)), show a very small decrease or no change in the width of the Rabi peak for the 0 jump or 1 jump scenarios with increasing detuning, respectively. In contrast, simulations based on 4-atom group ensembles (Figures 5.8(a) and 5.9(a)), show a slight increase in the width of Rabi peak with increasing detuning. This indicates that dephasing via excitation hopping becomes more important as detuning increases. This is consistent with the conclusions of previous research in the extreme on and off resonant cases, and provides new results connecting the two regimes. The effects of hopping can be largely ignored for on resonance population transfer [70, 81, 82, 85] but hopping gradually becomes the dominating factor in the evolution of the system as resonant energy transfer turns off with increasing detuning [71, 78, 79, 80, 84].

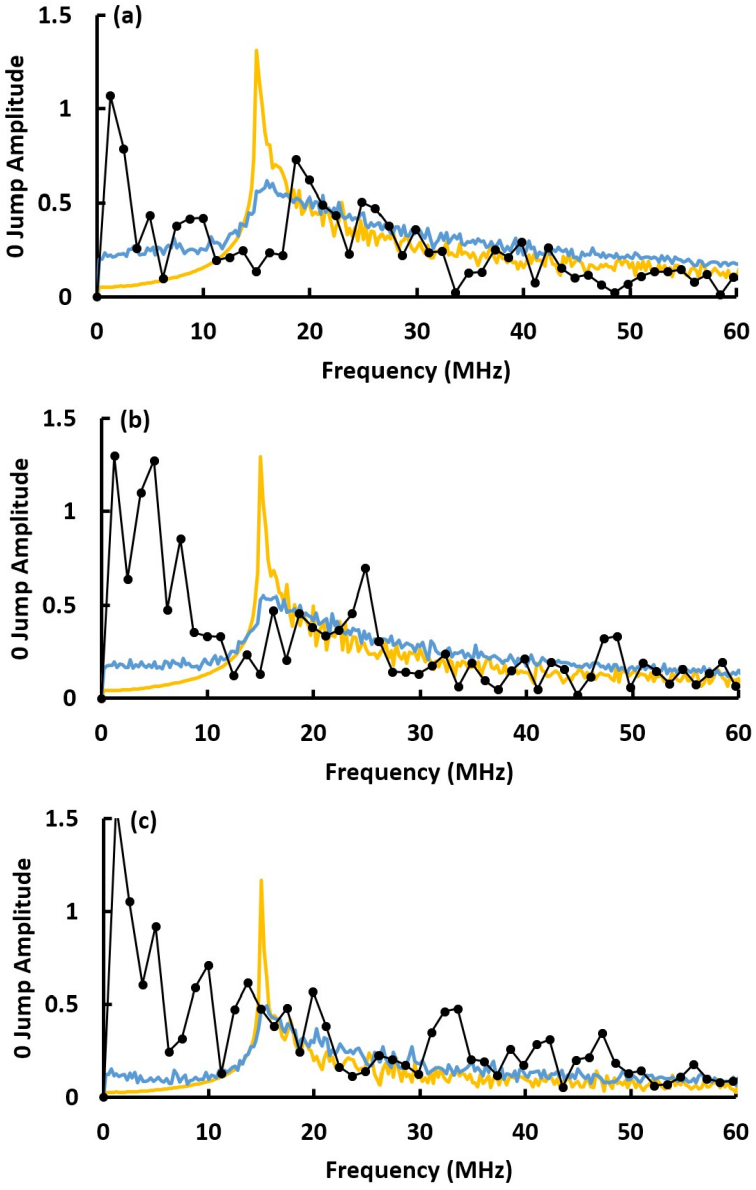

Figure 5.2: Frequency spectra extracted from experimental data (black) or simulations based on 4-atom group ensembles (blue, including Gaussian distribution of density) or 2-atom group ensembles (yellow, including Gaussian distribution of density) for p state population (normalized to total population) as a function of time after an ensemble of initially excited p atoms with peak Rydberg density of (a)~$3 \times 10^9/\text{cm}^3$, (b)~$2 \times 10^9/\text{cm}^3$, and (c)~$1 \times 10^9/\text{cm}^3$ is tuned +15MHz on the positive field side of resonance.

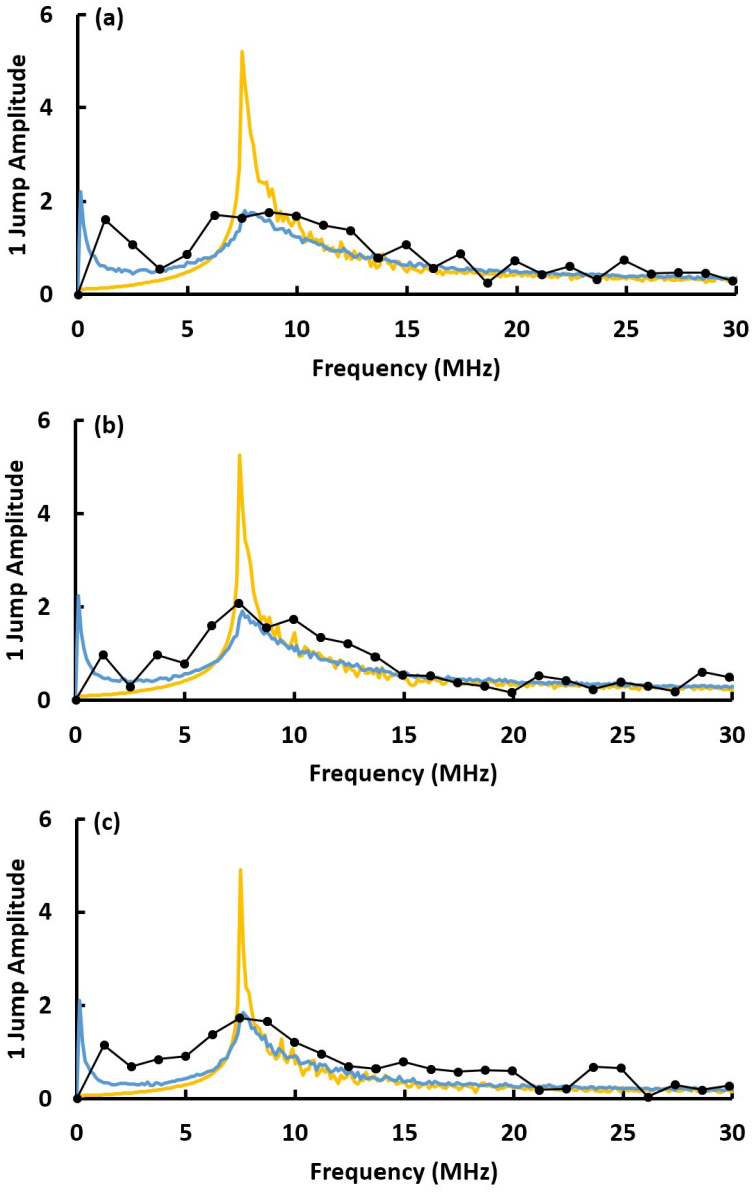

Figure 5.3: Frequency spectra extracted from experimental data (black) or simulations based on 4-atom group ensembles (blue, including Gaussian distribution of density) or 2-atom group ensembles (yellow, including Gaussian distribution of density) for p state population (normalized to total population) as a function of time after an ensemble of initially excited p atoms with peak Rydberg density of (a)~$3 \times 10^9/\text{cm}^3$, (b)~$2 \times 10^9/\text{cm}^3$, and (c)~$1 \times 10^9/\text{cm}^3$ is subject to 1 jump cycle at detunings of $\pm$15MHz.

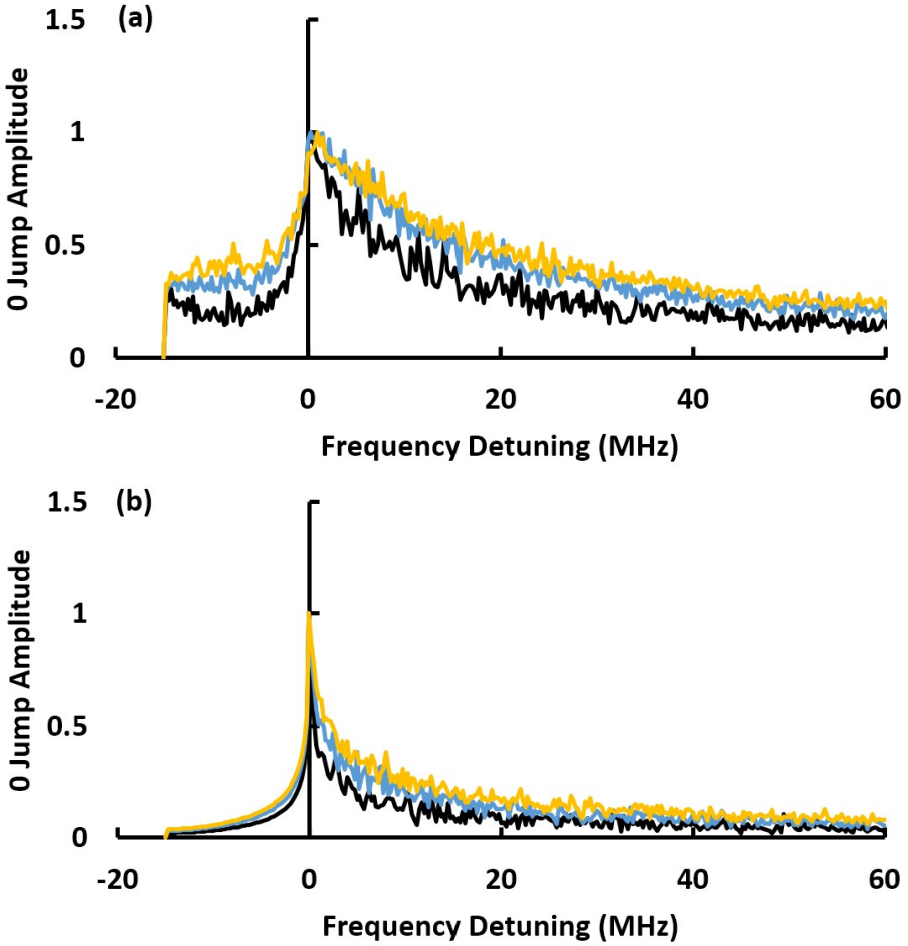

Figure 5.4: Frequency spectra extracted from simulations based on (a) 4-atom group ensembles (including Gaussian distribution of density) or (b) 2-atom group ensembles (including Gaussian distribution of density) for p state population as a function of time after an ensemble of initially excited p atoms with peak Rydberg density of $\sim 3 \times 10^9/\text{cm}^3$ (yellow), $\sim 2 \times 10^9/\text{cm}^3$ (blue), and $\sim 1 \times 10^9/\text{cm}^3$ (black) is tuned +15MHz on the positive field side of resonance. The frequency amplitudes in the different scenarios are normalized to the maximum frequency amplitude in each scenario, and the frequency scale is relative to the detuning, 15MHz in this case.

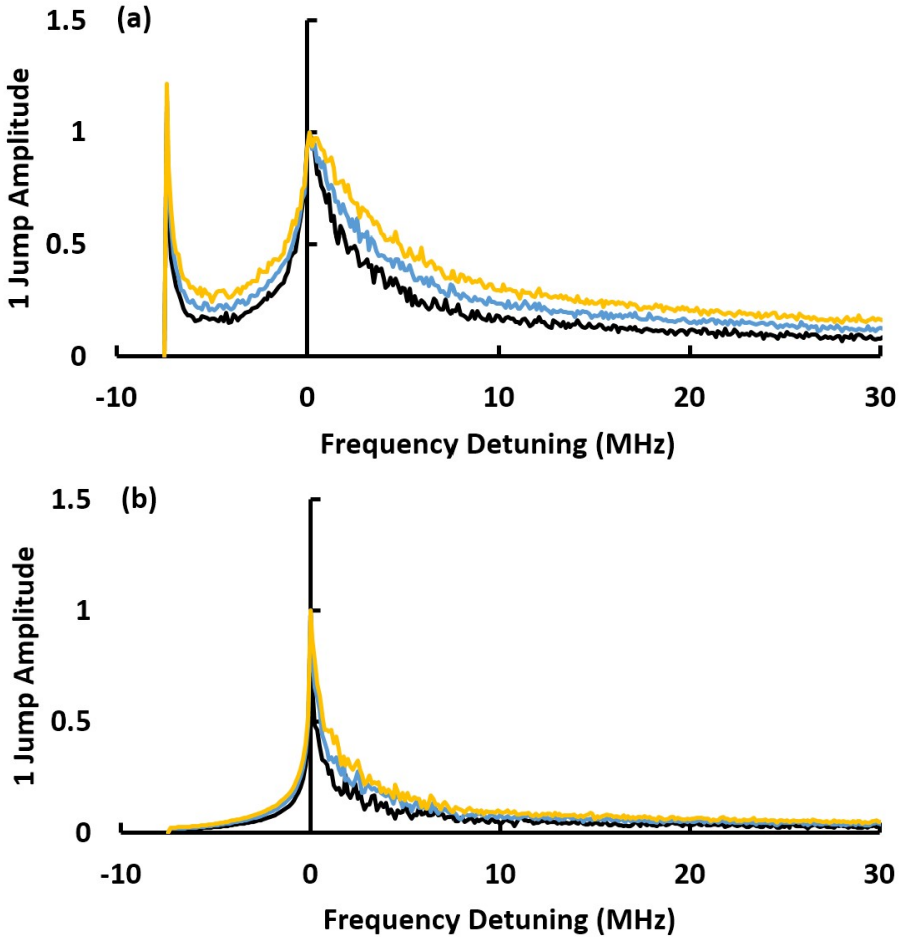

Figure 5.5: Frequency spectra extracted from simulations based on (a) 4-atom group ensembles (including Gaussian distribution of density) or (b) 2-atom group ensembles (including Gaussian distribution of density) for p state population as a function of time after an ensemble of initially excited p atoms with peak Rydberg density of $\sim 3 \times 10^9/\text{cm}^3$ (yellow), $\sim 2 \times 10^9/\text{cm}^3$ (blue), and $\sim 1 \times 10^9/\text{cm}^3$ (black) is subject to 1 jump cycle at detunings of $\pm$15MHz. The frequency amplitudes in the different scenarios are normalized to the maximum frequency amplitude in each scenario, and the frequency scale is relative to the detuning, 15MHz in this case.

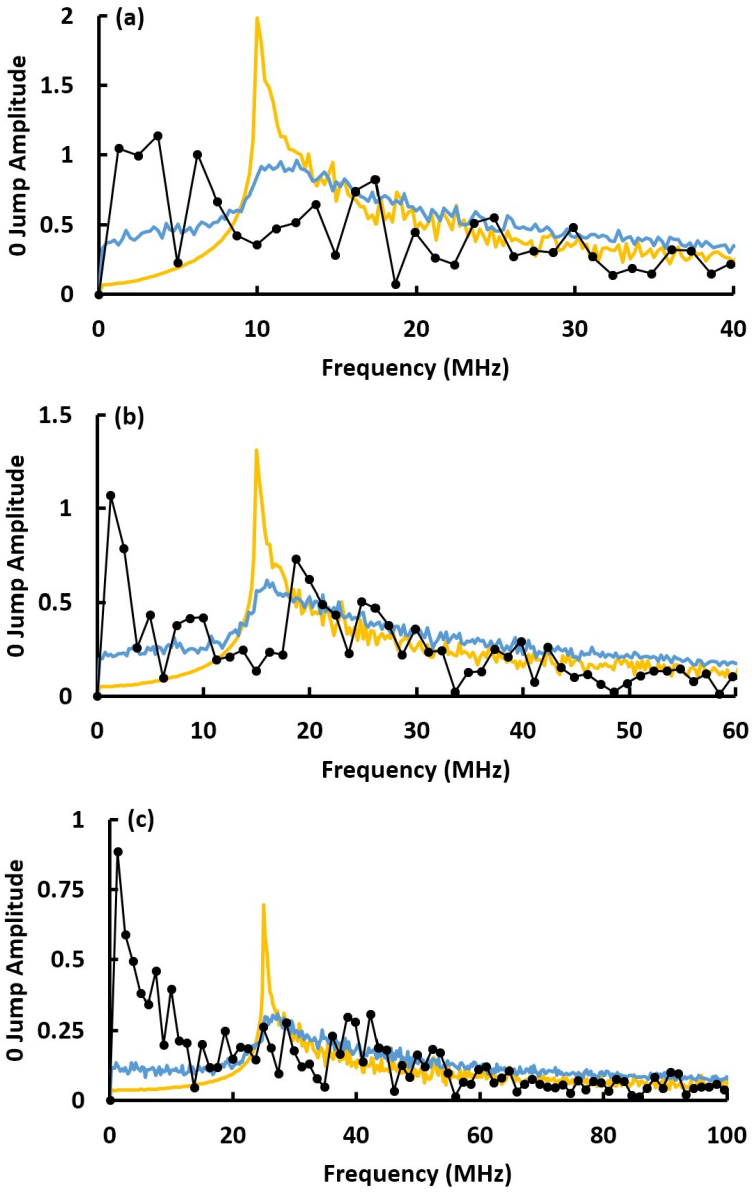

Figure 5.6: Frequency spectra extracted from measurements (black) or simulations based on 4-atom group ensembles (blue, including Gaussian distribution of density) or 2-atom group ensembles (yellow, including Gaussian distribution of density) for p state population (normalized to total population) as a function of time after an ensemble of initially excited p atoms with peak Rydberg density of $\sim 3 \times 10^9/\text{cm}^3$ is tuned (a) +10MHz, (b) +15MHz or (c) +25MHz from resonance.

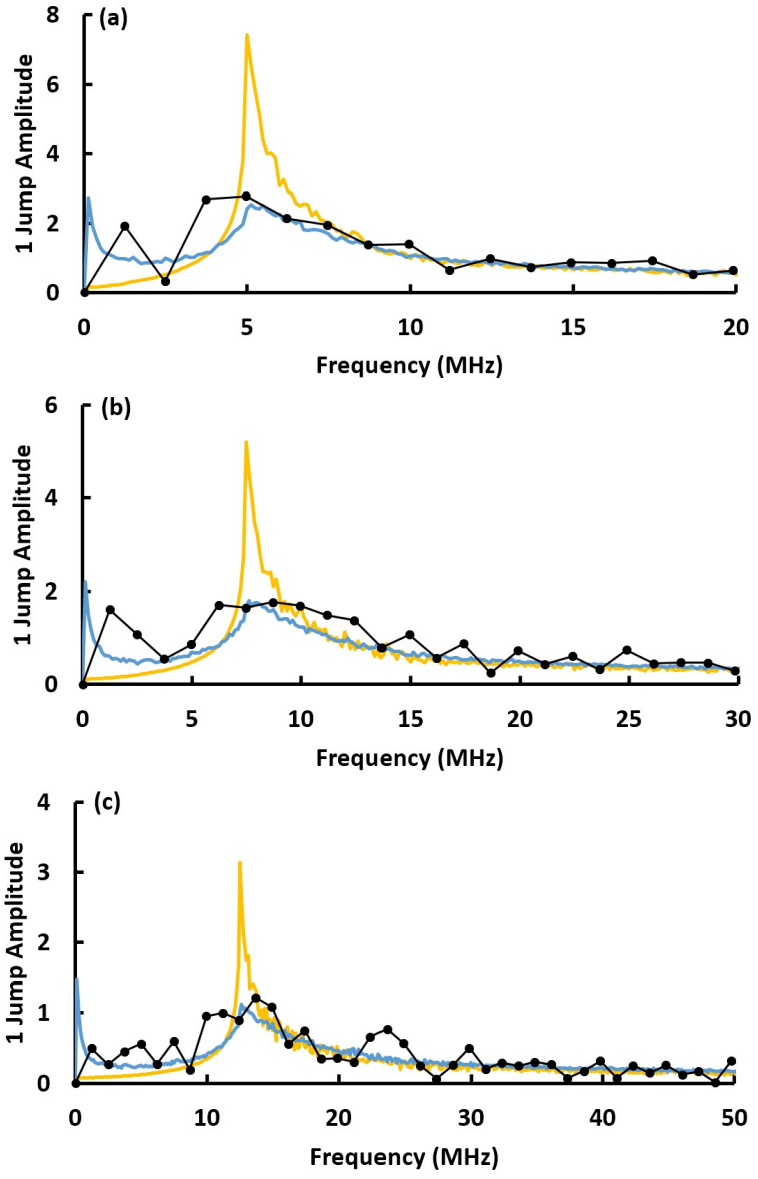

Figure 5.7: Frequency spectra extracted from measurements (black) or simulations based on 4-atom group ensembles (blue, including Gaussian distribution of density) or 2-atom group ensembles (yellow, including Gaussian distribution of density) for p state population (normalized to total population) as a function of time after an ensemble of initially excited p atoms with peak Rydberg density of $\sim 3 \times 10^9/\text{cm}^3$ is subject to 1 jump cycle at detunings of (a) $\pm$10MHz, (b) $\pm$15MHz or (c) $\pm$25MHz.

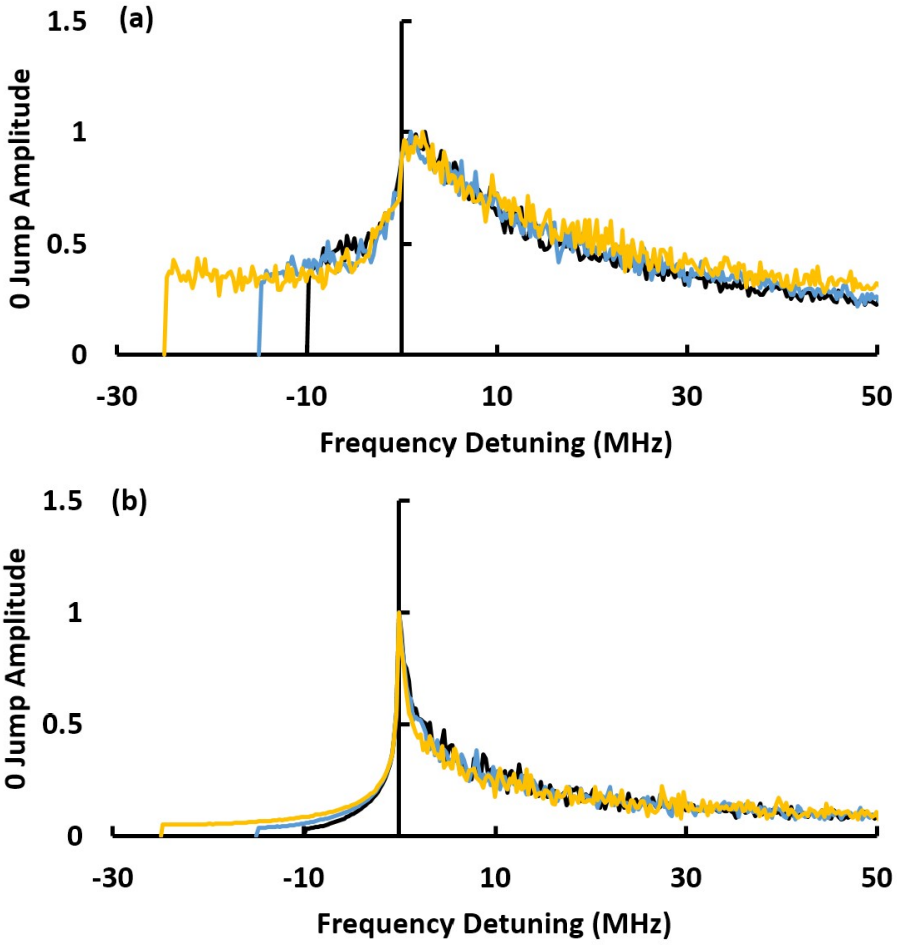

Figure 5.8: Frequency spectra extracted from simulations based on (a) 4-atom group ensembles (including Gaussian distribution of density) or (b) 2-atom group ensembles (including Gaussian distribution of density) for p state population as a function of time after an ensemble of initially excited p atoms with peak Rydberg density of $\sim 3\times 10^9/\mathrm{cm}^3$ is tuned +10MHz (black), +15MHz (blue) or +25MHz (yellow) from resonance. The frequency amplitude of the different curves are normalized to the maximum amplitude in each scenario, and the frequency scale is relative to the detuning, 10MHz (black), 15MHz (blue) and 25MHz (yellow), in each case.

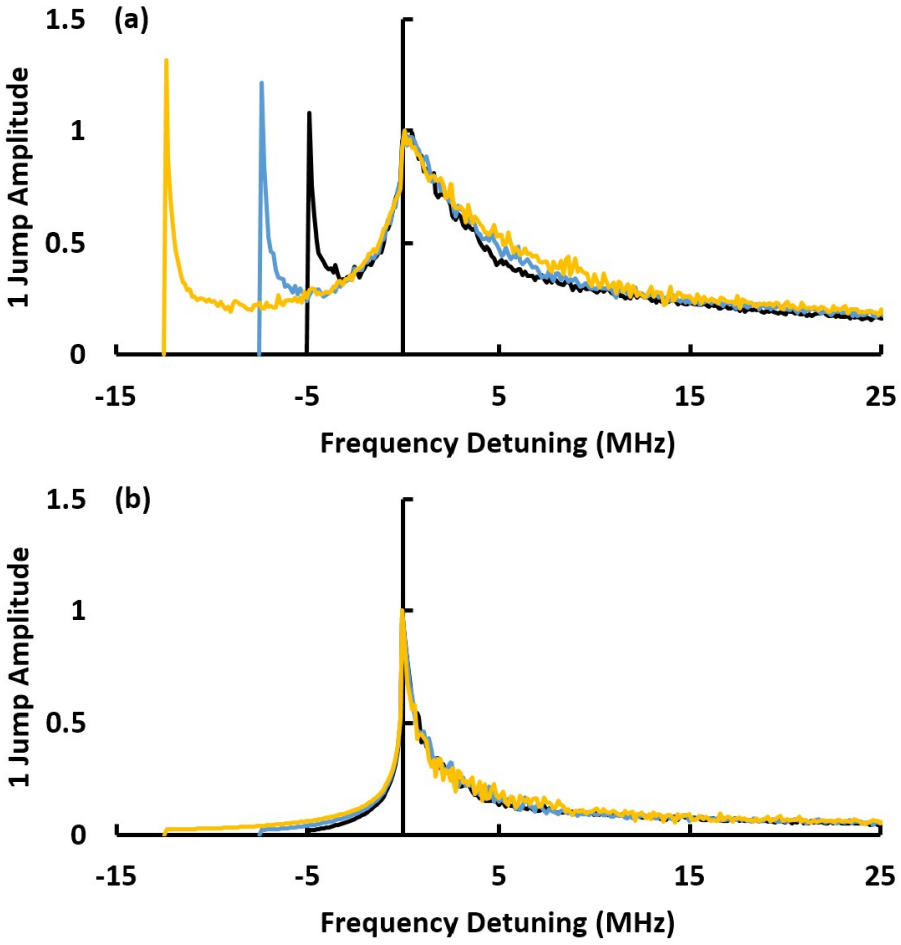

Figure 5.9: Frequency spectra extracted from simulations based on (a) 4-atom group ensembles (including Gaussian distribution of density) or (b) 2-atom group ensembles (including Gaussian distribution of density) for p state population as a function of time after an ensemble of initially excited p atoms with peak Rydberg density of $\sim 3 \times 10^9/\text{cm}^3$ is subject to 1 jump cycle at detunings of $\pm$10MHz (black), $\pm$15MHz (blue) and $\pm$25MHz (yellow). The frequency amplitude of the different curves are normalized to the maximum amplitude in each scenario, and the frequency scale is relative to the detuning, 10MHz (black), 15MHz (blue) and 25MHz (yellow), in each case.

5.3 Examining Hopping Effects with Ramsey Interference

Thus far, we have considered population transfer measurements for on resonance (chapter 3) and near resonance scenarios. To explore dephasing in the far off resonant regime, we have employed a variant of time-domain Ramsey interference spectroscopy [33], as illustrated in Figure 5.10. A random Rydberg ensemble of $32p$ atoms is first created using a 300ns Rydberg excitation laser pulse (produced via AOM chopping of the 480nm CW laser). The laser excites atoms from the upper MOT trap state ($5p_{3/2}$) to the $32p$ level (enabled by Stark mixing in the applied electric field) in an external field of ~12V/cm (i.e., detuned by +0.5V/cm or +85MHz from resonance). The large initial detuning essentially turns off the resonant dipole-dipole interaction during the laser excitation. The Rydberg atoms are tuned on resonance for 25ns, enabling a small amount of population transfer from pp to ss', and then detuned by +0.5V/cm for a variable delay time. Here the resonant pp-ss' coupling is far detuned and the superposition of pp and ss' atoms evolves under the principal influence of exchange interaction for a variable time delay. The atoms are tuned on resonance again, enabling addition population transfer between pp and ss'. The ss' amplitudes created during the two 25ns interaction intervals can interfere constructively or destructively, depending on the delay between those two intervals. After the second interaction the state populations are measured with SSFI.

Figure 5.11 shows the result of typical Ramsey interference measurements.

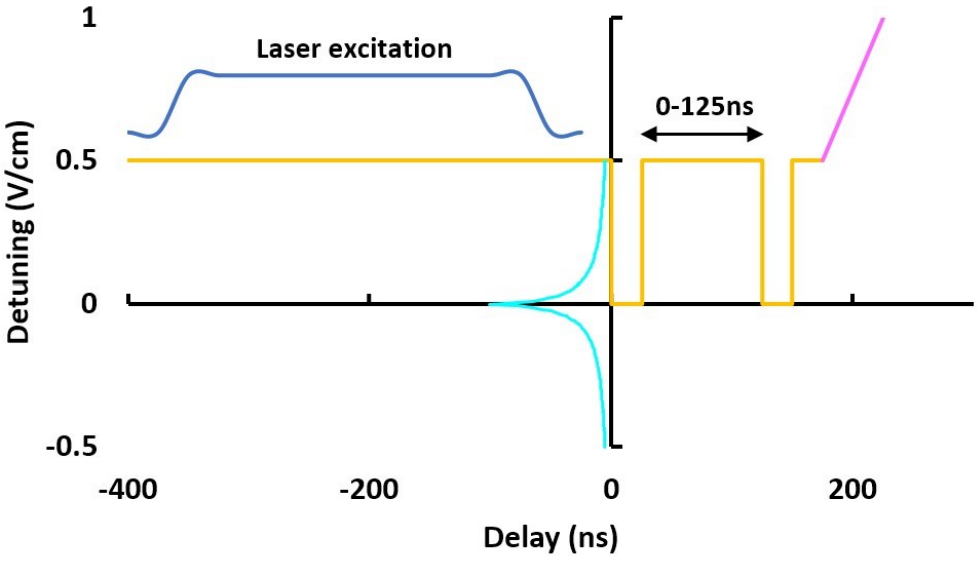

Figure 5.10: Electric field in the Rydberg interaction region as a function of time during a Ramsey interference experiment, determined by voltages applied to both the front field plate (connected to the AWG, yellow) and back field plate (connected to the high voltage trigger transformer for SSFI, magenta). The AOM chopped blue laser pulse (blue) creates a Rydberg gas via Stark assisted excitation of $5p_{3/2}$ atoms to the $32p$ state while the pp to ss' interaction is tuned far (~85MHz) from resonance. Voltage pulses from the AWG then tune the system on resonance for 25ns, before tuning the system off resonance. In our case, the off resonance detuning between the nominal pp and ss' states is ~85MHz. The off resonance time is scanned from 0-125ns (100ns shown on graph) before the system is tuned on resonance for an additional 25ns and then brought far off resonance again. The resonance lineshape (or interaction strength) in the relevant fields is shown in cyan. After the Ramsey interference sequence, the atoms are ionized and populations in different Rydberg states measured via SSFI.

The delay-dependent modulations in the p-state population reflect the ~85MHz energy separation of the nominal pp and ss' in the far detuned configuration. In the absence of beyond nearest neighbor hopping interactions, and electric field inhomogeneities, this energy splitting would be nearly identical for all atom pairs in the ensemble. In this case, any decay in the observed Ramsey interference modulations would reflect the small differences in energy splitting due to variations in the far off resonance pp-ss' coupling between nearest neighbor atoms. However, in the presence of hopping interactions, the energy splitting varies between atom pairs even when the resonant coupling is completely negligible, resulting in a dephasing of the Ramsey interference in a time that is inversely proportional to the spread in energies due to those exchange couplings.

The relatively poor agreement between the Ramsey data and the 2-atom based simulation results (which do not include hopping) in Figure 5.11, as compared to the excellent and reasonable agreement for the on or near resonance population transfer measurements respectively (see chapter 3 and 4), reflects the change in the impact of excitation hopping interactions, from negligible in the on resonance case, to primary in the Ramsey interference case. The 4-atom simulations also fail to accurately capture the rate of decay of the Ramsey interference modulations and the asymptotic baseline of the population transfer at long delays. Apparently, more than 4 atoms are coupled and larger groups of correlated atoms are required to accurately describe the few- or many-body system dynamics in this regime. The asymptotic population transfer baseline also reflects an effect of hopping that was discussed in the

context of resonance lineshapes [75, 81, 82, 85] but not unambiguously observed in population dynamics experiments: On average, more p population can be transferred to ss' pairs as the coupling strength, and hopping rate, between non-nearest neighbors, is increased. This has been explained as the result of hopping interactions that move s and s' excitations that were rapidly produced from pp atom pairs separated by less than the average atom spacing, away from those nearby atom pairs, leaving pp pairs that can rapidly convert to ss' again for a net long time gain in the number of s and s' atoms [75].

To quantitatively assess the ensemble dephasing in the far off resonance regime, we can again compute the Fourier transform of the time-domain Ramsey interference data and simulations (Figure 5.12). To accurately determine the frequency spectra, the simulations of p population as a function of delay time between the two on resonance intervals are performed with a 2GHz temporal sampling rate, and a maximum delay of 10μs. Accordingly, the spectral resolution for the simulations is 0.1MHz. The experimental data were collected at a 1GHz temporal sampling rate, and a maximum delay time of 125ns. Thus, the measurement resolution is limited to 8MHz. However, the data are zero padded to 250ns before applying the FFT to increase the number of spectral points on the peak corresponding to the Ramsey interference frequency. Additionally, unlike the main feature in the near resonance Rabi spectra, the width of the Ramsey peak is much less than its central frequency (85MHz) and the peak is reasonably symmetric. Hence, its width is fairly well characterized by it's FWHM. Therefore, we use the FWHM as a measure of the dephasing rate in the experiment and different simulation models (Table 5.1), and utilize the

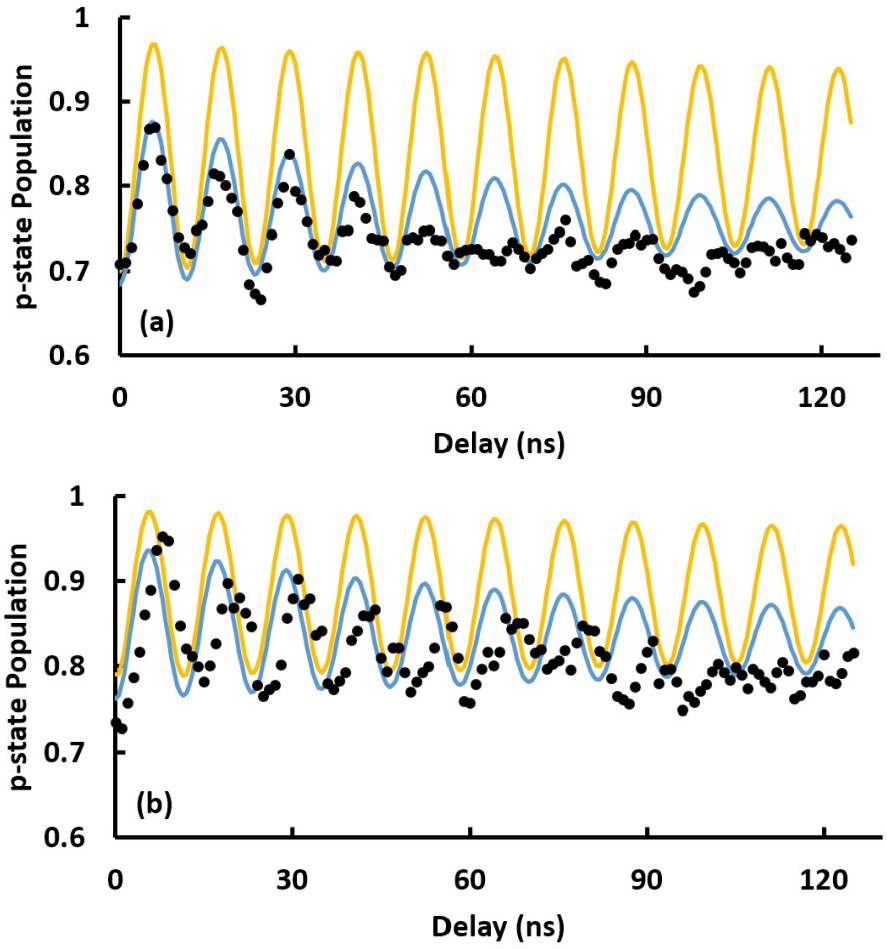

Figure 5.11: Experimental data (black) and simulation results based on 4-atom group ensembles (blue, including Gaussian distribution of density) or 2-atom group ensembles (yellow, including Gaussian distribution of density) for p state population (normalized to total population) in an ensemble of initially excited p atoms with peak Rydberg density of (a) ~$2.7\times10^9/\text{cm}^3$ or (b) ~$1.4\times10^9/\text{cm}^3$ as the delay between the two on resonance intervals in the Ramsey interference control sequence is scanned from 0-125ns.

comparison of the FWHM between different models to revisit the question of how ensemble density affects the importance of dephasing due to the exchange interactions responsible for hopping.

density(10^9/cm^3)	2.7	1.4
Experiment	~20MHz	~12MHz
4-atom group ensembles	1.4MHz	0.9MHz
2-atom group ensembles	0.5MHz	0.3MHz

Table 5.1: FWHM of Ramsey interference frequency spectra for experimental data and simulations based on 4/2-atom group ensembles at different densities. The spectral resolution is limited to 8 MHz for the experimental data and 0.1 MHz for the simulations. The contribution to the experimental width due to electric field inhomogeneity is estimated to be ~0.5MHz.

The vast differences between the frequency spectra associated with the measurements and simulations based on 4/2-atom group ensembles reflect the importance of excitation hopping in the evolution of Rydberg gases far from energy transfer resonance. Unlike the measurements on and near resonance, the 4 and 2 atom simulations clearly do not accurately capture the essential aspects of the few- to many-body physics in the far off resonance case. As Table 5.1 shows, the experimental dephasing rates reflected by the FWHM of the primary spectral peak are much larger than those predicted by the 4-atom and 2-atom simulations, respectively, indicating that the spread in the energies of coupled Rydberg atoms in the ensemble is ~40× larger than predicted if hopping interactions are ignored, and ~14× larger than expected if hopping is only allowed within 4-atom groups. Note that inhomogeneous broadening effects due to electric field inhomogeneities are estimated to be ~0.5MHz, essentially negligible when compared to the measured widths.

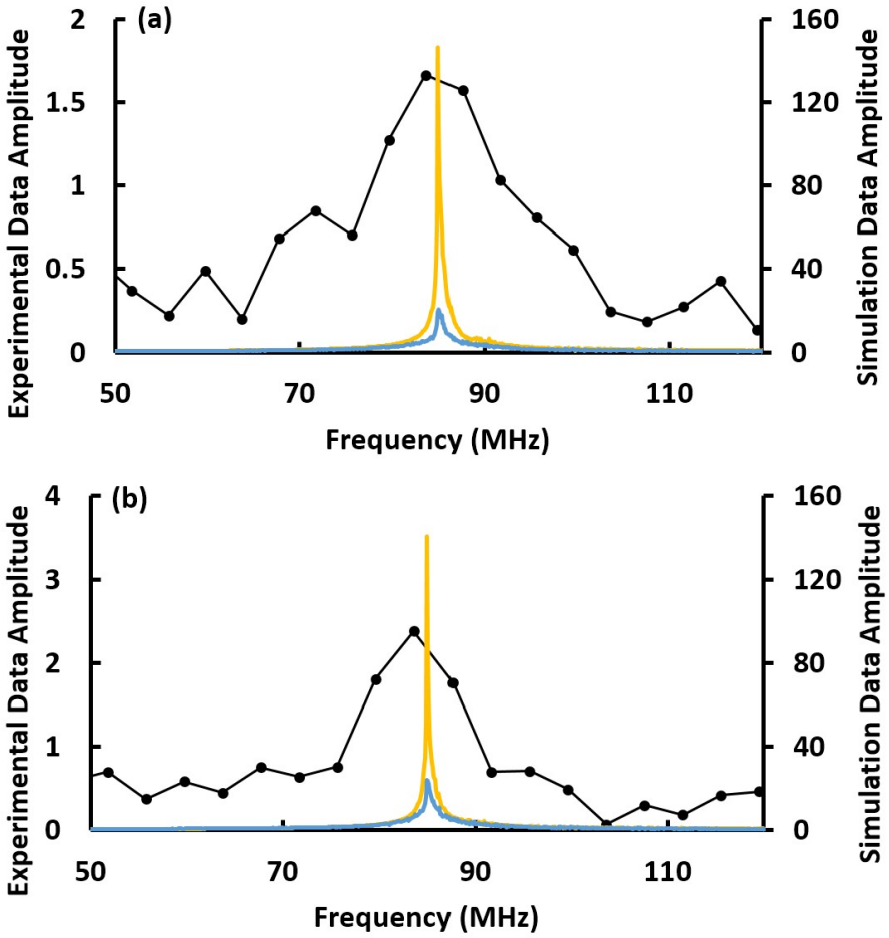

Figure 5.12: Frequency spectra extracted from experimental results (black) and simulations based on 4-atom group ensembles (blue, including Gaussian distribution of density) or 2-atom group ensembles (yellow, including Gaussian distribution of density) for p state population (normalized to total population) in an ensemble of initially excited p atoms with peak Rydberg density of (a) ~$2.7 \times 10^9/\text{cm}^3$ or (b) ~$1.4 \times 10^9/\text{cm}^3$ as the delay between two on resonance pulses in Ramsey interference is scanned. The spectral resolution is 8MHz for the experimental data and 0.1MHz for the simulations.

Interestingly, the dephasing rates for the experiment and both simulations increase by a factor of ~1.6 for a density increase of 1.9×. This is roughly consistent with a linear density dependence, as would be expected if the energy variations responsible for the dephasing are due solely to dipole-dipole couplings whose average strengths are proportional to the ensemble density. Unfortunately, the range of densities over which Ramsey interference measurements could be accurately performed was limited by signal to noise at low density and the maximum density achievable in the current MOT configuration. Therefore, it was not possible to measure the dephasing rates over a wider range of densities to confirm the linear dependence. Importantly, the fact that the experiment and simulations show the same density-dependence provides strong evidence that the large experimental widths are not due to experimental imperfections, such as temporal inhomogeneities in the applied electric field, as those would not be density dependent.

Comparison of the 2-atom and 4-atom simulations suggests that enabling exchange interactions with one additional pair of atoms increases the dephasing rate (i.e., the spread of coupled atom energies) in the far off resonance regime by approximately a factor of 3. The fact that the experimental widths are an additional factor of 14 wider suggests that couplings and correlations between significantly larger groups of atoms are responsible for dephasing in far off resonance regime. Taken together the Rabi flopping and Ramsey interference measurements provide a view of the evolution of complexity in population transfer in frozen Rydberg gases, with the principal on resonance couplings and dynamics restricted to nearest neighbors [5, 70, 81, 82], near resonant inter-

actions limited to nearest and next nearest neighbors, and far off resonance evolution involving couplings between many atoms.

Chapter 6

Directional Population Control Beyond the Exceptional Point in a Non-Hermitian System[1]

In the presence of exponential loss and/or gain, pseudo-two-level quantum systems exhibit complex eigenenergy surfaces whose real and imaginary parts are chiral functions of the coupling strength γ and energy separation δ between the bare states [118]. There has been substantial interest in exploring methods for robust quantum control in such non-Hermitian models. For example, controlled population transfer can be realized by adiabatically steering the system around a closed control loop in the (γ, δ) parameter space [119, 120]. Given the change in state in this context, the system evolution cannot be truly adiabatic. Nevertheless, the term is commonly used to describe trans-

formations that would be adiabatic for a similar system governed only by the real part of the Hamiltonian. Previous work has suggested that population transfer can only occur through such a transformation if the control loop encloses an exceptional point (EP), i.e., a point of energy degeneracy that exists at nonzero coupling in the eigenenergy landscape [121, 122]. Further studies predicted that the helicity of the control path, as well as its starting or ending point, can impact the population transfer probability and serve as additional control knobs [119, 123, 124, 125]. Experiments exploring these and related phenomena have been performed using microwave cavities [126], optomechanical cavities [120, 127], molecules [128, 129, 130], and other systems [131, 132, 133, 134, 135]. Recently, the nonadiabatic transition probability in a two-level system steered directly through two exceptional points was determined [136]. Here we present results of simulations based on numerical integration of the time-dependent Schrödinger equation (TDSE), showing that encircling an EP is not a necessary condition for control of directional population transfer in a two-level non-Hermitian system.

In the following sections we examine the adiabatic control problem for simple rectangular paths in the (γ, δ) parameter space for a generic two-level system in the presence of exponential decay (and/or gain). Our numerical simulations clearly show that directional population transfer can still occur in adiabatic transformations that do not enclose the EP. We also present an analytical model that identifies the mechanism responsible and predicts how far beyond the control loop boundary the EP can lie while still affording full directional population control.

6.1 Two-level System with Decay

Consider a pair of uncoupled states with energies E_1 and E_2 that spontaneously decay at rates of $2\Gamma_1$ and $2\Gamma_2$, respectively, to some unspecified levels. We assume that a coupling γ between the two states can be externally applied, and that γ and the energy splitting $\delta = E_2 - E_1$ between the bare states can be continuously varied. As a concrete example, this situation might be realized by driving two opposite-parity atomic states with a nearly resonant oscillating field. In a dressed-atom picture, δ is determined by the detuning of the field frequency from resonance and γ can be changed by varying the field strength. The system can be described by an effective non-Hermitian Hamiltonian

$$H = \begin{pmatrix} -E_1 - i\Gamma_1 & \gamma^* \\ \gamma & -E_2 - i\Gamma_2 \end{pmatrix} \tag{6.1}$$

in atomic units.

Without loss of generality, we can further simplify the Hamiltonian. First, we translate the complex energy origin, subtracting $-E_1 - i\Gamma_1$ from the diagonal matrix elements. Next, we define γ to be real and positive. Finally, we rescale all terms in the Hamiltonian by dividing them by the difference in the decay rates of the two bare states. The Hamiltonian is then a function of only two variables γ and δ and takes the convenient form

$$H' = \begin{pmatrix} 0 & \gamma \\ \gamma & -\delta - i \end{pmatrix}, \tag{6.2}$$

where one of the uncoupled basis states does not decay and the other decays with a characteristic lifetime $\tau = \frac{1}{2}$.

Figures 6.1(a) and 6.1(b) show the real and imaginary parts of the eigenvalue surfaces E as a function of δ and γ. At each point, the surface colors identify the eigenstates with the smallest (magenta) and largest (cyan) rates of decay, i.e., the magenta eigenstate has the eigenvalue with the least-negative imaginary part. The surfaces exhibit a point of degeneracy, the EP, at $\left(\delta = 0, \gamma = \frac{1}{2}\right)$. For $\left(\delta = 0, \gamma > \frac{1}{2}\right)$, the real parts of the eigenvalues form an avoided level crossing, whereas for $\left(\delta = 0, \gamma \leq \frac{1}{2}\right)$ they cross with zero gap. Conversely, the imaginary parts of the eigenvalues exhibit a line of degeneracy, $\left(\delta = 0, \gamma \geq \frac{1}{2}\right)$.

When attempting to understand how an initial state of the non-Hermitian system will be transformed during a closed control loop, it is tempting to assume that the principal effect of the imaginary part of the Hamiltonian is a steady leak of population from the two levels. Under that assumption, one might neglect the difference in the decay rates of the two states (i.e., ignore the imaginary part of the effective Hamiltonian) and consider only the evolution on the real part of the eigenvalue surfaces. In that case, if the system is initially in one of the two eigenstates, it will remain in an eigenstate throughout a perfectly adiabatic transformation. The character of the initial state will vary smoothly with time as γ and/or δ are changed, with the system evolution well described by a path that does not leave the eigenenergy surface. Inspection of Figure 6.1(a) would then predict that because of the line of degeneracy in the surface, any closed adiabatic path (regardless of its shape or the direction of

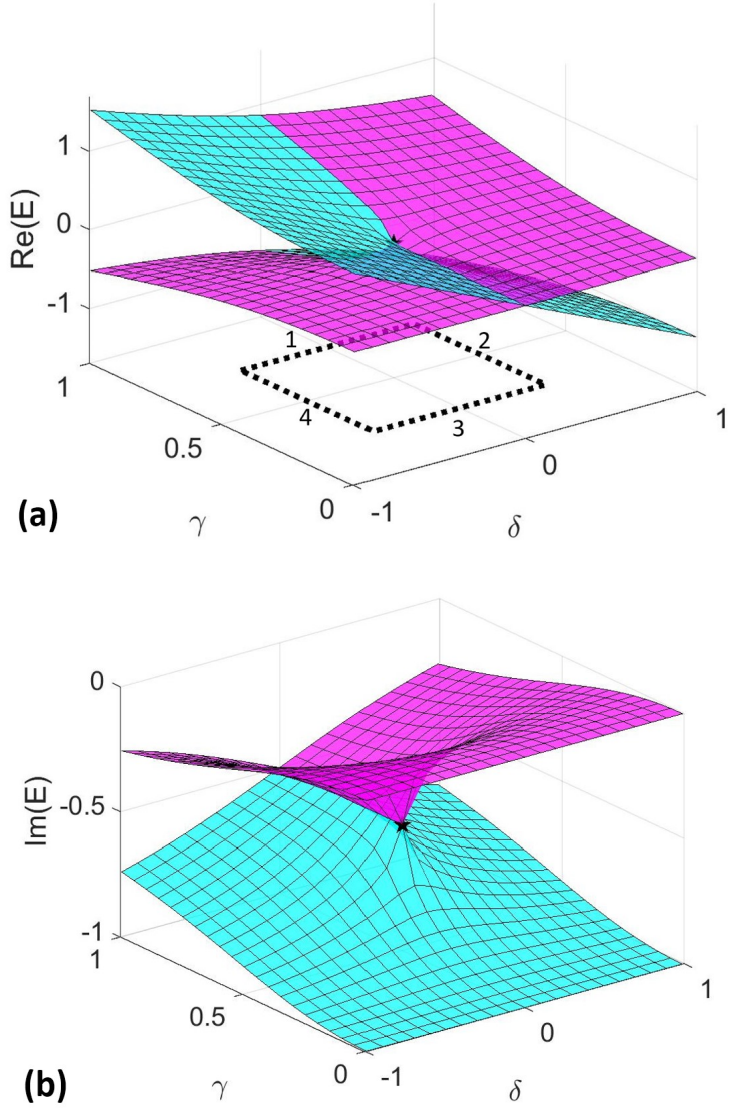

Figure 6.1: (a) Real and (b) imaginary parts of the eigenvalue surfaces E for the coupled pseudo-two-level system with decay. Magenta and cyan correspond to the states with the smallest and largest decay rates, respectively. The black star marks the EP $\left(\delta = 0, \gamma = \frac{1}{2}\right)$. The dashed line beneath the real part of the eigensurfaces illustrates the form of the closed path transformations we consider in detail (see the text), with two legs (labeled 1 and 3) at constant γ and two legs (labeled 2 and 4) at constant δ.

travel) that encircles the EP (an odd integer number of times) will result in complete population transfer from one eigenstate to the other. Any adiabatic path that does not encircle the EP (or encircles it an even integer number of times) results in no net population transfer.

However, not only does the presence of an imaginary part of the Hamiltonian lead to decay of the system as a whole, it can fundamentally change the system evolution during the control loop and accordingly the final result of the transformation. The primary issue is related to the asymmetric decay of the two eigenstates and the fact that no dynamical process of finite duration can be truly adiabatic. While nonadiabatic (de)excitations resulting from time-varying external controls can be reduced to negligible levels in Hermitian systems, they can be dramatically amplified by the unequal decay rates from the constituent eigenstates during a slow transformation. Increasing the loop time can reduce any nonadiabatic effects associated with the time-dependent controls, but simultaneously enhances the impact of the differential decay. Indeed, it has been shown, contrary to the naive picture presented in the preceding paragraph, that the population transfer in the non-Hermitian system is actually chiral. Depending on the helicity of the control loop, population transfer is effective for only one of the two eigenstates, with the other essentially unaffected by the process [120]. Also in contrast to the Hermitian picture, the transfer probability for a given closed control loop also depends on the starting point (δ_0, γ_0) of the transformation [125]. Here we demonstrate via simulations based on numerical integration of the TDSE and explain through an analytic model another important result stemming from the difference in

decay rates of the bare states, namely, closed control loops need not enclose the EP to induce selective population transfer.

For convenience, we focus on rectangular control loops that can be separated into four distinct segments (or legs). As shown in Figure 6.1(a), δ varies along legs 1 and 3 (with constant $\gamma = \gamma_{\max}$ and $\gamma_{\min}$, respectively) and γ varies along legs 2 and 4 (with constant $\delta = \delta_{\max}$ and $-\delta_{\max}$, respectively). Moreover, for ease of illustration, we exclusively consider population transfer from systems that are initially prepared in one of the two eigenstates. All closed loop transformations start from $(\delta_0 = 0, \gamma_0 = \gamma_{\max})$. Because our primary goal is to understand how the *relative* populations are affected by the system transformations, when plotting the state populations (or population transfer probability) at a particular time, we normalize to the total population remaining in the system at that time. It is worth noting that the reduced Hamiltonian has the same form if one or both of the bare states experience exponential gain rather than decay (as, for example, with optical modes in a cavity with gain), so our consideration of times long compared to τ does not imply negligible system population.

Figure 6.2 illustrates the principal effect we explore in this paper. In Figure 6.2(a) the clockwise control loop encloses the EP and initial population in the upper state is transferred to the lower state, while initial population in the lower state remains in the lower state. Following the same path in a counterclockwise direction (not shown) induces population transfer from the lower to the upper state, but not from upper to lower. In Figure 6.2(c) the control loop does not enclose the EP and there is no population transfer from either

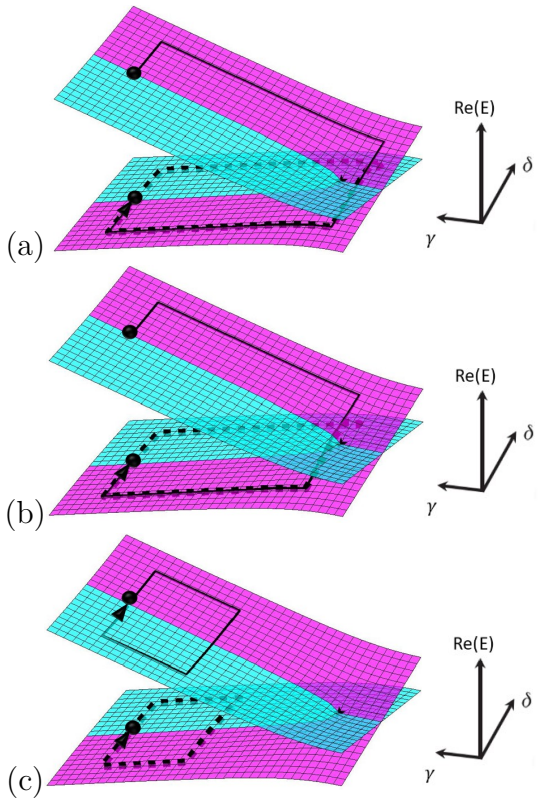

Figure 6.2: Energy expectation value of the two-level system, shown as a path in the real part of the energy eigenvalue landscape, computed via numerical integration of the TDSE for clockwise rectangular control loops. The three plots show control loops with different values of $\gamma_{\min}$: (a) 0.3, (b) 0.6, and (c) 2. The surface coloring designates the eigenvalue with the slowest (magenta) and fastest (cyan) decay, analogous to Figure 6.1, with a black star positioned at the EP, $\left(\delta = 0, \gamma = \frac{1}{2}\right)$. The thin solid (thick dashed) black lines show the energy expectation value vs (δ, γ) during the transformation, for initial system preparation in the upper (lower) eigenstate. For all cases in the figure (i) the start and stop point is $(\delta_0 = 0, \gamma_0 = 3)$, (ii) the detuning is varied over the same range, $-1 \leq \delta \leq 1$, and (iii) the duration of each leg of the control loop is 20τ, for a total transformation time of 80τ. In (a) the clockwise control loop encloses the EP and the initial population in the upper state is transferred to the lower state, while the initial population in the lower state remains in the lower state. In (c) the control loop does not enclose the EP and there is no population transfer from either initial state. Interestingly, complete and directional population transfer is observed in (b), despite the fact that the EP is not enclosed within the control loop.

initial state. Figure 6.2(b) shows that efficient chiral population transfer can still occur, even for closed control loops that do not enclose an EP, and under conditions where the evolution would be purely adiabatic (with negligible net population transfer from either initial state) in a Hermitian analog system. Adiabaticity of identical transformations in a Hermitian analog system whose eigenenergy surface closely matches the real part of the surface in our non-Hermitian system[1] has been directly confirmed via numerical integration of the TDSE. This observation begs the following questions. If not enclosure of the EP, what characteristics of a closed control loop determine whether population transfer occurs? For the rectangular loops that we consider, can we predict the range of $\gamma_{\min}$ values for which the transformation leaves the initial state unchanged?

To gain additional insight toward answering these questions, we have calculated the population transfer probability vs $\gamma_{\min}$ for families of clockwise and counterclockwise control loops (with the same value of $\gamma_{\max} = 3$, the same starting point ($\delta = 0, \gamma = 3$), and the same total loop time of 80τ) for three different values of $\delta_{\max}$. As shown in Figure 6.3, population initially in the upper (lower) eigenstates is largely unaffected by counterclockwise (clockwise) control loops for any values of $\gamma_{\min}$ and $\delta_{\max}$. However, for $\gamma_{\min}$ below some threshold (greater than 0.5), clockwise (counterclockwise) transformations result in efficient transfer from the upper (lower) eigenstate. We define the critical coupling γ_c as the smallest value of $\gamma_{\min}$ for which the population

[1]The Hermitian analog Hamiltonian is obtained by replacing the diagonal elements of the non-Hermitian Hamiltonian in Eq. 6.2 with their real parts and replacing the off-diagonal elements with $\sqrt{\gamma'^2}$, where γ'^2 is the greater of $\gamma^2 - \frac{1}{4}$ and 0.

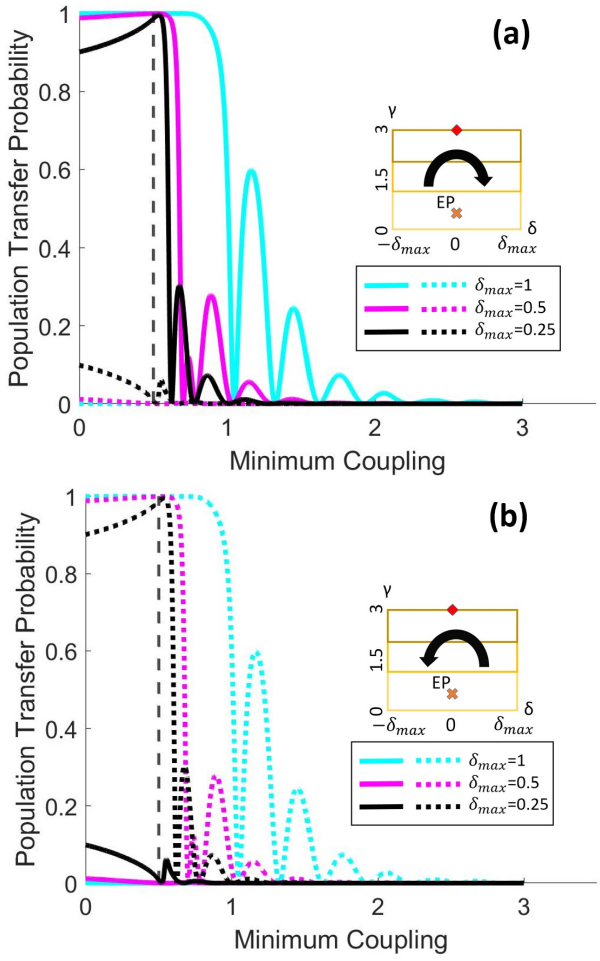

Figure 6.3: Population transfer probability computed via numerical integration of the TDSE as a continuous function of $\gamma_{\min}$ for closed rectangular control loops analogous to those in Figure 6.2 but for several different values of $\delta_{\max}$. Black, magenta and cyan curves correspond to $\delta_{\max} = 0.25$, 0.5, and 1, respectively. Results are plotted for (a) clockwise and (b) counterclockwise paths. The thick solid (dotted) lines give the transfer probabilities when the system is initially prepared in the upper (lower) eigenstate at the start of the control loop, $(\delta = 0, \gamma = 3)$. The thin gray vertical dashed line at $\gamma_{\min} = \frac{1}{2}$ marks the position of the EP. Loops with $\gamma_{\min} < \frac{1}{2}$ enclose the exceptional point, whereas those with $\gamma_{\min} > \frac{1}{2}$ do not. The duration of each leg of each control loop is 20τ, for a total transformation time of 80τ. The insets show examples of three different control loops, each with the same value of $\delta_{\max}$ and $\gamma_{\max}$, but different values of $\gamma_{\min}$.

transfer probability equals 0.5. As Figure 6.3 clearly shows, γ_c depends on the detuning range in the control loop. In particular, $\gamma_c > 0.5$ and increases monotonically, but nonlinearly, as a function of $\delta_{\max}$. For $\gamma_{\min} > \gamma_c$, the transfer probability exhibits oscillations whose amplitude decays with increasing $\gamma_{\min}$. The amplitude and rate of decay of those oscillations also depend on $\delta_{\max}$.

We first consider the dependence of γ_c on $\delta_{\max}$, i.e., on the width of the control loop. We note that Figure 6.2 suggests that, in general, population transfer is only significant during leg 3, as δ varies with $\gamma = \gamma_{\min}$. Therefore, to understand the principal aspects of the population transfer dynamics, we can focus on the evolution during leg 3. Along that path, for $\gamma_{\min} > 0.5$, the system traverses an avoid crossing in the real part of the eigenvalue surface (Figure 6.4). Accordingly, if the Hamiltonian were Hermitian, the population transfer probability would be well described by the standard Landau-Zener formula [137]. As such, one might expect that the key parameter in determining the population transfer probability would be the rate at which the system passes through the avoided crossing. However, Figure 6.5 illustrates that this expectation generally fails in the non-Hermitian case, even for adiabatic transformations where the detuning is scanned sufficiently slowly that there is negligible population transfer in an analogous Hermitian system with the same avoided crossing characteristics.

Figure 6.5 shows the population transfer probability as the detuning is adiabatically scanned along leg 3, for fixed values of the detuning end points, but for different scan rates and different coupling strengths (i.e., different energy gaps at the center of the avoided crossing). While the details of the population

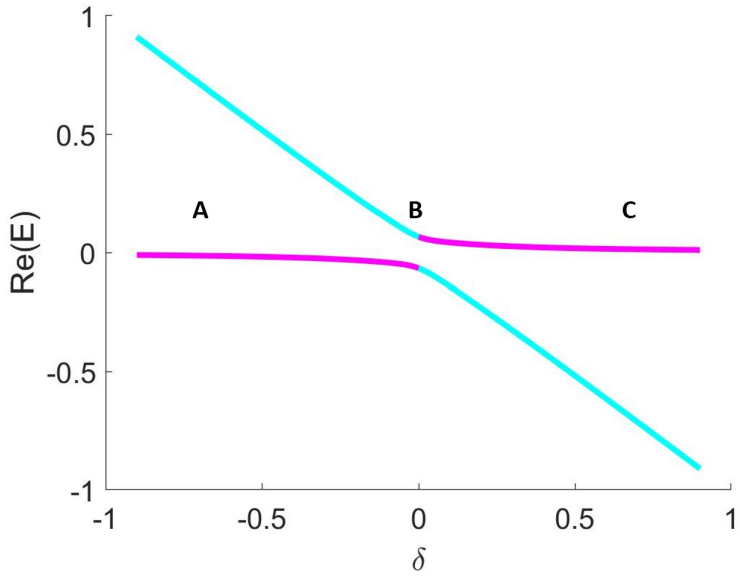

Figure 6.4: Avoided level crossing along leg 3 of the control loop for a coupling strength γ slightly greater than $\frac{1}{2}$. Far from the avoided crossing, the eigenstates are nearly equivalent to the bare states. Magenta and cyan denote the more slowly and rapidly decaying eigenstates, respectively. The letters label three principal regions of population evolution during a detuning scan through the avoided crossing.

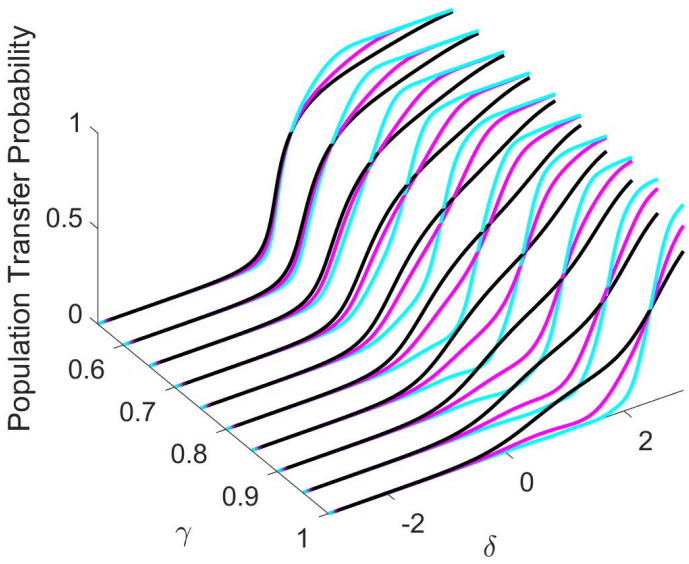

Figure 6.5: Population transfer probability between two eigenstates calculated via numerical integration of the TDSE as the detuning δ is scanned from -3 to 3 at different couplings γ with constant detuning scan rates of $\frac{d\delta}{dt}$ =0.25 (cyan), 0.5 (magenta) and 1 (black).

transfer along the path depend on the scan rate and coupling strength, the value of the detuning (i.e., the position along the path) at which 50% transfer occurs is nearly independent of the scan rate (within the adiabatic regime). Apparently, it is the range of δ, and not the rate at which δ is scanned, that determines γ_c for the adiabatic passage. As we show below, this is because the differential decay rate of the bare states plays a dominant role in the population transfer.

6.2 Landau-Zener Transition in Non-Hermitian Systems

As noted above, the well-known Landau-Zener formula gives the probability of population transfer at an avoided crossing in a two-level Hermitian system as the energy difference between two bare states is scanned through degeneracy at a constant rate [137]. The extension of the problem to non-Hermitian systems has also been studied in detail [138, 139]. We take an alternative approach, using an approximate model that allows us to develop an analytic expression for the critical value $\delta_{\max} = \delta_c$ at which the population transfer probability is 0.5 for a given value of γ. We assume that the detuning range is sufficiently large that the system evolution along leg 3 can be divided into three regions (Figure 6.4). In regions A and C, $\delta \gg \gamma$, so the eigenstates are approximately equivalent to the bare states, one of which does not decay and the other decaying with a lifetime, $\tau = \frac{1}{2}$. Note that energy ordering of the slow and fast decaying states is opposite for regions A and C. In region B, $\delta < \gamma$, the two eigenstates are nearly equal admixtures of the two bare states, and they decay at approximately the same rate. Therefore, there is negligible relative decay. Accordingly, the population transfer between the two states in region B is accurately described by a Hermitian Landau-Zener formula, assuming a coupling $\sqrt{\gamma^2 - \frac{1}{4}}$ that exhibits approximately the same energy gap as the non-Hermitian system at $\delta = 0$.

Inspection of Figures 6.2 and 6.3 shows that for the control loops we have considered, significant population transfer occurs only when the system enters

leg 3 with essentially all population in the more slowly decaying eigenstate. Therefore, to predict the value of δ_c for a given γ along leg 3, we only need to examine two cases: all population initially in the lower (upper) state traversing the avoided crossing from left to right (right to left) as shown in Figure 6.4. Since these two cases are equivalent, we focus on the left to right transformation, progressing through regions from A to B to C.

Within the model, the eigenstates are approximately equivalent to the bare states in region A. So if all population is initially in the nondecaying state, it will remain there throughout region A and at the start of region B. The Landau-Zener formula [137] then predicts the following populations in the nondecaying (upper) state

$$P_{ND} = \exp\left[-2\pi\left(\gamma^2 - \frac{1}{4}\right)\Big/\frac{d\delta}{dt}\right] \tag{6.3}$$

and decaying (lower) state

$$P_D = 1 - \exp\left[-2\pi\left(\gamma^2 - \frac{1}{4}\right)\Big/\frac{d\delta}{dt}\right] \tag{6.4}$$

at the beginning of region C. Of course, in the adiabatic regime $\left(\gamma^2 - \frac{1}{4}\right)/\frac{d\delta}{dt} \gg 1$, so $P_D \approx 1$. However, P_{ND} is non-zero provided $\frac{d\delta}{dt} > 0$.

In region C, the population in the nondecaying level does not change, but the other decays exponentially with a time constant τ,

$$P_D(t) \approx \exp\left(-\frac{t}{\tau}\right), \tag{6.5}$$

where we have defined $t = 0$ at the start of region C. For a constant scan rate,

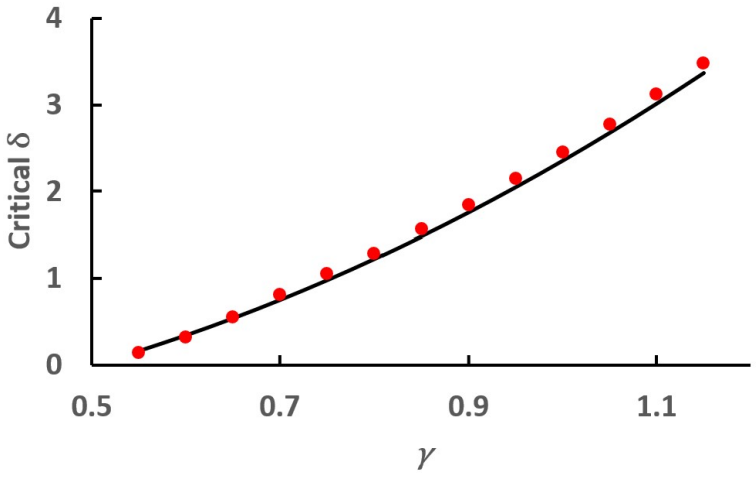

Figure 6.6: Critical detuning δ_c vs coupling γ as determined from TDSE simulations of population transfer along leg 3 using the non-Hermitian Hamiltonian (filled circles) and the analytic approximation $\delta_c = \pi\left(\gamma^2 - \frac{1}{4}\right)$ (solid line).

we can substitute $t = \delta / \frac{d\delta}{dt}$ and $\tau = \frac{1}{2}$ to obtain

$$P_D(\delta) \approx exp\left(-2\delta \Big/ \frac{d\delta}{dt}\right). \tag{6.6}$$

At the end of region C, $\delta = \delta_{\max}$. By definition, if $\delta_{\max} = \delta_c$, then there is 50% relative population transfer during the transformation and we have $P_{ND} = P_D(\delta_c)$. Accordingly, we find $\delta_c = \pi\left(\gamma^2 - \frac{1}{4}\right)$, independent of the scanning rate.

Figure 6.6 compares the approximate analytic prediction for δ_c with simulation results based on population transfer along leg 3 using the non-Hermitian Hamiltonian. The agreement is excellent.

6.3 Extension to Closed Control Loops

We can readily extend the model of population transfer during just leg 3 to the full control loop, starting and ending at $(\delta = 0, \gamma_{\max})$. To predict γ_c for the closed loop, we again only need focus on situations where non-negligible population transfer occurs during leg 3, i.e., clockwise paths starting from the upper eigenstate and counterclockwise paths starting from the lower eigenstate (Figure 6.2). During the first $\frac{3}{8}$ of the loop, the system population remains in the initial, slow decaying state. Any small level of population transfered to the other eigenstate (due to imperfect adiabaticity) rapidly decays. Thus, all population is in the slow decaying state when the system enters leg 3. Population transfer can then occur during leg 3 as described in the preceding section, with $\gamma_c = \sqrt{\frac{\delta_{\max}}{\pi} + \frac{1}{4}}$. The plot in Figure 6.7(b) shows this analytic prediction for γ_c, along with simulation results based on population transfer during the first $\frac{5}{8}$ of the control loop with the full non-Hermitian Hamiltonian. The agreement is again excellent.

Continuing on the remaining $\frac{3}{8}$ of the control loop after leg 3, small levels of probability amplitude transfer between the two eigenstates (again due to imperfect adiabaticity) can interfere with the non-negligible population in the two eigenstates for a substantial effect. The oscillations in the population transfer for the full loop, visible in Figure 6.3 for $\gamma > \gamma_c$, are the result of that interference. Those interferences also cause a substantial steplike increase in the value of γ_c with increasing $\delta_{\max}$, as shown in Figure 6.7(a).

It is worth noting that using our operational definition based on the evolu-

tion of a Hermitian analog system, the adiabaticity of the closed-loop transformation improves with increasing distance of the (excluded) EP from the path. This is because the energy gap at the avoided crossing along the minimum coupling leg increases the further the EP is from the path. Thus, adiabatic behavior can be achieved with reduced transformation times. In addition, as shown by the magenta and especially the black curves in Figure 6.3, we find that in some cases the effectiveness of the population swap actually improves for loops that do not enclose the EP, with the population transfer probability increasing as $\gamma_{\min}$ is tuned from the EP toward γ_c.

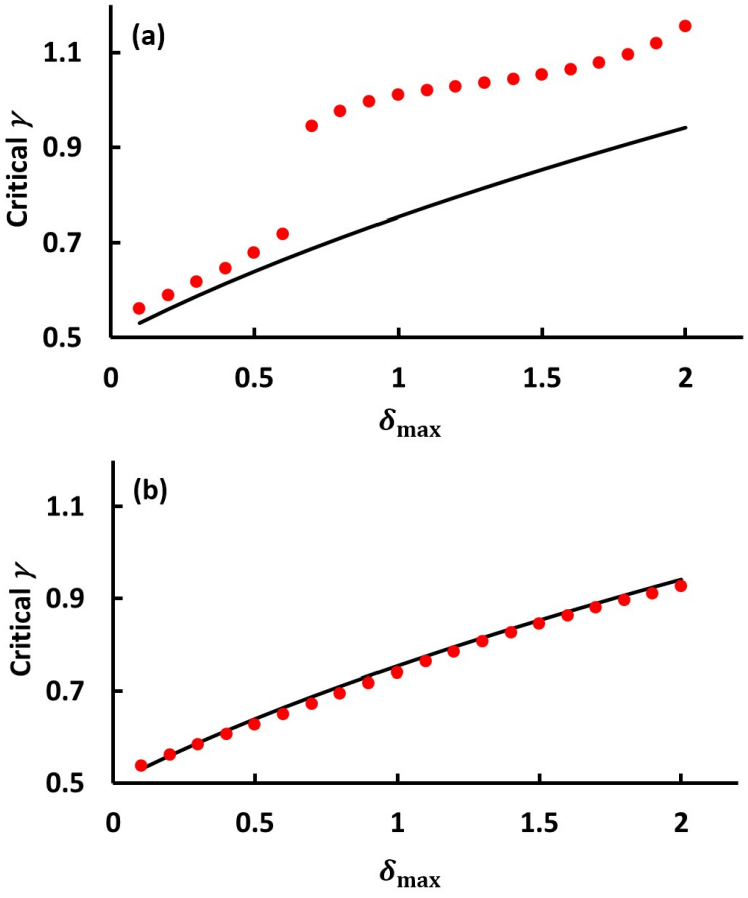

Figure 6.7: Critical coupling γ_c (filled circles) for which 50% relative population transfer occurs vs maximum detuning, according to TDSE simulations with the non-Hermitian Hamiltonian over (a) the full control loop and (b) the first $\frac{5}{8}$ of the control loop. The solid curve is the expression $\gamma_c = \sqrt{\frac{\delta_{\max}}{\pi} + \frac{1}{4}}$ derived in the text.

Chapter 7

Summary and Outlook

The identification of dephasing mechanisms, and the development of techniques to suppress it, continue to be important for ongoing research in many-body quantum physics, especially so for engineering quantum computers/simulators. In this dissertation, dephasing of Rydberg atom gas ensembles is thoroughly modeled and measured. Beyond that, suppression of dephasing is achieved with detuning jump sequences, enabling us to achieve the first observation of Rabi flopping in random dipole-dipole coupled systems with more than a few atoms.

More specifically, dephasing in Rydberg atom gas ensembles is visualized via experiments and simulations based on random collections of 2 or 4 atom group ensembles, and demonstrated by: (1) the fast decay of the Rabi oscillation amplitude for ensembles of $32p_{3/2}(|m_j = 3/2|)$ atoms subject to $32p_{3/2}(|m_j = 3/2|)$ $32p_{3/2}(|m_j = 3/2|)$ to $32s33s$ resonant energy transfer through dipole-dipole interactions (for both on and off resonance cases); (2)

cusp rather than Lorentzian lineshapes for the energy transfer probability as the splitting between the bare $32p_{3/2}(|m_j = 3/2|)$ $32p_{3/2}(|m_j = 3/2|)$ and $32s33s$ pair state energy is Stark tuned; and (3) fast decay of Ramsey interference fringes based on the same energy transfer resonance. Comparison between experimental results and simulations based on 2 atom (for which excitation hopping cannot occur) or 4 atom group ensembles (for which limited excitation hopping can occur), guides the discussion of effects of different dephasing mechanisms.

To suppress dephasing, in chapter 4, detuning jump sequences are introduced. These involve driving a resonant energy transfer at positive and negative detunings of equal magnitude in consecutive time periods, and repetitions of that fundamental jump sequence. The mechanism of dephasing suppression within the sequence is discussed via an analytical model, and its performance is demonstrated experimentally and characterized through numerical simulations. Large detunings paired with more jumps allows for greater suppression of dephasing.

Chapters 3 and 5 consider two major mechanisms contributing to the fast dephasing of a dipole-dipole coupled Rydberg atom gas. One is the inhomogeneous dipole-dipole interaction strength across the ensemble, resulting in different local Rabi oscillation frequencies among local groups of atoms. The other is excitation hopping of Rydberg excitations, which continuously changes the interatomic distance of interacting Rydberg atom pairs, thus changing the relevant Rabi frequency. By extracting frequency spectra from time domain population transfer measurements and simulations for Rydberg gases allowed

to interact at a constant detuning from resonance, or subject to detuning jump sequences or time-domain Ramsey interference sequences, it was found that the dephasing rate has a linear dependence on density and a positive relation with detuning (when considering excitation hopping). By comparing the experimental frequency spectra with different simulation models at different densities and detunings, in chapter 5, we concluded that excitation hopping induced dephasing becomes more pronounced at higher detunings, and dephasing caused by either mechanism increases linearly as density inreases.

Beyond the discussion of dephasing and decoherence in Rydberg atom ensembles, chapter 6 focuses on directional population control in a non-Hermitian system. We have shown that encircling an EP is not a necessary condition for achieving directional population control via closed-loop adiabatic transformations in a non-Hermitian system. We present an analytic model that explains the conditions needed to achieve control outside the EP in a two-level system, predicting the minimum distance between the control path and the EP for a class of rectangular control loops in the two-parameter (bare level detuning and coupling strength) energy landscape. Experimental verification of the predictions may require a system in which one or both of the uncoupled states experiences exponential gain, rather than loss, to maintain non-negligible population in the system during the long adiabatic transformation times.

To further our understanding of dipole-dipole coupled gases through future research, a few updates to the current simulation and experimental tools could be beneficial. Simulations based on ensembles of more than four atoms would increase their accuracy, especially for high detuning cases where excita-

tion hopping effects are more pronounced. Moreover, simulations that include experimental imperfections like non-instant detuning jumps would be helpful not only for improving the accuracy of the simulations, but also for deciding if those effects noticeably change the behavior of the system. Furthermore, for simulations beyond ~1μs time scales, which are necessary for studying microscopic decoherence rather than macroscopic dephasing in the current experimental setup, the effects of spontaneous decay and blackbody radiation would need to be added to the model to more accurately represent what is happening in the system over longer timescales.

In terms of experiments, the current apparatus could be modified to allow for increased accuracy and stability. Possible improvements include higher fidelity electric field generation (shortening ramp up/down time for detuning jumps and eliminating voltage ringing after jumps), lower noise electrical signal amplification and transmission, better laser systems with improved frequency and power stability (readily available in the lab), and most importantly, a more stable MOT setup that reduces or eliminates the need of rubber suspension components. For example, instead of suspending and vibrating the retro-reflecting mirrors to average out standing wave patterns, one could vibrate and suspend a piece of glass to modulate the phasefronts of MOT beams to achieve the same effect. In this case, the retro-reflecting mirrors can be rigidly attached to the optical table, increasing stability.

As for future research directions, detuning jump sequences open the door for suppressing dephasing and decoherence in different physical systems, and together with Ramsey interference experiments, enable detailed studies of de-

phasing mechanisms. Specifically, a few twists on the current experimental apparatus can enable the study of the following topics.

7.1 Experimental Verification of the Contribution of Excitation Hopping to Dephasing

The Ramsey interference experiments prove to be a valuable tool for extracting frequency spectra and, thus, dephasing times. To better understand the dephasing mechanism with experiments, Ramsey interference experiments could be performed at different detunings and densities. To experimentally verify the effects of excitation hopping, ensembles that could turn on/off hopping effects would be very helpful. This means creating ensembles of two, four, eight etc. interacting atoms and exposing them to experimental sequences like detuning jumps and Ramsey interferences. In principle, this could be achieved via tweezer arrays. Comparison between experimental data based on ensembles of two, four, eight etc. interacting atoms could confirm the conclusions regarding the effects of excitation hopping or other dephasing mechanisms drawn from simulations.

7.2 Performance of Detuning Jump Sequences in More Ordered Systems

We have shown that detuning jump sequences can extend dephasing times in a highly inhomogeneous Rydberg atom gas. While highly ordered Rydberg atom ensembles can now be realized experimentally [21, 140], suppressing dephasing remains a major goal for enabling experiments and applications. To determine if detuning jump sequences might enhance the performance of those systems as well, simulations of the evolution of pairs of atoms with an average interatomic separation of 3μm and standard deviation of 50nm (Gaussian distribution), and internuclear axes aligned to an external electric field axis have been performed. This particular setup might be readily realized experimentally using optical tweezer arrays.

Detuning jump sequences for applications in those systems might be especially useful if well-defined population transfer between pp and ss' could be achieved on demand. As an example, to achieve 100% transfer, according to the theoretical model discussed previously where $P(ss'(T)) = \frac{2\mathcal{N}^2\Omega^2}{\widetilde{\Omega}^2}\left(1 - \cos\frac{\widetilde{\Omega}T}{2\mathcal{N}}\right)$, in the limit of $\delta \gg \Omega$, the number of jumps and detuning should be matched so that $\frac{2\mathcal{N}^2\Omega^2}{\widetilde{\Omega}^2} = \frac{1}{2}$, i.e., $\delta = \sqrt{4\mathcal{N}^2 - 1}\Omega$. Simulations (Figure 7.1) show that an ordered ensemble subject to the detuning jump sequence described above (matching number of jumps and detuning), rather than being driven on resonance, substantially reduces dephasing, for the same Rabi frequency. However, as discussed previously, the amplitude enhancement offered by the jump sequences does not match the prediction from the analytic model, unless the net

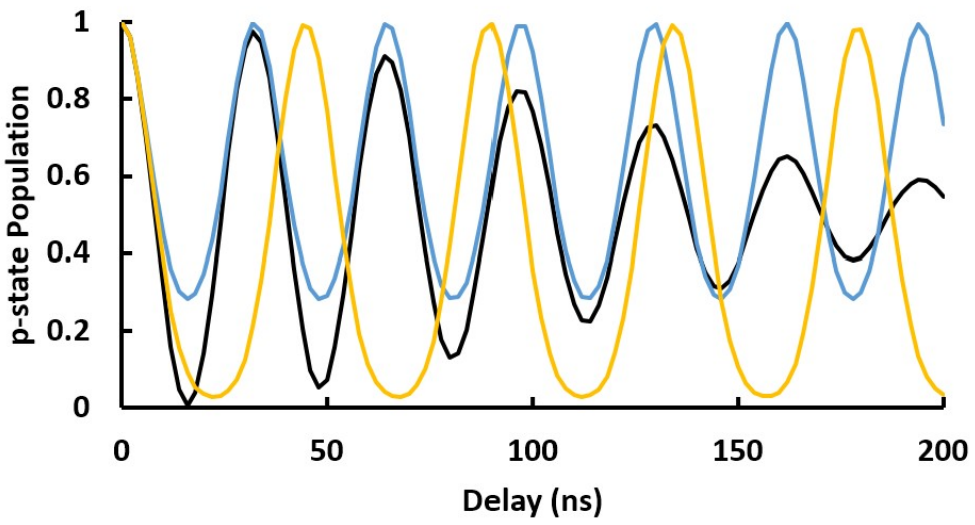

Figure 7.1: Simulation results of p state population (normalized to the total Rydberg population) as a function of time when an ensemble of p atom pairs, oriented along an external electric field axis with an average interatomic distance of 3μm and standard deviation of 50nm (Gaussian distribution), is tuned to energy transfer resonance (black) or subject to 2 jumps at detuning of $\delta = \sqrt{4\mathcal{N}^2 - 1}\Omega_{\text{avg}}$ (blue) or $\delta = 0.7\sqrt{4\mathcal{N}^2 - 1}\Omega_{\text{avg}}$ (yellow).

population transfer is $\ll 1$. Accordingly, the maximum population transfer to ss' in the case of $\mathcal{N}$ jumps with detuning of $\delta = \sqrt{4\mathcal{N}^2 - 1}\Omega$ is ~70% rather than 100%. This can be rectified by reducing the detuning slightly (at the price of lower Rabi frequency and a somewhat distorted Rabi oscillation profile (i.e., not a perfect cosine waveform)). For example, with $\delta = 0.7\sqrt{4\mathcal{N}^2 - 1}\Omega$, a peak population transfer of 97.2% can be achieved. Even higher peak population transfer rates can be achieved when the detuning is further reduced.

7.3 Suppressing Decoherence with Detuning Jump Sequences

So far, our discussion of jump sequences has centered on their use for suppressing dephasing. However, the sequences might also serve to suppress microscopic decoherence, i.e., to suppress time-dependent phase variations within local ensembles. It should be noted that the mechanisms responsible for decoherence in Rydberg gases can be quite complicated, including thermal motion, spontaneous decay, interactions with blackbody radiation, etc. Here the discussion focuses on how jump sequences could suppress decoherence caused by thermal motion of atoms.

Consider two atoms that are gradually drifting apart from each other. For simplicity suppose this results in a linear decrease in the interaction strength between them, and a linear decrease in their on resonance Rabi frequency, at a rate $\frac{d\Omega}{dt}$. This means the phase difference between the two on resonance eigenstates in the moving atom system would lag behind the same phase difference in an otherwise identical stationary system (where atoms remain in their starting positions), by $\frac{1}{2}\frac{d\Omega}{dt}T^2$ after an interaction time T.

For a system subject to detuning jump sequences, the sign of the energy difference between the two eigenstates is reversed whenever a detuning jump occurs, resulting in a net phase lag over the jump cycle that is the difference between the phase lags in the two halves of the jump cycle. In addition, as discussed previously, in the large detuning regime, the generalized Rabi frequency is $\widetilde{\Omega} \approx \delta + \frac{\Omega^2}{2\delta}$. Thus, in regimes where changes in the coupling

strength over a single jump cycle are small ($\frac{d\Omega}{dt}T \ll \Omega$), we have $\frac{d\widetilde{\Omega}}{dt} = \frac{\Omega}{\delta} \cdot \frac{d\Omega}{dt}$, so that the magnitude of the change in the eigenstate energy splitting due to atom motion is significantly smaller than in the on resonance case. Considering both factors, after $\mathcal{N}$ jumps at a detuning δ, the phase difference between the two eigenstates in a pair of moving atoms only lags behind the phase difference in a pair of stationary atoms by $-\frac{\Omega}{4\mathcal{N}\delta}\frac{d\Omega}{dt}T^2$, where T is the total evolution time. This is a significantly smaller phase difference as compared to the on resonance case (in terms of absolute value), and will result in substantially reduced decoherence within the ensemble. Note that the magnitude of the ratio of the phase differences for the jump to on resonance scenarios is $\frac{\Omega}{2\mathcal{N}\delta}$, which by construction ($\mathcal{N} > 1$, $\delta \gg \Omega$) is $\ll 1$.

Experimentally, the microscopic coherence of the ensemble can be characterized through the population transfer enhancement achieved with detuning jump sequence [37]. To clearly see the effects of decoherence under current conditions in our MOT, where the average motion of atoms is slow, the experimental delay times needed to observe decoherence is ~10μs and beyond. However, for the s, p and s' states considered in this dissertation, spontaneous decay and state redistribution due to blackbody radiation also occur on the ~10μs timescale, which could potentially cloud the interpretation of such a decoherence experiment. Although previous experimental results [5, 37] suggests that the coherence within a Rydberg atom gas is better preserved when more jumps are performed (within a given time period) - despite the presence of spontaneous decay and blackbody radiation -, to more quantitatively study how detuning jump sequences can suppress decoherence, more slowly decaying

Rydberg states should be used.

Overall, with the first observation and analysis of Rabi flopping in random dipole-dipole coupled systems with more than a few atoms, this dissertation has set a foundation for future experimental study of dephasing and decoherence suppression sequences based on detuning jumps, and pointed out a way to quantitatively study dephasing mechanisms in many-body systems like cold Rydberg gas subject to dipole-dipole interactions.

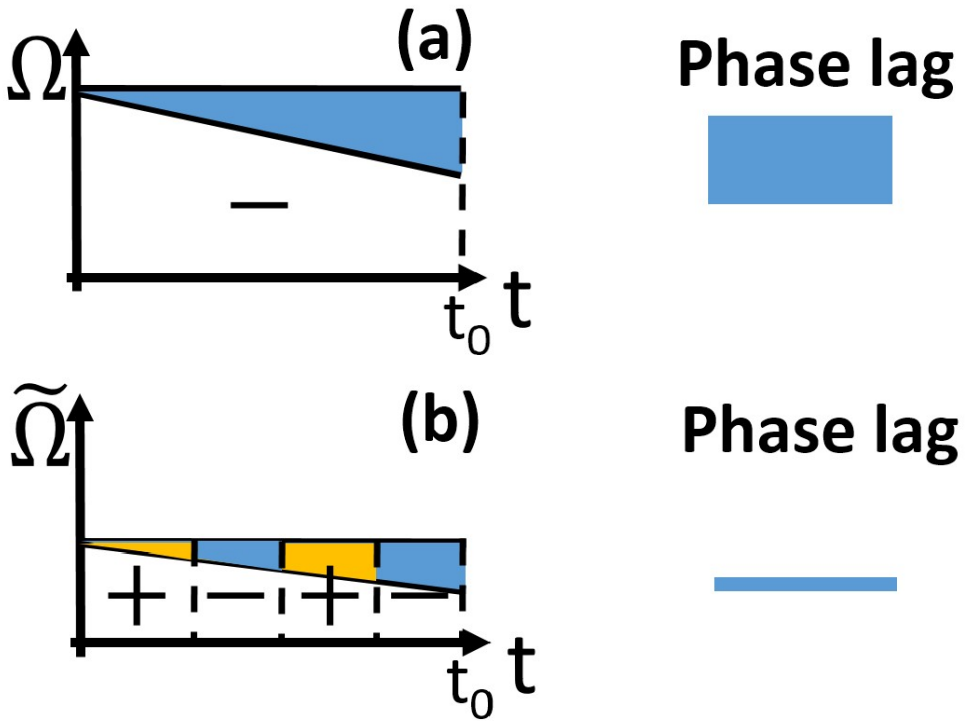

Figure 7.2: Illustration of phase difference ($\int \Omega dt$ or $\int \widetilde{\Omega} dt$, note $\widetilde{\Omega}$ is smaller in value) between two eigenstates of a pair of atoms at time t_0 for (a) on resonance eigenstates and (b) detuned eigenstates subject to two jumps, when the atoms are stationary (constant Rabi frequency/generalized Rabi frequency) or gradually coming apart (Rabi frequency/generalized Rabi frequency subject to linear shift). The signs and colors indicate if the energy of one state is higher than the other (blue), or the other way around (yellow). The cases where atoms gradually come apart show integrated phase differences, relative to the cases where atoms are stationary, proportional to the areas of the blue rectangle in the "phase lag" portion of the graphs.

Appendix A

Absence of Collective Decay in Lower Rydberg States

Many body quantum ensembles can exhibit collective behavior that is quite distinct from that of a group of uncorrelated individuals. In 1954 [141], Dicke provided the first physical model for N identical radiators in a small (compared to radiation wavelength) or properly phased extended ensemble in which correlated radiators coherently interfere with each other to achieve radiation rates much greater than ("superradiance") or much smaller than ("subradiance") those of individuals in the sample. Superradiance and subradiance have since been observed in many different contexts, and because superradiating systems exhibit a high level of cooperativity, they are good candidates for observing and utilizing many-body effects and remain topics of active research [51, 91, 142, 143, 144, 145, 146, 147, 148, 149, 150, 151, 152, 153, 154, 155,

156, 157, 158, 6, 159, 160, 161, 162, 163, 164, 165, 166]. However, to our best knowledge, despite the fact that superradiant emission between Rydberg states has been observed in extended hot atom ensembles long ago [159, 153, 154], it has never been experimentally observed in small atomic ensembles with sizes much smaller than the radiation wavelength (λ), and for very good reasons. There have been claims of observing superradiant transitions in cold Rydberg ensembles [142, 143], but the radiation itself was not observed directly, and other mechanisms that could be responsible for the rapid redistribution of population that was observed [167, 168, 169, 170, 171] were not ruled out. Chapter 3 provides an extensive discussion of dipole-dipole interactions which lead to inhomogeneous shifts of the eigenenergies of Rydberg atoms in a random ensemble. Thus, the requirement of "identical radiators" in Dicke's proposal cannot be strictly met in a very small and dense ensemble where the radiation path length $L < \lambda$, and/or the ensemble volume $V < \lambda^3$. The unavoidable variation in the frequency of the radiators across the ensemble suppresses superradiance effects. In fact, previous students in our group found no evidence for superradiance in cold Rydberg ensembles with a diameter of 0.4mm and densities ρ~$1.5 \times 10^9/\text{cm}^3$ and ρ~$3 \times 10^9/\text{cm}^3$ involving transitions with $\lambda > 1$mm [91].

In a cold Rydberg gas, two mechanisms, cooperativity and dephasing compete, encouraging and discouraging superradiance. Specifically, the dephasing rate from dipole-dipole interactions involving pairs of atoms can be written as

$$\gamma_{DD} = \frac{\pi \mu^2 \rho}{4\epsilon_0 \hbar} \text{ [154]}, \tag{A.1}$$

here μ^2 is the sum of the transition dipole moments $\Sigma \langle n_1 l_1 | \hat{r} | nl \rangle \langle n_2 l_2 | \hat{r} | nl \rangle$ associated with all the possible (near) resonant dipole-dipole interaction channels involving the initial quantum state $|nlnl\rangle$ to $|n_1 l_1 n_2 l_2\rangle$, ρ is the number density of Rydberg atoms. Note that in reality the dipole-dipole dephasing rate is even higher, due to the possibility of interactions involving more than two atoms. Conversely, the superradiant decay rate is

$$\gamma_{SR} = \frac{\pi \mu^2 \rho}{3\epsilon_0 \hbar} \frac{L}{\lambda} \text{ [154]}, \tag{A.2}$$

where λ is the wavelength of the radiation, and L is the path length of radiation through the sample. A comparison between the two rates suggests that superradiance should occur before dephasing can suppress it if, and only if, $\frac{L}{\lambda} \gg 1$. In fact, to our knowledge, all observations of superradiance to date have involved extended ensembles where $\frac{L}{\lambda} \gg 1$ is met, and often with the assistance of resonant cavities which boosts cooperativity [144, 145, 146, 148, 149, 150, 151, 153, 154, 155, 156, 157, 158, 159, 160, 161, 162, 163, 164, 165, 166]. As noted above, previous students were unable to observe any evidence for superradiance from Rydberg atoms excited in a Rb MOT with a diameter of 0.4mm for the $26s$ to $25p$ transitions with λ~1mm, or for similar transitions between higher n states involving longer wavelengths [91]. More recently, we performed additional experiments to explore whether any evidence for accelerated radiative decay of Rydberg atoms, in a comparable volume, could be observed for shorter wavelength transitions involving lower Rydberg states for which $\frac{L}{\lambda} \geq 1$.

Thanks to the addition of electric field plates, rather than field rods (the plates used in this experiment are two parallel sheets of high transparency stainless steel mesh, supported by rigid stainless steel frames), a higher ionization field strength (~5000V/cm) could be applied to atoms in the MOT (when simultaneously applying a positive voltage pulse to back plate and a negative voltage pulse to front plate) compared to previous experiments [91], where the maximum ionization field was limited to <2000V/cm. This strong field allowed $19s$ and $19p$ Rydberg states to be field ionized and thus detected with SSFI. The wavelength of the $19s$ to $18p$ transition is 0.33mm, substantially shorter than the 1mm transition wavelength of $26s$ to $25p$ transition, and less than the 0.5mm FWHM of the MOT (at densities of 0.5-4.3$\times 10^8$/cm^3). If $\frac{L}{\lambda} > 1$ encourages superradiance, then the $19s$ to $18p$ transition in a 0.5mm MOT should be more likely to exhibit superradiance than the $26s$ to $25p$ transition in a similarly sized MOT (0.4mm FWHM in the previous students' case).

To determine if collective effects influenced the decay of initially populated $19s$ atoms in our MOT, atoms within MOT were first excited from the upper trap state ($5p_{3/2}$) to the $19s$ state with pulsed dye laser. The laser utilized an infrared laser oscillator (using LDS 925 dye), whose output was frequency doubled and then amplified (using Couramin 460 dye) in an attempt to suppress large Rydberg density fluctuations due to spectral noise in the direct output from the Nd:YAG pumped multi-mode dye laser. The detailed operation principles of pulsed dye lasers can be found in the dissertations of previous students [51, 5, 74]. After a variable delay time (0-80μs, as controlled by a digital delay generator), ramped voltages of opposite signs were applied to the front and

back field plates, ionizing the Rydberg atoms and enabling the measurement of the population in the $19s$ and $19p$ energy levels at given delay time. It should be noted that although the beginning (trigger) time for the ionization pulses can be well defined, the actual ionization time for different states of atoms can only be determined to be somewhere during the ~5μs ionization pulse. Thus, to accurately determine the ionization time, the time dependence of the $19p$ population profile is used as a calibration. The $19p$ atoms are excited from the $19s$ state via blackbody radiation and decay via spontaneous emission to lower lying ns and nd states. As a result, the population in $19p$ state as a function of time exhibits a well-defined peak. Lining up the temporal peak in the measured $19p$ population with simulation results including the effects of spontaneous emission and blackbody radiation allows us to accurately define the ionization (i.e. measurement) time for the $19s$ states, which is 2.3μs after ionization pulse trigger in this case.

The population in the $19s$ and $19p$ states is recorded as a function of delay and compared to a theoretical model considering population transfer due to spontaneous emission as well as blackbody radiation between $18s$, $19s$, $20s$, $17p$, $18p$, $19p$, $17d$, $18d$ states, but not superradiance effects. Any statistically significant difference in the measured population change (enhancement or suppression) from the theoretical model could provide evidence for collective decay.

As with experiments performed by previous students on more highly excited atoms, the measurements suggest that the time-dependent population in the $19s$ and $19p$ states can be described very accurately without including

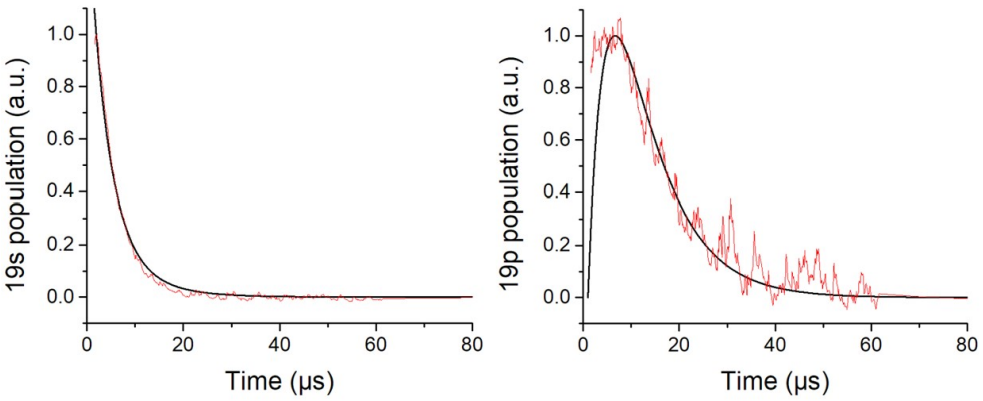

Figure A.1: Population in the $19s$ and $19p$ states as a function of delay for Rydberg atoms excited from atoms in a MOT (0.5mm FWHM, at $6 \times 10^7/\text{cm}^3$ Rydberg density). The black line is a theoretical model that includes spontaneous emission and transitions driven by blackbody radiation, but not cooperative effects. The red line shows the experimental results. The population in $19s$ is normalized to the population during the start of the delay time scan (2.3μs after $19s$ is excited), while the population in $19p$ is normalized to the largest population transfer to $19p$ (slightly higher in experimental data to account for noise).

collective effects. Apparently, collective decay does not play a significant role for $\frac{L}{\lambda} \gtrsim 1$.

More involved (but still incomplete) simulations [6] suggest that the key parameter for observing collective decay may not be $\frac{L}{\lambda}$, but rather $\gamma = \frac{1}{\lambda\rho^{1/3}}$. Such expression can be rewritten as $\gamma = \frac{L}{\lambda N^{1/3}}$, where N is the number of atoms within the ensemble, suggesting that in addition to the geometry of the ensemble, the number of atoms N is also an important factor. If γ is too small, dipole-dipole interactions dephase the system too rapidly for superradiance to occur. If γ is too big, the probability of one photon interacting with multiple atoms within a solid angle is too small, discouraging superradiance. For the experimental data shown above, $\gamma = 0.077$, which is close to the predicted optimal superradiance condition according to this model (see Figure A.2). The fact that no evidence of collective decay was observed suggests that the conditions necessary to observe Rydberg superradiance outside of the regime $\frac{L}{\lambda} \gg 1$ are still not fully understood.

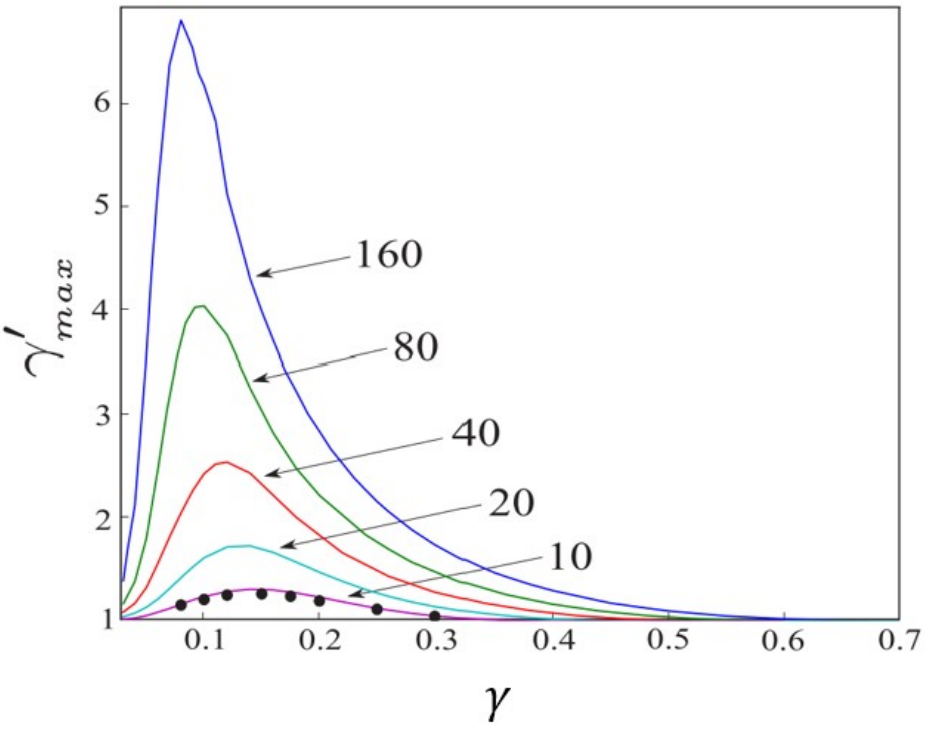

Figure A.2: Calculated maximum enhancement of photon emission rate ($\gamma'_{\max}$) versus $\gamma = \frac{1}{\lambda\rho^{1/3}}$ for Rydberg atom gas [6]. Different colors suggest different total number of atoms in the ensemble. The black dots represent simulation results for ensembles of fully-interacting 10 atom clouds. Figure taken from [6].

Bibliography

[1] C. He and R. R. Jones. Directional population control beyond the exceptional point in a non-Hermitian system. *Phys. Rev. A*, 104:013111, 2021.

[2] New Focus, Inc. *User's guide for 6000 Vortex Series tunable diode laser*, 2002.

[3] Toptica Photonics AG. *TA/DL-SHG pro Frequency Doubled High Power Laser System Manual*, 2009.

[4] J. L. Wiza. Microchannel plate detectors. *Nucl. Instrum. Methods*, 162(1):587–601, 1979.

[5] M. Kutteruf. *Coherence in Rydberg Atoms: Measurement and Control*. PhD thesis, University of Virginia, Charlottesville, VA, 2010.

[6] R. T. Sutherland and F. Robicheaux. Superradiance in inverted multilevel atomic clouds. *Phys. Rev. A*, 95:033839, 2017.

[7] L. H. Thomas. The Motion of the Spinning Electron. *Nature*, 117(2945):514–514, 1926.

[8] M. Born and R. Oppenheimer. Zur Quantentheorie der Molekeln. *Ann. Phys.*, 389(20):457–484, 1927.

[9] D. R. Hartree and W. Hartree. Self-consistent field, with exchange, for beryllium. *Proc. R. Soc. Lond. A.*, 150(869):9–33, 1935.

[10] Y. Alexeev, D. Bacon, K. R. Brown, R. Calderbank, L. D. Carr, F. T. Chong, B. DeMarco, D. Englund, E. Farhi, B. Fefferman, A. V. Gorshkov, A. Houck, J. Kim, S. Kimmel, M. Lange, S. Lloyd, M. D. Lukin, D. Maslov, P. Maunz, C. Monroe, J. Preskill, M. Roetteler, M. J. Savage, and J. Thompson. Quantum Computer Systems for Scientific Discovery. *PRX Quantum*, 2:017001, 2021.

[11] E. Altman, K. R. Brown, G. Carleo, L. D. Carr, E. Demler, C. Chin, B. DeMarco, S. E. Economou, M. A. Eriksson, K. C. Fu, M. Greiner, K. R.A. Hazzard, R. G. Hulet, A. J. Kollár, B. L. Lev, M. D. Lukin, R. Ma, X. Mi, S. Misra, C. Monroe, K. Murch, Z. Nazario, K. Ni, A. C. Potter, P. Roushan, M. Saffman, M. Schleier-Smith, I. Siddiqi, R. Simmonds, M. Singh, I. B. Spielman, K. Temme, D. S. Weiss, J. Vučković, V. Vuletić, J. Ye, and M. Zwierlein. Quantum Simulators: Architectures and Opportunities. *PRX Quantum*, 2:017003, 2021.

[12] D. Awschalom, K. K. Berggren, H. Bernien, S. Bhave, L. D. Carr, P. Davids, S. E. Economou, D. Englund, A. Faraon, M. Fejer, S. Guha, M. V. Gustafsson, E. Hu, L. Jiang, J. Kim, B. Korzh, P. Kumar, P. G. Kwiat, M. Lončar, M. D. Lukin, D. A.B. Miller, C. Monroe, S. W. Nam, P. Narang, J. S. Orcutt, M. G. Raymer, A. H. Safavi-

Naeini, M. Spiropulu, K. Srinivasan, S. Sun, J. Vučković, E. Waks, R. Walsworth, A. M. Weiner, and Z. Zhang. Development of Quantum Interconnects (QuICs) for Next-Generation Information Technologies. *PRX Quantum*, 2:017002, 2021.

[13] R. P. Feynman. Simulating physics with computers. *Int. J. Theor. Phys.*, 21(6):467–488, 1982.

[14] P.W. Shor. Algorithms for quantum computation: discrete logarithms and factoring. In *Proc. 35th Annu. IEEE Symp. Found. Comput. Sci.*, pages 124–134, 1994.

[15] D. P. DiVincenzo. The Physical Implementation of Quantum Computation. *Fortschr. Phys.*, 48(9-11):771–783, 2000.

[16] M. D. Lukin, M. Fleischhauer, R. Cote, L. M. Duan, D. Jaksch, J. I. Cirac, and P. Zoller. Dipole Blockade and Quantum Information Processing in Mesoscopic Atomic Ensembles. *Phys. Rev. Lett.*, 87:037901, 2001.

[17] E. Urban, T. A. Johnson, T. Henage, L. Isenhower, D. D. Yavuz, T. G. Walker, and M. Saffman. Observation of Rydberg blockade between two atoms. *Nat. Phys.*, 5(2):110–114, 2009.

[18] M. Weidemüller. There can only be one. *Nat. Phys.*, 5(2):91–92, 2009.

[19] M. Saffman, T. G. Walker, and K. Mølmer. Quantum information with Rydberg atoms. *Rev. Mod. Phys.*, 82:2313–2363, 2010.

[20] M. Saffman. Quantum computing with atomic qubits and Rydberg interactions: progress and challenges. *J. Phys. B*, 49(20):202001, 2016.

[21] M. Endres, H. Bernien, A. Keesling, H. Levine, E. R. Anschuetz, A. Krajenbrink, C. Senko, V. Vuletic, M. Greiner, and M. D. Lukin. Atom-by-atom assembly of defect-free one-dimensional cold atom arrays. *Science*, 354(6315):1024—1027, 2016.

[22] K. M. Maller, M. T. Lichtman, T. Xia, Y. Sun, M. J. Piotrowicz, A. W. Carr, L. Isenhower, and M. Saffman. Rydberg-blockade controlled-not gate and entanglement in a two-dimensional array of neutral-atom qubits. *Phys. Rev. A*, 92:022336, 2015.

[23] D. Blatt, R.and Wineland. Entangled states of trapped atomic ions. *Nature*, 453(7198):1008–1015, 2008.

[24] J. Clarke and F. K. Wilhelm. Superconducting quantum bits. *Nature*, 453(7198):1031–1042, 2008.

[25] D. R. Hartree. The Wave Mechanics of an Atom with a Non-Coulomb Central Field. Part I. Theory and Methods. *Math. Proc. Camb. Philos. Soc.*, 24(1):89–110, 1928.

[26] E. Tiesinga, P. J. Mohr, D. B. Newell, and B. N. Taylor. The 2018 CODATA Recommended Values of the Fundamental Physical Constants (Web Version 8.1), 2020.

[27] T. F. Gallagher. *Rydberg Atoms*. Cambridge Monographs on Atomic, Molecular and Chemical Physics. Cambridge University Press, 1994.

[28] C. J. Lorenzen and K. Niemax. Quantum Defects of the $n^2P_{1/2,3/2}$ Levels in ^{39}K I and ^{85}Rb I. *Phys. Scr.*, 27(4):300–305, 1983.

[29] Th. Förster. Zwischenmolekulare Energiewanderung und Fluoreszenz. *Ann. Phys.*, 437(1-2):55–75, 1948.

[30] S. Westermann, T. Amthor, A. L. de Oliveira, J. Deiglmayr, M. Reetz-Lamour, and M. Weidemüller. Dynamics of resonant energy transfer in a cold Rydberg gas. *Eur. Phys. J. D*, 40(1):37–43, 2006.

[31] I. I. Ryabtsev, D. B. Tretyakov, I. I. Beterov, and V. M. Entin. Observation of the Stark-Tuned Förster Resonance between Two Rydberg Atoms. *Phys. Rev. Lett.*, 104:073003, 2010.

[32] K. A. Safinya, J. F. Delpech, F. Gounand, W. Sandner, and T. F. Gallagher. Resonant Rydberg-Atom-Rydberg-Atom Collisions. *Phys. Rev. Lett.*, 47:405–408, 1981.

[33] W. R. Anderson, M. P. Robinson, J. D. D. Martin, and T. F. Gallagher. Dephasing of resonant energy transfer in a cold Rydberg gas. *Phys. Rev. A*, 65:063404, 2002.

[34] K. Singer, M. Reetz-Lamour, T. Amthor, L. G. Marcassa, and M. Weidemüller. Suppression of Excitation and Spectral Broadening Induced by Interactions in a Cold Gas of Rydberg Atoms. *Phys. Rev. Lett.*, 93:163001, 2004.

[35] M. Weidemüller. There can be only one. *Nat. Phys.*, 5(2):91–92, 2009.

[36] B. G. Richards and R. R. Jones. Dipole-dipole resonance line shapes in a cold Rydberg gas. *Phys. Rev. A*, 93:042505, 2016.

[37] M. R. Kutteruf and R. R. Jones. Probing Electronic Coherence in a Gas of Dipole-Dipole Coupled Rydberg Atoms. *Phys. Rev. Lett.*, 108:013001, 2012.

[38] T. Day, F. Luecke, and M. Brownell. Continuously tunable diode lasers. *Lasers and Optronics*, 12(6):15, 1993.

[39] K. C. Harvey and C. J. Myatt. External-cavity diode laser using a grazing-incidence diffraction grating. *Opt. Lett.*, 16(12):910–912, 1991.

[40] M. G. Littman and H. J. Metcalf. Spectrally narrow pulsed dye laser without beam expander. *Appl. Opt.*, 17(14):2224–2227, 1978.

[41] M. G. Littman. Single-mode operation of grazing-incidence pulsed dye laser. *Opt. Lett.*, 3(4):138–140, 1978.

[42] M. G. Littman. Single-mode pulsed tunable dye laser. *Appl. Opt.*, 23(24):4465–4468, 1984.

[43] K. Liu and M. G. Littman. Novel geometry for single-mode scanning of tunable lasers. *Opt. Lett.*, 6(3):117–118, 1981.

[44] T. W. Hänsch. Repetitively Pulsed Tunable Dye Laser for High Resolution Spectroscopy. *Appl. Opt.*, 11(4):895–898, 1972.

[45] R. N. Hall, G. E. Fenner, J. D. Kingsley, T. J. Soltys, and R. O. Carlson. Coherent Light Emission From GaAs Junctions. *Phys. Rev. Lett.*, 9:366–368, 1962.

[46] M. I. Nathan, W. P. Dumke, G. Burns, F. H. Dill, and G. Lasher. Stimulated Emission of Radiation from GaAs p-n Junctions. *Appl. Phys. Lett.*, 1(3):62–64, 1962.

[47] G. D. Boyd and D. A. Kleinman. Parametric Interaction of Focused Gaussian Light Beams. *J. Appl. Phys.*, 39(8):3597–3639, 1968.

[48] R. W. P. Drever, J. L. Hall, F. V. Kowalski, J. Hough, G. M. Ford, A. J. Munley, and H. Ward. Laser phase and frequency stabilization using an optical resonator. *Appl. Phys. B*, 31(2):97–105, 1983.

[49] E. D. Black. An introduction to Pound–Drever–Hall laser frequency stabilization. *Am. J. Phys.*, 69(1):79–87, 2001.

[50] N. Minorsky. Directional stability of automatically steered bodies. *J. Amer. Soc. Naval Eng.*, 34(2):280–309, 1922.

[51] T. Zhou. *Influence of Dipole-Dipole Interaction on Electron Dynamics in a Cold Rydberg Gas.* PhD thesis, University of Virginia, Charlottesville, VA, 2016.

[52] R. F. Stebbings and F. B. Dunning. *Rydberg States of Atoms and Molecules.* Essays in nuclear astrophysics. Cambridge University Press, 1983.

[53] G. Leuchs and H. Walther. Quantum interference effects in field ionization: Application to the measurement of the fine structure splitting of highly excited Na ^2D states. *Z. Phys., A At. nucl.*, 293(2):93–101, 1979.

[54] T. F. Gallagher, L. M. Humphrey, W. E. Cooke, R. M. Hill, and S. A. Edelstein. Field ionization of highly excited states of sodium. *Phys. Rev. A*, 16:1098–1108, 1977.

[55] T. H. Jeys, G. W. Foltz, K. A. Smith, E. J. Beiting, F. G. Kellert, F. B. Dunning, and R. F. Stebbings. Diabatic Field Ionization of Highly Excited Sodium Atoms. *Phys. Rev. Lett.*, 44:390–393, 1980.

[56] V. C. Gregoric, X. Kang, Z. C. Liu, Z. A. Rowley, T. J. Carroll, and M. W. Noel. Quantum control via a genetic algorithm of the field ionization pathway of a Rydberg electron. *Phys. Rev. A*, 96:023403, 2017.

[57] V. C. Gregoric, J. J. Bennett, B. R. Gualtieri, A. Kannad, Z. C. Liu, Z. A. Rowley, T. J. Carroll, and M. W. Noel. Improving the state selectivity of field ionization with quantum control. *Phys. Rev. A*, 98:063404, 2018.

[58] V. C. Gregoric, J. J. Bennett, B. R. Gualtieri, H. P. Hastings, A. Kannad, Z. C. Liu, M. R. Rabinowitz, Z. A. Rowley, M. Wang, L. Yoast, T. J. Carroll, and M. W. Noel. Perturbed field ionization for improved state selectivity. *J. Phys. B: At. Mol. Opt. Phys.*, 53(8):084003, 2020.

[59] SAES Getters S.p.A. *Alkali Metal Dispensers Brochure*, 2007.

[60] E. L. Raab, M. Prentiss, A. Cable, S. Chu, and D. E. Pritchard. Trapping of Neutral Sodium Atoms with Radiation Pressure. *Phys. Rev. Lett.*, 59:2631–2634, 1987.

[61] W. Ketterle. 8.422 Atomic and Optical Physics II., Spring 2013. Massachusetts Institute of Technology: MIT OpenCourseWare.

[62] A. Ashkin. Acceleration and Trapping of Particles by Radiation Pressure. *Phys. Rev. Lett.*, 24:156–159, 1970.

[63] A. Ashkin. Atomic-Beam Deflection by Resonance-Radiation Pressure. *Phys. Rev. Lett.*, 25:1321–1324, 1970.

[64] S. Chu, L. Hollberg, J. E. Bjorkholm, A. Cable, and A. Ashkin. Three-dimensional viscous confinement and cooling of atoms by resonance radiation pressure. *Phys. Rev. Lett.*, 55:48–51, 1985.

[65] P. D. Lett, R. N. Watts, C. I. Westbrook, W. D. Phillips, P. L. Gould, and H. J. Metcalf. Observation of Atoms Laser Cooled below the Doppler Limit. *Phys. Rev. Lett.*, 61:169–172, 1988.

[66] T. Bergeman, G. Erez, and H. J. Metcalf. Magnetostatic trapping fields for neutral atoms. *Phys. Rev. A*, 35:1535–1546, 1987.

[67] D. A. Steck. Rubidium 85 D Line Data (revision 2.2.3), 2021.

[68] A. Ashkin, J. M. Dziedzic, J. E. Bjorkholm, and S. Chu. Observation of a single-beam gradient force optical trap for dielectric particles. *Opt. Lett.*, 11(5):288–290, 1986.

[69] M. L. Zimmerman, M. G. Littman, M. M. Kash, and D. Kleppner. Stark structure of the Rydberg states of alkali-metal atoms. *Phys. Rev. A*, 20:2251–2275, 1979.

[70] F. Robicheaux, J. V. Hernández, T. Topçu, and L. D. Noordam. Simulation of coherent interactions between Rydberg atoms. *Phys. Rev. A*, 70:042703, 2004.

[71] D. W. Schönleber, A. Eisfeld, M. Genkin, S. Whitlock, and S. Wüster. Quantum Simulation of Energy Transport with Embedded Rydberg Aggregates. *Phys. Rev. Lett.*, 114:123005, 2015.

[72] G. Racah. Theory of Complex Spectra. II. *Phys. Rev.*, 62:438–462, 1942.

[73] A. R. Edmonds. *Angular Momentum in Quantum Mechanics*. Princeton Landmarks in Mathematics and Physics. Princeton University Press, 1996.

[74] B. G. Richards. *Dipole-Dipole Interactions in a Cold Rydberg Gas*. PhD thesis, University of Virginia, Charlottesville, VA, 2017.

[75] W. R. Anderson, J. R. Veale, and T. F. Gallagher. Resonant Dipole-Dipole Energy Transfer in a Nearly Frozen Rydberg Gas. *Phys. Rev. Lett.*, 80:249–252, 1998.

[76] I. Mourachko, D. Comparat, F. de Tomasi, A. Fioretti, P. Nosbaum, V. M. Akulin, and P. Pillet. Many-Body Effects in a Frozen Rydberg Gas. *Phys. Rev. Lett.*, 80:253–256, 1998.

[77] I. Mourachko, W. Li, and T. F. Gallagher. Controlled many-body interactions in a frozen Rydberg gas. *Phys. Rev. A*, 70:031401, 2004.

[78] G. Abumwis, M. T. Eiles, and A. Eisfeld. Delocalization in two and three-dimensional Rydberg gases. *J. Phys. B: At. Mol. Opt. Phys.*, 53(12):124003, 2020.

[79] G. Abumwis, M. T. Eiles, and A. Eisfeld. Extended Coherently Delocalized States in a Frozen Rydberg Gas. *Phys. Rev. Lett.*, 124:193401, 2020.

[80] F. Robicheaux and N. M. Gill. Effect of random positions for coherent dipole transport. *Phys. Rev. A*, 89:053429, 2014.

[81] K. C. Younge, A. Reinhard, T. Pohl, P. R. Berman, and G. Raithel. Mesoscopic Rydberg ensembles: Beyond the pairwise-interaction approximation. *Phys. Rev. A*, 79:043420, 2009.

[82] B. Sun and F. Robicheaux. Spectral linewidth broadening from pair fluctuations in a frozen Rydberg gas. *Phys. Rev. A*, 78:040701, 2008.

[83] J. V. Hernández and F. Robicheaux. Simulations using echo sequences to observe coherence in a cold Rydberg gas. *J. Phys. B*, 41(19):195301, 2008.

[84] T. Zhou, S. Li, and R. R. Jones. Rydberg-wave-packet evolution in a frozen gas of dipole-dipole-coupled atoms. *Phys. Rev. A*, 89:063413, 2014.

[85] T. J. Carroll, C. Daniel, L. Hoover, T. Sidie, and M. W. Noel. Simulations of the dipole-dipole interaction between two spatially separated groups of Rydberg atoms. *Phys. Rev. A*, 80:052712, 2009.

[86] D. P. Fahey, T. J. Carroll, and M. W. Noel. Imaging the dipole-dipole energy exchange between ultracold rubidium Rydberg atoms. *Phys. Rev. A*, 91:062702, 2015.

[87] Z. C. Liu, N. P. Inman, T. J. Carroll, and M. W. Noel. Time Dependence of Few-Body Förster Interactions among Ultracold Rydberg Atoms. *Phys. Rev. Lett.*, 124:133402, 2020.

[88] C. E. Shannon. Communication in the Presence of Noise. *Proc. Inst. Radio Eng.*, 37(1):10–21, 1949.

[89] M. Abramowitz and I. A. Stegun. *Handbook of Mathematical Functions with Formulas, Graphs, and Mathematical Tables*. Applied mathematics series. Dover Publications, 1964.

[90] Gounand, F. Calculation of radial matrix elements and radiative lifetimes for highly excited states of alkali atoms using the Coulomb approximation. *J. Phys. France*, 40(5):457–460, 1979.

[91] T. Zhou, B. G. Richards, and R. R. Jones. Absence of collective decay in a cold Rydberg gas. *Phys. Rev. A*, 93:033407, 2016.

[92] A. Peres. Reversible logic and quantum computers. *Phys. Rev. A*, 32:3266–3276, 1985.

[93] P. W. Shor. Scheme for reducing decoherence in quantum computer memory. *Phys. Rev. A*, 52:R2493–R2496, 1995.

[94] A. R. Calderbank and P. W. Shor. Good quantum error-correcting codes exist. *Phys. Rev. A*, 54:1098–1105, 1996.

[95] R. Laflamme, C. Miquel, J. P. Paz, and W. H. Zurek. Perfect Quantum Error Correcting Code. *Phys. Rev. Lett.*, 77:198–201, 1996.

[96] D. A. Lidar, D. Bacon, and K. B. Whaley. Concatenating Decoherence-Free Subspaces with Quantum Error Correcting Codes. *Phys. Rev. Lett.*, 82:4556–4559, 1999.

[97] N. Boulant, L. Viola, E. M. Fortunato, and D. G. Cory. Experimental Implementation of a Concatenated Quantum Error-Correcting Code. *Phys. Rev. Lett.*, 94:130501, 2005.

[98] J. Chiaverini, D. Leibfried, T. Schaetz, M. D. Barrett, R. B. Blakestad, J. Britton, W. M. Itano, J. D. Jost, E. Knill, C. Langer, R. Ozeri, and D. J. Wineland. Realization of quantum error correction. *Nature*, 432(7017):602–605, 2004.

[99] T. B. Pittman, B. C. Jacobs, and J. D. Franson. Demonstration of quantum error correction using linear optics. *Phys. Rev. A*, 71:052332, 2005.

[100] P. T. Cochrane, G. J. Milburn, and W. J. Munro. Macroscopically distinct quantum-superposition states as a bosonic code for amplitude damping. *Phys. Rev. A*, 59:2631–2634, 1999.

[101] Z. Leghtas, G. Kirchmair, B. Vlastakis, R. J. Schoelkopf, M. H. Devoret, and M. Mirrahimi. Hardware-Efficient Autonomous Quantum Memory Protection. *Phys. Rev. Lett.*, 111:120501, 2013.

[102] M. Mirrahimi, Z. Leghtas, V. V. Albert, S. Touzard, R. J. Schoelkopf, L. Jiang, and M. H. Devoret. Dynamically protected cat-qubits: a new paradigm for universal quantum computation. *New J. Phys.*, 16(4):045014, 2014.

[103] E. Knill. Quantum computing with realistically noisy devices. *Nature*, 434(7029):39–44, 2005.

[104] D. G. Cory, M. D. Price, W. Maas, E. Knill, R. Laflamme, W. H. Zurek, T. F. Havel, and S. S. Somaroo. Experimental Quantum Error Correction. *Phys. Rev. Lett.*, 81:2152–2155, 1998.

[105] R. S. Minns, M. R. Kutteruf, H. Zaidi, L. Ko, and R. R. Jones. Preserving Coherence in Rydberg Quantum Bits. *Phys. Rev. Lett.*, 97:040504, 2006.

[106] R. S. Minns, M. R. Kutteruf, M. A. Commisso, and R. R. Jones. Decoherence suppression in a resonant driving field. *J. Phys. B*, 41(7):074012, 2008.

[107] L. Viola and S. Lloyd. Dynamical suppression of decoherence in two-state quantum systems. *Phys. Rev. A*, 58:2733–2744, 1998.

[108] L. Viola, E. Knill, and S. Lloyd. Dynamical Decoupling of Open Quantum Systems. *Phys. Rev. Lett.*, 82:2417–2421, 1999.

[109] C. Search and P. R. Berman. Suppression of Magnetic State Decoherence Using Ultrafast Optical Pulses. *Phys. Rev. Lett.*, 85:2272–2275, 2000.

[110] E. Fraval, M. J. Sellars, and J. J. Longdell. Method of Extending Hyperfine Coherence Times in $Pr^{3+} : Y_2SiO_5$. *Phys. Rev. Lett.*, 92:077601, 2004.

[111] E. Fraval, M. J. Sellars, and J. J. Longdell. Dynamic Decoherence Control of a Solid-State Nuclear-Quadrupole Qubit. *Phys. Rev. Lett.*, 95:030506, 2005.

[112] P. Facchi, D. A. Lidar, and S. Pascazio. Unification of dynamical decoupling and the quantum Zeno effect. *Phys. Rev. A*, 69:032314, 2004.

[113] P. Facchi, S. Tasaki, S. Pascazio, H. Nakazato, A. Tokuse, and D. A. Lidar. Control of decoherence: Analysis and comparison of three different strategies. *Phys. Rev. A*, 71:022302, 2005.

[114] S. Damodarakurup, M. Lucamarini, G. Di Giuseppe, D. Vitali, and P. Tombesi. Experimental Inhibition of Decoherence on Flying Qubits via "Bang-Bang" Control. *Phys. Rev. Lett.*, 103:040502, 2009.

[115] J. A. Armstrong, N. Bloembergen, J. Ducuing, and P. S. Pershan. Interactions between Light Waves in a Nonlinear Dielectric. *Phys. Rev.*, 127:1918–1939, 1962.

[116] P. A. Franken and J. F. Ward. Optical Harmonics and Nonlinear Phenomena. *Rev. Mod. Phys.*, 35:23–39, 1963.

[117] D. Feng, N. Ming, J. Hong, Y. Yang, J. Zhu, Z. Yang, and Y. Wang. Enhancement of second-harmonic generation in $LiNbO_3$ crystals with periodic laminar ferroelectric domains. *Appl. Phys. Lett.*, 37(7):607–609, 1980.

[118] A. Mondragon and E. Hernandez. Degeneracy and crossing of resonance energy surfaces. *J. Phys. A: Math. Gen.*, 26(20):5595–5611, 1993.

[119] R. Uzdin, A. Mailybaev, and N. Moiseyev. On the observability and asymmetry of adiabatic state flips generated by exceptional points. *J. Phys. A: Math. Theor.*, 44(43):435302, 2011.

[120] H. Xu, D. Mason, L. Jiang, and J. G. E. Harris. Topological energy transfer in an optomechanical system with exceptional points. *Nature*, 537(7618):80–83, 2016.

[121] C. Miniatura, C. Sire, J. Baudon, and J. Bellissard. Geometrical Phase Factor for a Non-Hermitian Hamiltonian. *Europhys. Lett.*, 13(3):199–203, 1990.

[122] W. D. Heiss. Repulsion of resonance states and exceptional points. *Phys. Rev. E*, 61:929–932, 2000.

[123] G. Nenciu and G. Rasche. On the adiabatic theorem for nonself-adjoint Hamiltonians. *J. Phys. A: Math. Gen.*, 25(21):5741–5751, 1992.

[124] M. V. Berry and R. Uzdin. Slow non-Hermitian cycling: exact solutions and the Stokes phenomenon. *J. Phys. A: Math. Theor.*, 44(43):435303, 2011.

[125] T. J. Milburn, J. Doppler, C. A. Holmes, S. Portolan, S. Rotter, and P. Rabl. General description of quasiadiabatic dynamical phenomena near exceptional points. *Phys. Rev. A*, 92:052124, 2015.

[126] C. Dembowski, H. D. Gräf, H. L. Harney, A. Heine, W. D. Heiss, H. Rehfeld, and A. Richter. Experimental Observation of the Topological Structure of Exceptional Points. *Phys. Rev. Lett.*, 86:787–790, 2001.

[127] S. B. Lee, J. Yang, S. Moon, S. Y. Lee, J. B. Shim, S. W. Kim, J. H. Lee, and K. An. Observation of an Exceptional Point in a Chaotic Optical Microcavity. *Phys. Rev. Lett.*, 103:134101, 2009.

[128] R. Lefebvre, O. Atabek, M. Šindelka, and N. Moiseyev. Resonance Coalescence in Molecular Photodissociation. *Phys. Rev. Lett.*, 103:123003, 2009.

[129] A. Leclerc, D. Viennot, G. Jolicard, R. Lefebvre, and O. Atabek. Exotic states in the strong-field control of H_2^+ dissociation dynamics: from exceptional points to zero-width resonances. *J. Phys. B: At. Mol. Opt. Phys.*, 50(23):234002, 2017.

[130] O. Atabek, R. Lefebvre, M. Lepers, A. Jaouadi, O. Dulieu, and V. Kokoouline. Proposal for a Laser Control of Vibrational Cooling in Na_2 Using Resonance Coalescence. *Phys. Rev. Lett.*, 106:173002, 2011.

[131] H. Cartarius, J. Main, and G. Wunner. Exceptional Points in Atomic Spectra. *Phys. Rev. Lett.*, 99:173003, 2007.

[132] B. Zhen, C. W. Hsu, Y. Igarashi, L. Lu, I. Kaminer, A. Pick, S. L. Chua, J. D. Joannopoulos, and M. Soljačić. Spawning rings of exceptional points out of Dirac cones. *Nature*, 525(7569):354–358, 2015.

[133] T. Gao, E. Estrecho, K. Y. Bliokh, T. C. H. Liew, M. D. Fraser, S. Brodbeck, M. Kamp, C. Schneider, S. Höfling, Y. Yamamoto, F. Nori, Y. S. Kivshar, A. G. Truscott, R. G. Dall, and E. A. Ostrovskaya. Observation of non-Hermitian degeneracies in a chaotic exciton-polariton billiard. *Nature*, 526(7574):554–558, 2015.

[134] T. Stehmann, W. D. Heiss, and F. G. Scholtz. Observation of exceptional points in electronic circuits. *J. Phys. A: Math. Gen.*, 37(31):7813–7819, 2004.

[135] P. Peng, W. Cao, C. Shen, W. Qu, J. Wen, L. Jiang, and Y. Xiao. Anti-parity–time symmetry with flying atoms. *Nat. Phys.*, 12(12):1139–1145, 2016.

[136] B. Longstaff and E. M. Graefe. Nonadiabatic transitions through exceptional points in the band structure of a PT-symmetric lattice. *Phys. Rev. A*, 100:052119, 2019.

[137] C. Zener. Non-adiabatic crossing of energy levels. *Proc. R. Soc. London Ser. A*, 137:696–702, 1932.

[138] Y. Avishai and Y. B. Band. Landau-Zener problem with decay and dephasing. *Phys. Rev. A*, 90:032116, 2014.

[139] V. M. Akulin and W. P. Schleich. Landau-Zener transition to a decaying level. *Phys. Rev. A*, 46:4110–4113, 1992.

[140] T. M. Graham, M. Kwon, B. Grinkemeyer, Z. Marra, X. Jiang, M. T. Lichtman, Y. Sun, M. Ebert, and M. Saffman. Rydberg-Mediated Entanglement in a Two-Dimensional Neutral Atom Qubit Array. *Phys. Rev. Lett.*, 123:230501, 2019.

[141] R. H. Dicke. Coherence in Spontaneous Radiation Processes. *Phys. Rev.*, 93:99–110, 1954.

[142] T. Wang, S. F. Yelin, R. Côté, E. E. Eyler, S. M. Farooqi, P. L. Gould, M. Koštrun, D. Tong, and D. Vrinceanu. Superradiance in ultracold Rydberg gases. *Phys. Rev. A*, 75:033802, 2007.

[143] J. Han and H. Maeda. Super-radiance-cascades and multimode superradiance oscillations in a cold ^{85}Rb Rydberg gas. *Can. J. Phys.*, 92(10):1130–1134, 2014.

[144] N. Skribanowitz, I. P. Herman, J. C. MacGillivray, and M. S. Feld. Observation of Dicke Superradiance in Optically Pumped HF Gas. *Phys. Rev. Lett.*, 30:309–312, 1973.

[145] M. Gross, C. Fabre, P. Pillet, and S. Haroche. Observation of Near-Infrared Dicke Superradiance on Cascading Transitions in Atomic Sodium. *Phys. Rev. Lett.*, 36:1035–1038, 1976.

[146] D. Pavolini, A. Crubellier, P. Pillet, L. Cabaret, and S. Liberman. Experimental Evidence for Subradiance. *Phys. Rev. Lett.*, 54:1917–1920, 1985.

[147] M. G. Moore and P. Meystre. Theory of Superradiant Scattering of Laser Light from Bose-Einstein Condensates. *Phys. Rev. Lett.*, 83:5202–5205, 1999.

[148] J. I. Kim, R. B. B. Santos, and P. Nussenzveig. Manipulation of Cold Atomic Collisions by Cavity QED Effects. *Phys. Rev. Lett.*, 86:1474–1477, 2001.

[149] C. Greiner, B. Boggs, and T. W. Mossberg. Superradiant Emission Dynamics of an Optically Thin Material Sample in a Short-Decay-Time Optical Cavity. *Phys. Rev. Lett.*, 85:3793–3796, 2000.

[150] C. F. Lee and N. F. Johnson. First-Order Superradiant Phase Transitions in a Multiqubit Cavity System. *Phys. Rev. Lett.*, 93:083001, 2004.

[151] V. V. Temnov and U. Woggon. Superradiance and Subradiance in an Inhomogeneously Broadened Ensemble of Two-Level Systems Coupled to a Low-Q Cavity. *Phys. Rev. Lett.*, 95:243602, 2005.

[152] J. O. Day, E. Brekke, and T. G. Walker. Dynamics of low-density ultracold Rydberg gases. *Phys. Rev. A*, 77:052712, 2008.

[153] K. Prozument, A. P. Colombo, Y. Zhou, G. B. Park, V. S. Petrović, S. L. Coy, and R. W. Field. Chirped-Pulse Millimeter-Wave Spectroscopy of Rydberg-Rydberg Transitions. *Phys. Rev. Lett.*, 107:143001, 2011.

[154] A. P. Colombo, Y. Zhou, K. Prozument, S. L. Coy, and R. W. Field. Chirped-pulse millimeter-wave spectroscopy: Spectrum, dynamics, and manipulation of Rydberg–Rydberg transitions. *J. Chem. Phys.*, 138(1):014301, 2013.

[155] F. Karlewski, M. Mack, J. Grimmel, N. Sándor, and J. Fortágh. State-selective all-optical detection of Rydberg atoms. *Phys. Rev. A*, 91:043422, 2015.

[156] D. Meiser and M. J. Holland. Steady-state superradiance with alkaline-earth-metal atoms. *Phys. Rev. A*, 81:033847, 2010.

[157] D. Meiser and M. J. Holland. Intensity fluctuations in steady-state superradiance. *Phys. Rev. A*, 81:063827, 2010.

[158] J. G. Bohnet, Z. Chen, J. M. Weiner, D. Meiser, M. J. Holland, and J. K. Thompson. A steady-state superradiant laser with less than one intracavity photon. *Nature*, 484(7392):78–81, 2012.

[159] F. Gounand, M. Hugon, P. R. Fournier, and J. Berlande. Superradiant cascading effects in rubidium Rydberg levels. *J. Phys. B*, 12(4):547–553, 1979.

[160] J. M. Weiner, K. C. Cox, J. G. Bohnet, and J. K. Thompson. Phase synchronization inside a superradiant laser. *Phys. Rev. A*, 95:033808, 2017.

[161] M. A. Norcia and J. K. Thompson. Cold-Strontium Laser in the Superradiant Crossover Regime. *Phys. Rev. X*, 6:011025, 2016.

[162] M. A. Norcia, R. J. Lewis-Swan, J. R. K. Cline, B. Zhu, A. M. Rey, and J. K. Thompson. Cavity-mediated collective spin-exchange interactions in a strontium superradiant laser. *Science*, 361(6399):259–262, 2018.

[163] A. Asenjo-Garcia, M. Moreno-Cardoner, A. Albrecht, H. J. Kimble, and D. E. Chang. Exponential Improvement in Photon Storage Fidelities Using Subradiance and "Selective Radiance" in Atomic Arrays. *Phys. Rev. X*, 7:031024, 2017.

[164] A. Goban, C. L. Hung, J. D. Hood, S. P. Yu, J. A. Muniz, O. Painter, and H. J. Kimble. Superradiance for Atoms Trapped along a Photonic Crystal Waveguide. *Phys. Rev. Lett.*, 115:063601, 2015.

[165] A. Shankar, J. T. Reilly, S. B. Jäger, and M. J. Holland. Subradiant-to-Subradiant Phase Transition in the Bad Cavity Laser. *Phys. Rev. Lett.*, 127:073603, 2021.

[166] K. Kitano, H. Tomida, D. Takei, and H. Maeda. Polarization correlation in the superfluorescent decay process. *Opt. Lett.*, 46(19):5055–5058, 2021.

[167] T. C. Killian, S. Kulin, S. D. Bergeson, L. A. Orozco, C. Orzel, and S. L. Rolston. Creation of an Ultracold Neutral Plasma. *Phys. Rev. Lett.*, 83:4776–4779, 1999.

[168] M. P. Robinson, B. Laburthe Tolra, Michael W. Noel, T. F. Gallagher, and P. Pillet. Spontaneous Evolution of Rydberg Atoms into an Ultracold Plasma. *Phys. Rev. Lett.*, 85:4466–4469, 2000.

[169] M. Robert-de Saint-Vincent, C. S. Hofmann, H. Schempp, G. Günter, S. Whitlock, and M. Weidemüller. Spontaneous Avalanche Ionization of a Strongly Blockaded Rydberg Gas. *Phys. Rev. Lett.*, 110:045004, 2013.

[170] P. J. Tanner, J. Han, E. S. Shuman, and T. F. Gallagher. Many-Body Ionization in a Frozen Rydberg Gas. *Phys. Rev. Lett.*, 100:043002, 2008.

[171] A. Reinhard, T. Cubel Liebisch, K. C. Younge, P. R. Berman, and G. Raithel. Rydberg-Rydberg Collisions: Resonant Enhancement of State Mixing and Penning Ionization. *Phys. Rev. Lett.*, 100:123007, 2008.